Federico Santa María Technical University

Department of Physics

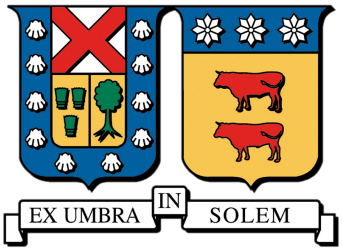

Precise Determination of the Axial Contribution to the Coherent Elastic neutrino-Nucleus Scattering Event Rate

Thesis for the degree of Master's

Author:
Laura Trincado Saldibar

Supervisor:
Diego Aristizabal Sierra

April 24, 2026

CONSTANCIA DE VALIDACIÓN Y CONFIDENCIALIDAD DE MONOGRAFÍA A REPOSITORIO ACADÉMICO

1.- IDENTIFICACIÓN DEL TRABAJO ACADÉMICO

Tipo de monografía (marcar una opción): ☐ Memoria o trabajo de título ☒ Tesis de Postgrado

Título del trabajo: Precise determination of the axial contribution to the coherent elastic neutrino-nucleus scattering event rate

Nombre del candidato(a): Laura Trincado Saldibar

Carrera / Grado: Magister en Física

Campus: San Joaquin **Departamento:** Departamento de física

2.- VALIDACIÓN DEL PROFESOR GUÍA/DIRECTOR DE TESIS

Yo, Diego Aristizabal en mi calidad de profesor(a) guía/director(a) del trabajo académico mencionado anteriormente **DEJO CONSTANCIA** que:

- He revisado esta versión del documento y corresponde a la versión final aprobada del trabajo.
- El trabajo cumple con los requisitos académicos y de formato establecidos por la institución.

3.- EVALUACIÓN DE CONFIDENCIALIDAD POR PROPIEDAD INDUSTRIAL (marcar una opción)

☒ El trabajo **NO contiene** información que amerite confidencialidad y puede ser publicado de inmediato en repositorio con acceso abierto.

☐ El trabajo **CONTIENE** información con potenciales implicancias de propiedad industrial o intelectual y requiere un periodo de confidencialidad (**embargo**) por **(marcar una opción)**:

☐ 6 meses ☐ 12 meses ☐ 2 años ☐ 3 años ☐ 5 años ☐ 10 años

Fundamentación de la necesidad de confidencialidad (obligatorio si se solicita embargo):

_____

_____

_____

4.- FIRMAS

Profesor(a) guía o director(a) de memoria o tesis:

Fecha: 24-0-2026 **Firma:** _____

Estudiante o Candidato(a):

Fecha: 24-0-2026 **Firma:** _____

Este formulario debe ser insertado como página 2 de la memoria o tesis, completado y firmado por estudiante y profesor(a) antes de la entrega en portal PRISMA de Biblioteca USM.

To my parents

Abstract

Coherent elastic neutrino–nucleus scattering (CEνNS) is a low-energy process within the Standard Model, characterized by an enhanced cross section due to the coherent vector weak charge. Although this dominant contribution has been thoroughly investigated, subleading axial-vector effects are typically considered suppressed and have consequently received limited attention.

In this work, we present a systematic determination of the axial contribution to the CEνNS differential cross section within an effective field theory framework, incorporating spin-dependent nuclear structure factors from modern nuclear calculations. We identify target-dependent regimes in which the axial contribution is not strongly suppressed relative to the vector term, challenging the common assumption of its negligibility and providing a basis for precision CEνNS analyses beyond the coherent approximation.

Acknowledgements

I dedicate this work to my parents. I am the daughter of a miner, my father, Cristian Trincado, who built his life through effort, dedication, and intelligence. He devoted himself completely to his work to ensure that nothing was ever lacking for his daughters. To my mother, Ana Saldibar, who is the most noble, patient, and loving person I know. She gave her life to her daughters so that we could grow up in a home filled with peace, happiness, and love. From both of them, I learned perseverance, dedication, sacrifice, courage, and above all, love.

I am grateful to my sisters, Anais, Sofia, and Beatriz, with whom I grew up, and to my little baby, who have never left me alone and have always made me believe in myself. They have been the embrace I needed at every moment. They are the ones who have supported me and given me the confidence I needed.

To my friends, who understand the effort behind this journey we have shared together. To my special friend, who brought happiness into my life and stood patiently by my side.

Finally, I would like to thank my supervisor for patiently listening to my questions and dedicating his time to make this work possible, and all my professors, who guided me in the path of physics and encouraged me not to give up because they believed in me.

Contents

List of Figures

List of Tables

Chapter 1

Introduction

Among the elementary particles that form the universe, neutrinos played a crucial role in our understanding of particle physics. The study of their properties and interactions has been one of the most dynamic activities in particle physics and astrophysics, since Pauli proposed their existence in 1930 [1]. Neutrino interactions are described with an impressive accuracy by the Standard Model (SM) having no electric charge and coupled weakly, make them unique tools for exploring fundamental phenomena in astrophysical, cosmological and particle physics processes.

In astrophysical contexts, neutrinos are the dominant mechanism for energy loss in core-collapse supernovae process [2, 3]. Furthermore, the Sun is a powerful source of neutrinos, making these a unique tool that enables us to get direct information of the solar interior [4]. At cosmological scales, process during the primordial nucleosynthesis era, and large-scale structure formation, neutrinos played an essential role [5, 6].

In particle physics neutrinos have a central role in the development of the theory of weak interactions. Beginning with the historical β-decay process, in which the interaction is understood as a product of four spinor fields. The discovery of neutrino oscillations demonstrated that neutrinos have non-zero masses, thus providing the first evidence for beyond the SM physics [7]. Furthermore, it is possible to establish a relation between particle physics and nuclear physics. Being subject solely to weak interactions they interact directly with the nuclei, providing information on the internal distribution of nucleons and giving access to the fundamental couplings of the weak force at the nuclear level.

It is in this intersection where Coherent Elastic neutrino-Nucleus Scattering (CEνNS) emerges as a powerful tool for research on nuclear structure. Where precision measurement of CEνNS provides information on nuclear structure, including the determination of nuclear form factors [8]. In addition, CEνNS is characterized by a relatively high interaction rate and small intrinsic nuclear uncertainties thus it is cleanly predicted in the SM. It therefore it is excellent probe for precision tests of fundamental parameters in the electroweak sector [9, 10] and enables searches for physics beyond the SM [10, 11].

In astrophysics CEνNS is also highly relevant. Neutrinos produced in Sun, supernovae and atmospheric cosmic-ray showers can produce nuclear recoils in terrestrial detectors through this process, leading to signals in dark matter (DM) detectors [12, 13]. Furthermore this process is of paramount importance for WIMP searches. It represents an irreducible background, thus demanding its full understanding [13].

Predicted in 1974 by Daniel Freedman [14] as a consequence of the neutral weak current. This SM process remained unobserved for decades due to the daunting technical requirements: very low nuclear recoil energy thresholds, intense sources/large target masses, and low backgrounds [15]. It was finally observed in 2017 by the COHERENT Collaboration, using 14.6 kg in a cesium iodide scintillation detector exposed to the neutrino flux of the Spallation Neutron Source (SNS) at the Oak Ridge National Laboratory (ORNL) [16].

Following its initial observation, the COHERENT collaboration has developed a comprehensive experimental program to investigate CEνNS across various targets and physics regimes. The first measurement of CEνNS on argon provided a crucial test of the process in a lighter nucleus, confirming that the cross-section scales with the square of the neutron number [17]. In parallel, the experiment has probed sensitivity to physics beyond the SM. This includes searches for accelerator-produced dark matter [18, 19], which demonstrates the versatility of the CEνNS signal as a probe for new interactions. More recently, the initial detection of CEνNS on germanium nuclei [20] has extended the experimental program to lower recoil energies, thereby enhancing sensitivity to subtle effects and enabling more precise investigations.

The cross section is sizable when the momentum transferred in the neutrino-nucleus interaction is below 200 MeV for typical nuclei. Under these conditions, nuclear structure effects are less significant, and the scattering is enhanced proportionally to the square of the number of neutrons. In the SM, CEνNS is described by the neutral current interaction between neutrinos and quarks, mediated by the Z^0 boson. [12, 14]. At the nuclear level there are two contributions vector and axial: The vector current contributes dominantly, with sub-leading contributions from the axial current. The latter, being related with nuclear spin, is relevant only in nuclei with spin non-zero ground-state.

Energy recoils, which are the measurable signal are small. Actually, measurements of CEνNS require innovative technologies, accelerating advances in neutrino detection techniques in order to achieve the required ultra low-threshold operation level and background reduction. For this reason, the COHERENT program includes plans for upgrades, exploiting a variety of target materials, different detection technologies, and ton-scale detectors [21].

Furthermore, XENONnT [22], PandaX-4T [23] and LZ [24] have reported their first measurement CEνNS, and soon next-generation facilities such as the European Spallation Source (ESS) are expected to provide larger neutrino fluxes [25], enabling precision measurements of CEνNS that were previously beyond reach. These, indicates a experimental progress that will producing the reduction of experimental and theoretical uncertainties for CEνNS.

In light of this emerging precision era, sub-leading effects in the scattering process become increasingly relevant. Therefore, the axial contribution, that has been historical neglected due to its strong suppression, demands a more careful and systematic study. In this context, upcoming experiments with larger detector masses, different material targets and access to smaller nuclear recoil energy are expected. They will open the possibility of experimentally accessing axial-current effects in CEνNS. It should be noted that access is essential for a complete understanding of neutrino-nucleus scattering. The measurement of this quantity will open new possibilities for spin-dependent new physics searches, while providing indirect information on the axial-vector coupling g_{A}.

Motivated by the previous discussion, this work examines the axial contribution to the CEνNS process and identifies the experimental conditions required for its measurement. The analysis uses the multipole decomposition formalism of Donnelly and Walecka [26, 27] as the nuclear framework to implement structure factors. These structure factors, from Ref. [28], are based on nuclear structure computations initially developed for direct DM detection and later adapted for CEνNS interactions. This connects nuclear structure computation methods to the study of CEνNS.

Building on this framework, the spin-dependent nuclear responses for isotopes most relevant in CEνNS experiments are calculated and analyzed. This methodology enables the consistent determination of the differential cross section. Both axial and vector contributions are incorporated. The axial component's magnitude is evaluated relative to the dominant coherent contribution across different target materials and spallation neutrino sources. The physical parameters and experimental conditions that impact its detectability are also identified.

This study identifies the ^{19}F isotope as the most suitable target for investigating the axial component in CEνNS. Compared to heavy nuclei, which strongly suppress the axial contribution due to their spin structure, light nuclei with non-zero spin, such as ^{19}F, experience much less suppression. Specifically, ^{19}F possesses a nuclear spin structure characterized by sizable nucleon spin expectation values. This property enhances the axial contribution to the cross-section.

In a realistic context, fluorine-based compounds such as CF_4, C_3F_8, and C_4F_{10} are particularly attractive. Among these, the use of C_3F_8 is identified as optimal, as it offers a favorable axial response and supports operation at large detector masses. The viability of this approach is further supported by the prior development of bubble chamber detectors in dark matter experiments [29, 30], which already employ these materials, facilitating their direct application in the CEνNS context. Under realistic experimental configurations. It is demonstrated that, despite inherent suppression relative to the dominant vector contribution, the axial component can be isolated and quantified. This enables a statistically significant extraction of both its cross section contribution and the axial-vector coupling g_A.

The structure of this thesis is as follows. Chapter 2 outlines the theoretical framework, introducing gauge theories and the electroweak sector of the SM. This chapter also covers the derivation of the V-A structure of weak interactions and Walecka's general semileptonic effective Hamiltonian [26, 31]. Chapter 3 discusses the nuclear shell model, the harmonic oscillator single-particle basis, and neutrino production mechanisms relevant to CEνNS experiments. Chapter 4 presents the results: spin-dependent nuclear structure factors, differential cross sections, and event rates for vector and axial contributions, considering various targets and sources. It concludes with a sensitivity analysis of g_{A}. Chapter 5 summarizes the main conclusions and outlines directions for future research.

Chapter 2

Theoretical Framework for Neutrino–Nucleus Scattering

2.1 Gauge theories

Symmetries in physics have an important role in governing or restricting the formulation of theories. One of the most relevant results for field theory and particle physics is provided by Noether's theorem: If an action is invariant under some group of transformations, then there exist one or more conserved quantities which are associated with these transformations [32, 33]. This concept correlates a conservation law with every continuous symmetry transformation under which the Lagrangian is invariant, and gives rise to the idea of gauge theories.

The concept of gauge theories was first introduced in the classic investigations of Hermann Weyl in 1918 [34]. Furthermore, it was established that Maxwell's equations and quantum electrodynamics (QED) are locally gauge invariant. However, the idea of generalizing the local gauge principle to non-Abelian groups was proposed only in 1954 by Yang and Mills [35]. Their construction was based on the concept introduced by Heisenberg in 1932 [36], namely isotopic spin, which provides a description of the two charge states of a nucleon. In this work Yang-Mills demonstrated that the conservation of isotopic spin is identical to the requirement of invariance of all interactions under isotopic spin rotation and presented the mathematical formulation of the idea of isotopic gauge invariance.

Gauge theories became consolidated as a unifying framework for all elementary interactions. In general, gauge theories show that when a system of fields is described by a Lagrangian invariant under local Lie group transformations, the dynamics remain unchanged. This invariance principle prescribes the introduction of vector gauge fields, whose transformation properties set their interactions with matter [37].

2.1.1 General formulation of gauge theories

In view of this, it becomes necessary to present the general formulation of gauge theories since the processes of interest occur in the electroweak sector, which is described by a non-Abelian gauge theory. Therefore, we begin considering a non-Abelian Lie group of continuous transformations $\mathcal{G}$ with N generators T_a, that satisfy the Lie algebra [38]:

$$[T_a, T_b] = i f_{abc} T_c \ , \tag{2.1.1}$$

with f_{abc} the group structure constants. Infinitesimal elements of the group can also be defined from the generators:

$$g(\epsilon) = 1 + i\epsilon \cdot T \ . \tag{2.1.2}$$

From Noether's theorem, charge conservation is a consequence of the invariance of the Lagrangian under global phase transformations [33]. In gauge theories, this symmetry is promoted to local transformations of the matter field, such that a general Lagrangian $\mathcal{L}(x)_\psi = \mathcal{L}(\psi_r(x), \partial_\mu \psi_r(x))$ must remain invariant under local phase transformations of the form

$$\psi(x) \to \psi'(x) = U(\theta(x))\, \psi(x) \ , \tag{2.1.3}$$

where $U(\theta(x)) \in \mathcal{G}$ depends on N real parameters $\theta_a(x)$.

The Lagrangian is not invariant under local gauge transformations, since the derivative term transforms as:

$$\begin{aligned} \partial_\mu \Psi(x) \ \to \ \partial_\mu \Psi'(x) &= \partial_\mu \big[U(\theta(x))\Psi(x)\big] \\ &= U(\theta(x))\, \partial_\mu \Psi(x) + \big(\partial_\mu U(\theta(x))\big)\, \Psi(x) \ . \end{aligned} \tag{2.1.4}$$

The second term breaks gauge invariance. To restore it, a gauge field $A_\mu(x)$ should be introduced [39], and ∂_μ promoted to a covariant derivative D_μ, such that $D_\mu \psi$ transforms as ψ:

$$D_\mu \psi \to \ D'_\mu \psi' = U(\theta)\, D_\mu \psi \ . \tag{2.1.5}$$

Using $\psi = U^{-1}(\theta)\psi'$, the transformation rule for D_μ follows:

$$D_\mu \to D'_\mu = U(\theta) D_\mu U^{-1}(\theta) \ . \tag{2.1.6}$$

Finally, the transformation in Eq. (2.1.6) is satisfied by the explicit definition:

$$D_\mu = \partial_\mu + igA_\mu \cdot L \ , \tag{2.1.7}$$

where g is a real constant.

The conditions in Eqs. (2.1.5), (2.1.6) and (2.1.7) are indeed satisfied. Using the definition of the covariant derivative in Eq. (2.1.7), the requirement in Eq. (2.1.6) leads directly to the transformation law of the gauge field,

$$A_\mu \cdot L \ \to \ A'_\mu \cdot L = U(\theta) \left(A_\mu \cdot L - \frac{i}{g}\, \partial_\mu \right) U^{-1}(\theta) \, . \tag{2.1.8}$$

This results in the finite transformation of the vector gauge field (as shown in the Appendix A and B),

$$A'_\mu = A_\mu + A_\mu \times \epsilon - \frac{1}{g} \partial_\mu \epsilon \, . \tag{2.1.9}$$

In conclusion, the explicit form of the variation of the gauge vector field has been derived. This result justifies the replacement of the ordinary derivative in the Lagrangian by the covariant derivative, which in turn implies the introduction of interaction terms coupling gauge fields A_μ to the matter fields ψ.

The previous discussion allows outlining the general principles for the construction of a gauge theory, namely [32]:

- Choose the gauge group G with N generators.

- Add N vector fields in a specific representation of the gauge group.
- Choose the representation, in general the fundamental representation, for the matter fields (elementary particles).
- Define the covariant derivative and write the most general renormalizable Lagrangian, invariant under $\mathcal{G}$, which couples all these fields.

2.1.2 Abelian and non-Abelian gauge symmetries

The general formalism is now applied to the two gauge relevant groups: the Abelian group U(1) and the non-Abelian group SU(2), treated separately.

Abelian group

Consider the free Dirac Lagrangian $\mathcal{L}_0 = \bar{\psi}(\not{p} - m)\psi$. Imposing invariance under local U(1) phase rotations leads to the following result:

$$\begin{aligned} \mathcal{L}_0 \to \mathcal{L}'_0 &= \overline{\psi'}(\not{p} - m)\psi' \\ &= \overline{\psi}(\not{p} - m)\psi + \overline{\psi}\gamma^\mu \partial_\mu \alpha(x)\psi \ . \end{aligned} \tag{2.1.10}$$

Thus, the gauge principle is evidently required. To consistently implement local gauge transformations, the principle of minimal coupling is employed. In this approach, the ordinary derivative is replaced by a gauge-covariant derivative as defined in Eq. (2.1.7):

$$D_\mu = \partial_\mu + ieA_\mu(x) \ . \tag{2.1.11}$$

The vector field A_μ transforms according to Eq. (2.1.9), as follows:

$$A_\mu \to A'_\mu = A_\mu + \frac{1}{e}\partial_\mu \alpha \ . \tag{2.1.12}$$

As a result, the free-particle Lagrangian is modified to a locally gauge-invariant form:

$$\begin{aligned} \mathcal{L} &= \bar{\psi}(i\gamma^\mu - m)\psi - qA_\mu \bar{\psi}\gamma^\mu \psi \\ &= \mathcal{L}_{\text{free}} - J^\mu A_\mu \, . \end{aligned} \tag{2.1.13}$$

Non-Abelian group: Yang-Mills, Isotopic spin

In the context of SU(2) formalism, the isospin theory is developed. Isospin is a new quantum number that emerges because the nucleon possesses an internal degree of freedom with two possible states: the proton and the neutron. These states are indistinguishable under the nuclear interaction. Consequently, an SU(2) symmetry arises, where the nucleon $\psi^T = (n, p)$ transforms as an SU(2) irreducible representation. This theoretical framework is mathematically analogous to spin [36, 40].

Yang and Mills extended the gauge principle to non-Abelian symmetries [35], motivated by evidence for isospin conservation and the near-equality of neutron and proton masses. They formulated the isotopic gauge principle, allowing arbitrary local orientation of the isotopic spin axes [35]. They required that physical processes, except those involving the electromagnetic field, be invariant under an isotopic gauge transformation of the form $\psi \to \psi' = S^{-1}\psi$, where S is a 2×2 unitary matrix representing a space-time dependent isotopic spin rotation [35]. This approach was inspired by Heisenberg's earlier

ideas [36].

Identifying the symmetry with SU(2) allowed the promotion of the nucleon as an isospin doublet. This development in turn paved the way for the development of the theory of weak interactions. Following on their reasoning, the nucleon field is represented by a two-component wave function ψ, corresponding to an isospin $\frac{1}{2}$ state [41]

$$\psi = \begin{pmatrix} \psi_1 \\ \psi_2 \end{pmatrix} . \tag{2.1.14}$$

This field obeys the free Dirac Lagrangian:

$$\mathcal{L}_0 = \bar{\psi}(x) \left(i\gamma^\mu \partial_\mu - m \right) \psi(x) . \tag{2.1.15}$$

Its transformation obeys:

$$\psi(x) \rightarrow \psi'(x) = \exp\left\{ \frac{-i\boldsymbol{\tau} \cdot \boldsymbol{\theta}(\boldsymbol{x})}{2} \right\} \psi(x) , \tag{2.1.16}$$

where $\boldsymbol{\tau} = (\tau_1, \tau_2, \tau_3)$ with τ_i the Pauli matrices that satisfy the Lie Algebra in Eq. (2.1.1):

$$\left[\frac{\tau_i}{2}, \frac{\tau_j}{2} \right] = i\varepsilon_{ijk} \frac{\tau_k}{2} \qquad i, j, k = 1, 2, 3 . \tag{2.1.17}$$

To ensure the local gauge invariance of the theory, the ordinary derivative is promoted to a covariant derivative which remains the form in Eq. (2.1.7):

$$D_\mu \psi = \left(I\partial_\mu + ig \frac{\boldsymbol{\tau} \cdot \boldsymbol{b}_\mu}{2} \right) \psi . \tag{2.1.18}$$

This requires the introduction of three vector fields b_μ^i $(i = 1, 2, 3)$, which transform under infinitesimal SU(2) gauge transformations as (see Appendix D for details):

$$\boldsymbol{b}'_\mu = \boldsymbol{b}_\mu - \boldsymbol{\alpha} \times \boldsymbol{b}_\mu - \frac{1}{g} \partial_\mu \boldsymbol{\alpha} . \tag{2.1.19}$$

At this stage, the isospin gauge theory of nucleons is described by the Lagrangian

$$\begin{aligned} \mathcal{L} &= \bar{\psi} \left(i\gamma^\mu D_\mu - m \right) \psi \\ &= \mathcal{L}_0 - \frac{g}{2} \boldsymbol{\tau} \cdot \bar{\psi} \gamma^\mu \psi , \end{aligned} \tag{2.1.20}$$

which consists of a free Dirac term and an interaction term coupling the fermion field to the isovector gauge fields. This structure leads to the conserved isospin current

$$\boldsymbol{j}^\mu = \bar{\psi} \gamma^\mu \frac{1}{2} \boldsymbol{\tau} \psi . \tag{2.1.21}$$

2.2 Standard Model of Electroweak Interactions

A comprehensive understanding of the weak interaction provides the theoretical basis for analyzing neutrino-nucleus scattering. As outlined in the previous section, fundamental interactions arise from electroweak theory, which is based on $\mathrm{SU}(2)_L$ weak-isospin symmetry and $\mathrm{U}(1)_Y$ phase symmetry associated with weak hypercharge.

Historically, the development of the SM began in early studies of radioactive decay, where it was established that α particles are helium nuclei and β particles are electrons. While α-decays produce monoenergetic particles consistent with two-body kinematics, β-decay was found to exhibit a continuous energy spectrum, as demonstrated by Chadwick in 1914 [42] and later confirmed through calorimetric measurements by Ellis and Wooster in 1927 [43]. This result implied that β-decay could not be a simple two-body process and posed a serious challenge to energy conservation [44]. To address the problem, Pauli suggested in 1930 the existence of a neutral, light, spin-1/2 particle emitted in β-decay [1]. The theory of β-decay was put forward years later by Fermi [45]

2.2.1 Four-Fermi interaction

Fermi built the theory of β-decay by analogy with the simplest electromagnetic interaction Hamiltonian

$$\mathcal{H}^{\mathrm{EM}}(x) = e\,\bar{p}(x)\gamma^{\alpha}p(x)\,A_{\alpha}(x)\ , \tag{2.2.1}$$

which induces the quantum transition $p \to p + \gamma$. It has the form of the scalar product of the electromagnetic vector current and the vector electromagnetic field $A^{\alpha}(x)$. Borrowing from this prescription, he postulated the following interaction Hamiltonian density for quantum transition of a neutron into a proton:

$$\mathcal{H}^{\beta}(x) = G_{\mathrm{F}}\,\bar{p}(x)\gamma^{\alpha}n(x)\,\bar{e}(x)\gamma_{\alpha}\nu(x) + \mathrm{h.c.}\ , \tag{2.2.2}$$

where G_{F} is the Fermi coupling constant and h.c. denotes the Hermitian conjugate [46].

It is important to note unlike $\mathcal{H}^{\mathrm{EM}}$, which couples two fermion fields to a boson, $\mathcal{H}^{\beta}$ involves four fermion fields. As a result of that the constants e and G_{F} possess different physical dimensions. Subsequent experiments revealed parity violation in weak interactions. To address this observation, a more general form was proposed [7]

$$\mathcal{H}_{\mathrm{W}}(x) = G_{\mathrm{F}}\sum_{i=1}^{5}\left[C_i\,(\bar{\psi}_p O_i \psi_n)(\bar{\psi}_e O^i \psi_{\nu_e}) + \mathrm{h.c.}\right]\ . \tag{2.2.3}$$

Here C_i are coupling constants and $O_{\mathrm{S,V,T,A,P}} = \{1,\ \gamma^{\alpha},\ \sigma^{\alpha\beta},\ \gamma^{\alpha}\gamma_5,\ \gamma_5\}$. They are five types of interactions: scalar, vector, tensor, axial-vector and pseudoscalar. Determining which structures are realised in nature became the central problem of weak interaction physics.

2.2.2 Parity Non-conservation

Conservation of parity (invariance under space inversion, i.e. under transition from a right-handed to a left-handed system) was firmly established for strong (hadronic) and electromagnetic processes. For many years physicists thought that this invariance is a general law of nature valid for all interactions [46]. The discovery of parity violation in the weak interaction represents one of the most significant advances in twentieth-century physics. In 1957, Lee and Yang proposed an experimental test of parity conservation in the weak interaction and were subsequently awarded the Nobel Prize [47].

In the early 1950s, the $\theta - \tau$ puzzle emerged: two mesons with nearly identical masses and lifetimes but with different parities in their decay products, suggesting they could

be the same particle. Lee and Yang resolved this in 1956 [48] by proposing parity non-conservation in weak interactions, noting the absence of any experimental evidence for parity conservation in β-decay. This was confirmed shortly after by Wu et al. [49] and Lederman et al. [50] in 1957.

Wu et al. tested this by measuring the angular distribution of electrons emitted from polarized ^{60}Co nuclei, where θ is the angle between the nuclear polarization axis and the electron momentum. Parity conservation requires a symmetric distribution under $\theta \to 180^\circ - \theta$. However, a pronounced asymmetry was observed: electrons were preferentially emitted opposite to the polarization axis ($\alpha < 0$, $|\alpha| \gtrsim 0.7$). This provided unambiguous evidence of parity violation in β-decay [46, 49].

In order to account the results of the Wu et al. and other experiments, we must assume that the Hamiltonian of the β-decay is the sum of a scalar and a pseudoscalar [7, 46]:

$$\mathcal{H}_{\rm W}^{\rm I} = \sum_{i=S,V,T,A,P} \bar{\psi}_p(x)\, O_i\, \psi_n(x)\; \bar{\psi}_e(x)\, O^i (G_i - G_i'\gamma_5)\, \psi_\nu(x) \;+\; \text{h.c.} \tag{2.2.4}$$

where the constants G_i characterize the scalar part of the Hamiltonian. While the constants G_i' characterize the pseudoscalar part. This became the most general Hamiltonian at the moment.

2.2.3 V-A theory

The discovery of parity violation in β-decay spurred enormous progress in understanding the weak interaction. This progress began with the two-component neutrino theory [46]. This theory of the neutrino became part of the universal V-A theory of the weak interaction and the main idea of the two-component theory (left-handed component of the neutrino field in the interaction Hamiltonian) was subsequently generalized, playing a key role in the further development of the theory of the weak interaction [46].

In 1957, Landau [51], Lee and Yang [47], and Salam [52] proposed the two-component neutrino theory. Let us present the field ν(x) in the form of the sum of the left-handed and the right-handed components. For $m_\nu = 0$, the chiral components decouple: $i\gamma^\alpha \partial_\alpha \nu_{L.R}(x) = 0$. Such a theory can be valid only if parity is violated. Shortly after the proposal of the two-component neutrino theory, the helicity of the neutrino was determined by the Goldhaber, Grodzins, and Sunyar experiment [53], which confirmed the two-component neutrino theory and the left-handed nature of the neutrino.

Feynman and Gell-Mann [54], as well as Marshak and Sudarshan [55], extended this framework by applying left-handedness to all fermion fields in the weak interaction Hamiltonian, rather than restricting it to the neutrino. According to this approach, the β-decay Hamiltonian assumes the form

$$\mathcal{H}_{\rm I}^{\beta} = \sum_{i=S,V,T,A,P} G_i\, \bar{p}_L\, O_i\, n_L\; \bar{e}_L\, O^i\, \nu_L + \text{h.c.}\,, \tag{2.2.5}$$

where $f_L = \frac{1-\gamma_5}{2} f$ denotes the left-handed component of field f. The explicit representation of the leptonic bilinear in terms of full Dirac fields is [46]

$$\bar{e}_L\, O_i\, \nu_L = \bar{e}\, \frac{1+\gamma_5}{2}\, O_i\, \frac{1-\gamma_5}{2}\, \nu\,. \tag{2.2.6}$$

Applying the left-handed prescription, the S, T, and P terms vanish [7], while the V and A terms are related by

$$\frac{1+\gamma_5}{2}\,\gamma_\alpha\gamma_5\,\frac{1-\gamma_5}{2} = -\frac{1+\gamma_5}{2}\,\gamma_\alpha\,\frac{1-\gamma_5}{2}\,. \tag{2.2.7}$$

This leads to a unique four-fermion Hamiltonian:

$$\mathcal{H}_{\rm I}^{\beta} = \frac{G_F}{\sqrt{2}}\,4\bar{p}_L\gamma_\alpha n_L\;\bar{e}_L\gamma^\alpha\nu_L + \text{h.c.} = \frac{G_F}{\sqrt{2}}\,\bar{p}\,\gamma_\alpha(1-\gamma_5)n\;\bar{e}\,\gamma^\alpha(1-\gamma_5)\nu + \text{h.c.}\,. \tag{2.2.8}$$

This formulation establishes the V-A (vector minus axial vector) current–current structure

$$\mathcal{H}_{\rm W} = \frac{G_F}{\sqrt{2}}\,J_\alpha^\dagger\,J^\alpha\,, \tag{2.2.9}$$

where J^α denotes a purely left-handed V-A current. Characterized by the single Fermi constant $G_{\rm F}$, this theory restores the universality of the weak interaction and is in excellent agreement with all charged-current experimental data.

2.2.4 $\boldsymbol{SU(2)_L \times U(1)_Y}$

The V−A current×current theory of the weak interaction represented a major step forward in the understanding of weak processes and neutrino physics. The proposal by Feynman and Gell-Mann, as well as Marshak and Sudarshan, that only left-handed components of fermion fields enter the charged-current (CC) Hamiltonian was strongly motivated by experimental evidence, in particular the success of the two-component neutrino theory [46].

In this framework, the charged weak interaction for a generic lepton ℓ is described by the current

$$J_\alpha^+ = \bar{\ell}\gamma_\alpha(1-\gamma_5)\nu = 2\,\bar{\ell}_L\gamma_\alpha\nu_L\;, \tag{2.2.10}$$

which explicitly involves only left-handed fields. This is a charged current, as it connects a charged lepton with a neutral neutrino. The chiral structure naturally suggests organizing leptons into left-handed isospin doublets [32]

$$\psi_L^{\rm lep}(x) = \begin{pmatrix}\nu_L\\ \ell_L\end{pmatrix}\;. \tag{2.2.11}$$

This structure is consistent with an SU(2) symmetry acting only on left-handed fields, denoted as $\mathrm{SU}(2)_L$.

Following the Yang–Mills construction, the interaction Lagrangian can be written as

$$\mathcal{L}_{\rm I} = -g\,\boldsymbol{j}_\alpha\cdot\boldsymbol{b}^\alpha\,, \tag{2.2.12}$$

where $\boldsymbol{b}_\alpha$ are the gauge fields associated with $\mathrm{SU}(2)_{\ L}$ and $\boldsymbol{j}_\alpha$ are the corresponding currents. Explicitly,

$$\begin{aligned}\mathcal{L}_{\rm I} &= -g\left(j_\alpha^1 b^{1\alpha} + j_\alpha^2 b^{2\alpha} + j_\alpha^3 b^{3\alpha}\right)\\ &= -g\,\bar{\psi}\gamma_\alpha\frac{\boldsymbol{\tau}}{2}\psi\cdot\boldsymbol{b}^\alpha\,.\end{aligned} \tag{2.2.13}$$

Introducing the combinations

$$j_\alpha = 2\, j_\alpha^{1+i2}, \qquad W_\alpha = \frac{1}{\sqrt{2}}\, b_\alpha^{1-i2}, \tag{2.2.14}$$

where $j_\alpha^{1\pm i2} = j_\alpha^1 \pm i\, j_\alpha^2$ and $b_\alpha^{1\pm i2} = b_\alpha^1 \pm i\, b_\alpha^2$. The interaction Lagrangian becomes

$$\mathcal{L}_{\rm I}(x) = \left(-\frac{g}{2\sqrt{2}}\, j_\alpha(x)\, W^\alpha(x) + \text{h.c.}\right) - g\, j_\alpha^3(x)\, b^{\alpha 3}(x)\ . \tag{2.2.15}$$

The current $j_\alpha(x)$ corresponds to the charged current and reproduces Eq. (2.2.10), while the third component,

$$j_\alpha^3(x) = \bar\psi(x)\gamma_\alpha \frac{1}{2}\tau_3\psi(x), \tag{2.2.16}$$

leads to a neutral current interaction. However, this neutral current cannot be identified with the electromagnetic current, since it involves only left-handed fields, whereas the electromagnetic interaction couples to both chiralities. This observation indicates that an additional symmetry is required therefore, hypercharge current is introduced [32],

$$J_\mu^Y = \bar\nu_L\gamma_\mu\nu_L + \bar\ell_L\gamma_\mu\ell_L + 2\,\bar\ell_R\gamma_\mu\ell_R\ , \tag{2.2.17}$$

associated with a $\mathrm{U}(1)_Y$ gauge symmetry. The electromagnetic current is then obtained as the linear combination

$$J_\mu^{\rm em} = J_\mu^3 + \frac{1}{2}\, J_\mu^Y\ , \tag{2.2.18}$$

which leads to the relation between the conserved charges $Q = T_3 + \frac{1}{2}Y$ known as the Gell-Mann–Nishijima relation [56, 57].

Therefore, the minimal gauge structure that unifies weak and electromagnetic interactions is given by the group

$$\mathrm{SU}(2)_L \otimes \mathrm{U}(1)_Y\ . \tag{2.2.19}$$

The symmetry group $\mathrm{SU}(2)_L$ associated to left-handed fermions satisfies the Lie algebra and contains three generators. While the symmetry group $\mathrm{U}(1)_Y$, known as hypercharge, possesses a single generator these constitutes the basis of the electroweak theory [7].

2.2.5 Electroweak Lagrangian for fermions

The gauge structure developed in Section 2.1.1, when combined with the V-A structure of the weak current, determines the form of the electroweak Lagrangian. Local $\mathrm{SU}(2)_L\times\mathrm{U}(1)_Y$ invariance is ensured by introducing the covariant derivative, as presented in Eqs. (2.1.18) and (2.1.11). This approach introduces three gauge fields A_i^α $(i = 1, 2, 3)$ associated with $\mathrm{SU}(2)_L$ and one gauge field B_α corresponding to the generator Y of $\mathrm{U}(1)_Y$ are introduced. Consequently, the covariant derivative for the unified group is given by:

$$D_\alpha = \partial_\alpha + ig\frac{1}{2}\boldsymbol{\tau}\cdot\boldsymbol{A}_\alpha + ig' B_\alpha \frac{Y}{2}\ , \tag{2.2.20}$$

where g and g' are the coupling constants of $\mathrm{SU}(2)_L$ and $\mathrm{U}(1)_Y$, respectively.

With the gauge structure in place, the left-handed fermion content is fixed as $\mathrm{SU}(2)_L$

doublets [7],

$$\psi_{eL}^{\text{lep}} = \begin{pmatrix} \nu_{eL} \\ e_L \end{pmatrix}, \qquad \psi_{\mu L}^{\text{lep}} = \begin{pmatrix} \nu_{\mu L} \\ \mu_L \end{pmatrix}, \qquad \psi_{\tau L}^{\text{lep}} = \begin{pmatrix} \nu_{\tau L} \\ \tau_L \end{pmatrix}, \tag{2.2.21}$$

$$\psi_{1L}^{q} = \begin{pmatrix} u_L \\ d_L \end{pmatrix}, \qquad \psi_{2L}^{q} = \begin{pmatrix} c_L \\ s_L \end{pmatrix}, \qquad \psi_{3L}^{q} = \begin{pmatrix} t_L \\ b_L \end{pmatrix}. \tag{2.2.22}$$

while Right-handed components are singlets. The covariant derivative in Eq. (2.2.20) acts on each multiplet as follows:

$$\partial_\alpha \psi_{iL}^{\text{lep}}(x) \longrightarrow \left(\partial_\alpha + ig\frac{1}{2}\tau^j A_\alpha^j(x) + ig'\frac{1}{2}Y_L^{\text{lep}} B_\alpha(x)\right)\psi_{iL}^{\text{lep}}(x)\ , \tag{2.2.23}$$

$$\partial_\alpha \psi_{iL}^{q}(x) \longrightarrow \left(\partial_\alpha + ig\frac{1}{2}\tau^j A_\alpha^j(x) + ig'\frac{1}{2}Y_L^{q} B_\alpha(x)\right)\psi_{iL}^{q}(x) \tag{2.2.24}$$

for left-handed leptons and quarks, respectively. Since right-handed fields are singlets, they couple only to $\mathrm{U}(1)_Y$,

$$\partial_\alpha \ell_R(x) \longrightarrow \left(\partial_\alpha + ig'\frac{1}{2}Y_R^{\text{lep}} B_\alpha(x)\right)\ell_R(x) \tag{2.2.25}$$

$$\partial_\alpha q_R(x) \longrightarrow \left(\partial_\alpha + ig'\frac{1}{2}Y_R^{\text{up}} B_\alpha(x)\right) q_R(x), \qquad q = u,\, c,\, t \tag{2.2.26}$$

$$\partial_\alpha d_R(x) \longrightarrow \left(\partial_\alpha + ig'\frac{1}{2}Y_R^{\text{down}} B_\alpha(x)\right) d_R(x), \qquad d = d,\, s,\, b\ . \tag{2.2.27}$$

for right-handed leptons and up-down quarks, respectively. By substituting these expressions into the Dirac Lagrangian and omitting the mass term, the resulting interaction Lagrangian is obtained. The derivation for leptons and quarks is presented separately below.

Lagrangian for leptons

Begin with the interaction Lagrangian for leptons, and we have (for details, see Appendix E.1):

$$\mathcal{L}_{\text{I}}^{\text{lep}} = g'\,\bar{\ell}_R\gamma^\mu B_\mu \ell_R - g\,\bar{\psi}_{iL}^{\text{lep}}\gamma^\mu\frac{\tau^a}{2}A_\mu^a\psi_{iL}^{\text{lep}} + g'\,\frac{1}{2}\,\bar{\psi}_{iL}^{\text{lep}}\gamma^\mu B_\mu\psi_{iL}^{\text{lep}}\ . \tag{2.2.28}$$

To derive the explicit interaction terms for the fermions, we consider, for simplicity, the first generation [58]. The leptonic interaction Lagrangian reads

$$\mathcal{L}_{\text{I}}^{\text{lep}} = g'\,\bar{e}_R \not{B} e_R - \frac{1}{2}\begin{pmatrix}\bar{\nu}_{eL} & \bar{e}_L\end{pmatrix}\begin{pmatrix} g\not{A}_3 - g'\not{B} & g(\not{A}_1 - i\not{A}_2) \\ g(\not{A}_1 + i\not{A}_2) & -g\not{A}_3 - g'\not{B}\end{pmatrix}\begin{pmatrix}\nu_{eL} \\ e_L\end{pmatrix}. \tag{2.2.29}$$

This expression naturally separates into CC and neutral-current (NC) contributions. The CC interaction arises from the off-diagonal terms and introducing the charged gauge field $W_\mu = \frac{A_\mu^1 - iA_\mu^2}{\sqrt{2}}$, the CC Lagrangian takes the form

$$\mathcal{L}_{\text{I},L}^{(\text{CC})} = -\frac{g}{\sqrt{2}}\left[\bar{\nu}_{eL}\not{W} e_L + \bar{e}_L\not{W}^\dagger\nu_{eL}\right]\ , \tag{2.2.30}$$

which, becomes the familiar V-A structure:

$$\mathcal{L}_{\mathrm{I},L}^{(\mathrm{CC})} = -\frac{g}{2\sqrt{2}}\,\bar{\nu}_e\gamma^\mu(1-\gamma^5)e\,W_\mu + \mathrm{H.c.} \tag{2.2.31}$$

$$= -\frac{g}{2\sqrt{2}}\,j^\mu_{W,L}W_\mu + \mathrm{H.c.}\ . \tag{2.2.32}$$

The diagonal terms lead to the neutral-current (NC) interaction. Additionally, the electromagnetic interaction must be included, as previously discussed. For this purpose, the electromagnetic field A_μ is expressed as a suitable linear combination of B_μ.

$$\begin{aligned}\begin{pmatrix} A_\mu \\ Z_\mu \end{pmatrix} &= \begin{pmatrix} \cos\theta_W & \sin\theta_W \\ -\sin\theta_W & \cos\theta_W \end{pmatrix}\begin{pmatrix} B_\mu \\ A^3_\mu \end{pmatrix}\ , \\ A^3_\mu &= \sin\theta_W\ A_\mu - \cos\theta_W\ Z_\mu \\ B_\mu &= \cos\theta_W\ A_\mu + \sin\theta_W\ Z_\mu\ .\end{aligned} \tag{2.2.33}$$

At this stage, the Brout–Englert–Higgs mechanism [59, 60] is explicitly realized. This mechanism spontaneously breaks $\mathrm{SU}(2)_L\times\mathrm{U}(1)_Y$ symmetry down to $\mathrm{U}(1)_{\mathrm{em}}$. As a result, it generates masses for the weak gauge bosons while leaving the photon massless. Consequently, the neutral gauge fields A^3_μ and B_μ mix to form the physical mass eigenstates Z_μ and A_μ (the photon). This mixing is described by a rotation in field space parameterized by the Weinberg angle θ_W.

Substituting Eq. (2.2.33) into NC interaction, one obtains

$$\begin{aligned}\mathcal{L}_{\mathrm{I},L}^{(\mathrm{NC})} = -\frac{1}{2}\Bigg\{ &\bar{\nu}_{eL}\Big[(g\cos\vartheta_W + g'\sin\vartheta_W)\not{Z} + (g\sin\vartheta_W - g'\cos\vartheta_W)\not{A}\Big]\nu_{eL} \\ &- \bar{e}_L\Big[(g\cos\vartheta_W - g'\sin\vartheta_W)\not{Z} + (g\sin\vartheta_W + g'\cos\vartheta_W)\not{A}\Big]e_L \\ &- 2g\,\bar{e}_R\Big[-\sin\vartheta_W\not{Z} + \cos\vartheta_W\not{A}\Big]e_R\Bigg\}\ .\end{aligned} \tag{2.2.34}$$

The condition of neutrino electromagnetic neutrality fixes $\tan\theta_W = g'/g$ and identifies the electric charge as $e = g\sin\theta_W = g'\cos\theta_W$. The neutral-current Lagrangian is then

$$\mathcal{L}_{\mathrm{I},L}^{(\mathrm{NC})} = -\frac{g}{2\cos\theta_W}\sum_{\psi_i=\nu,\ell}\bar{\psi}_i\gamma^\mu\left(g_V^i - g_A^i\gamma_5\right)\psi_i Z_\mu + e\,\bar{\ell}\gamma^\mu A_\mu\ell\ , \tag{2.2.35}$$

with

$$g_V^i = T_3^i - 2Q_i\sin^2\theta_W \text{ and } g_A^i T_3^i. \tag{2.2.36}$$

Lagrangian for quarks

The quark interaction Lagrangian follows the same procedure as for leptons, differing only in the hypercharge assignments (see Appendix E.2):

$$\mathcal{L}_{\mathrm{I}}^q = -\frac{2}{3}g'\,\bar{u}_{iR}\gamma^\mu B_\mu u_{iR} + \frac{1}{3}g'\,\bar{d}_{iR}\gamma^\mu B_\mu d_{iR} - \frac{1}{2}\bar{\psi}^q_{iL}\left(g\gamma^\mu\tau^a A^a_\mu - \frac{1}{3}g'\gamma^\mu B_\mu\right)\psi^q_{iL}\ .$$

Restricting to the first generation [58]:

$$\mathcal{L}_{\mathrm{I},Q} = -\frac{1}{2}\begin{pmatrix}\bar{u}_L & \bar{d}_L\end{pmatrix}\begin{pmatrix}gA_3 + \frac{1}{3}g'B & g(A_1 - iA_2) \\ g(A_1 + iA_2) & -gA_3 + \frac{1}{3}g'B\end{pmatrix}\begin{pmatrix}u_L \\ d_L\end{pmatrix} - \frac{2}{3}g'\,\bar{u}_R B u_R + \frac{1}{3}g'\,\bar{d}_R B d_R\ . \tag{2.2.37}$$

The charged-current Lagrangian is:

$$\mathcal{L}^{(\mathrm{CC})}_{\mathrm{I},Q} = -\frac{g}{2\sqrt{2}}\, j^{\mu}_{W,Q} W_{\mu} + \mathrm{H.c.}\ , \tag{2.2.38}$$

where the quark CC is $j^{\mu}_{W,Q} = \bar{u}\,\gamma^{\mu}(1-\gamma^5)\,d = 2\,\bar{u}_L\gamma^{\mu}d_L$.

The NC Lagrangian $\mathcal{L}^{(\mathrm{NC})}_{I,q} = \mathcal{L}^{(Z)}_{I,q} + \mathcal{L}^{(\gamma)}_{I,q}$ takes the same form as for leptons, with

$$\mathcal{L}^{(\gamma)}_{\mathrm{I},q} = -e\, j^{\mu}_{\gamma,q} A_{\mu} \quad \text{and} \quad \mathcal{L}^{(Z)}_{\mathrm{I},q} = -\frac{g}{2\cos\theta_W} j^{\mu}_{Z,q} Z_{\mu}\ , \tag{2.2.39}$$

where the quark electromagnetic current and the weak neutral current are:

$$j^{\mu}_{\gamma,Q} = \frac{2}{3}\,\bar{u}\gamma^{\mu}u - \frac{1}{3}\,\bar{d}\gamma^{\mu}d\ , \tag{2.2.40}$$

$$j^{\mu}_{Z,L} = \sum_{\psi_q = u,\ldots,c} \bar{\psi}_q \gamma^{\mu}(g^q_V - g^q_A\gamma_5)\psi_q\ Z_{\mu}\ . \tag{2.2.41}$$

with g^q_V and g^q_A as defined in Eq. (2.2.36).

2.3 Semileptonic Weak interactions

Throughout this section, the notation established by Walecka and detailed in Appendix G is employed. While this notation may differ from conventions used elsewhere in this work, it is adopted to maintain consistency with the seminal literature on semileptonic weak interactions [26, 31].

2.3.1 Effective theory

In physical situations characterized by a clear separation of energy scales, the appropriate theoretical framework is provided by an effective field theory (EFT). The central idea of an EFT is that the dynamics at low energies can be described independently of the detailed structure, whose effects are encoded in a set of higher-dimensional operators. Within this framework, one constructs the most general Lagrangian consistent with the symmetries of the system. Unlike fundamental renormalizable theories (where only operators of canonical dimension four or less are retained) an EFT systematically includes operators of dimension greater than four [61].

Weak interactions are governed by Eqs. (2.2.32), (2.2.35), (2.2.38), and (2.2.39), which specify the interactions between fermions and gauge bosons. In the low-energy nuclear regime, where $q^2 \ll M_W^2$ and M_Z^2, the intermediate bosons are significantly off-shell. As a result, the electroweak Lagrangian reduces to an effective current-current interaction [31, 62]. For nuclear applications, it is important to note that the relevant processes involve the semileptonic components of the effective low-energy Lagrangian, as explicitly provided

in [31]:

$$\mathcal{L}_{\text{eff}}^{(\pm)} = \frac{iG}{\sqrt{2}}\Big\{\left[\bar{\psi}_\ell\gamma_\mu(1+\gamma_5)\psi_{\nu_\ell}\right]\mathcal{J}_\mu^{(+)}(\text{hadrons}) + \left[\bar{\psi}_{\nu_\ell}\gamma_\mu(1+\gamma_5)\psi_\ell\right]\mathcal{J}_\mu^{(-)}(\text{hadrons})\Big\}\ , \tag{2.3.1a}$$

$$\mathcal{L}_{\text{eff}}^{(0)\nu} = \frac{iG}{\sqrt{2}}\left[\bar{\psi}_{\nu_\ell}\gamma_\mu(1+\gamma_5)\psi_{\nu_\ell}\right]\mathcal{J}_\mu^{(0)}(\text{hadrons})\ , \tag{2.3.1b}$$

$$\mathcal{L}_{\text{eff}}^{(0)\ell} = -\frac{iG}{\sqrt{2}}\Big[\bar{\psi}_\ell\gamma_\mu(1+\gamma_5)\psi_\ell - 4\sin^2\theta_W\,\bar{\psi}_\ell\gamma_\mu\psi_\ell\Big]\mathcal{J}_\mu^{(0)}(\text{hadrons})\ . \tag{2.3.1c}$$

The effective Lagrangians form the basis for the neutrino-nucleus scattering cross section in the subsequent sections.

2.3.2 Semileptonic Matrix Element

The process under consideration is the interaction between a neutrino and a nucleus, governed by the second term of Eq. (2.3.1). At energies significantly below the Z boson mass, this interaction is described by an effective semileptonic Hamiltonian of the following form:

$$\hat{H}_{\text{W}} = -\frac{G_{\text{F}}}{\sqrt{2}}\int d\boldsymbol{x}\, j_\mu^{\text{leptonic}}\hat{\mathcal{J}}_\mu(\boldsymbol{x})\ , \tag{2.3.2}$$

Here $\hat{\mathcal{J}}_\mu$ denotes the nuclear current and j_μ^{leptonic} the leptonic current. Working to first order in the weak coupling constant, the leptonic sector is treated perturbatively, while the hadronic sector requires a non-perturbative treatment due to the strong interaction.

The transition matrix element of the effective Hamiltonian between the initial state $|k_1, i\rangle$, which consists of a lepton with four-momentum k_1 and a nucleus in state i, and the final state $\langle k_2, f|$, comprising a lepton with four-momentum k_2 and a nucleus in state f, is given by

$$\langle\ k_2\ , f\ |\hat{H}_{\text{W}}|\ k_1\ , i\ \rangle = -\frac{G_{\text{F}}}{\sqrt{2}}\int d\boldsymbol{x}\,\langle\ k_2\ , f\ |\, j_\mu^{\text{lep}}\hat{\mathcal{J}}_\mu(\boldsymbol{x})\,|\ k_1\ , i\ \rangle\ . \tag{2.3.3}$$

Here the leptonic matrix element, derived in Appendix H, is expressed as follows:

$$\begin{aligned}\langle k_2, s'|j_\mu^{\text{lep}}|k_1, s\rangle &= \bar{u}_{s'}(k_2)e^{i\boldsymbol{k}_2\cdot\boldsymbol{x}}\gamma^\mu(1+\gamma^5)u_s(k_1)e^{-i\boldsymbol{k}_1\cdot\boldsymbol{x}}\\ &= \hat{\ell}_\mu e^{-i\boldsymbol{q}\cdot\boldsymbol{x}}\end{aligned} \tag{2.3.4}$$

with $\quad\boldsymbol{q} = k_1 - k_2$.

Decomposing the four-vector as $x_\mu = (\vec{x}, ix_0)$ and separating the temporal and spatial components yields the following expression for the Hamiltonian matrix element:

$$\langle f, k_2|\hat{H}_{\text{W}}|k_1, i\rangle = -\frac{G_{\text{F}}}{\sqrt{2}}\int d^3\boldsymbol{x}\ e^{-i\boldsymbol{q}\cdot\boldsymbol{x}}\left[l_0\mathcal{J}_0(\boldsymbol{x})_{fi} - \vec{l}\cdot\vec{\mathcal{J}}(\boldsymbol{x})_{fi}\right]\ . \tag{2.3.5}$$

At this stage, the only assumptions are the existence of a local current density operator $\hat{\mathcal{J}}_\mu(\boldsymbol{x})$ for the target and that the target is sufficiently localized in space such that partial integrations on the transition matrix elements $\langle f|\hat{\mathcal{J}}_\mu(\boldsymbol{x})|i\rangle \equiv \hat{\mathcal{J}}_\mu(\boldsymbol{x})_{fi}$ [26].

2.3.3 Multipole analysis of the nuclear matrix element

Multipole expansion for plane wave

We utilize a multipole expansion of the hadronic current matrix element to project irreducible tensor operators (ITOs). This approach provides a systematic framework for applying angular momentum algebra and strong isospin symmetry to evaluate nuclear matrix elements. The procedure begins with the expansion of a plane wave (see Appendix I for details),

$$e^{ikr\cos\theta} = \sum_{l=0}^{\infty} \sqrt{4\pi(2l+1)}\, i^l\, j_l(kr)\, Y_{l0}(\Omega)\,. \tag{2.3.6}$$

This expansion distinguishes the radial dependence, represented by the spherical Bessel functions $j_l(kr)$, from the angular dependence, described by the spherical harmonics $Y_{l0}(\Omega)$.

To account for the vector nature of the current, vector spherical harmonics are introduced and defined using Clebsch–Gordan coefficients

$$Y_{lm} e_\lambda = \sum_{JM} \langle l\ m\ 1\ \lambda | l\ 1\ J\ M\rangle\, \mathbf{Y}^M_{Jl1}\ . \tag{2.3.7}$$

This relation enables the coupling between orbital angular momentum and the spin-1 structure associated with the polarization vector e_λ. Multiplying the plane wave expansion by the polarization vector $e_{\lambda\boldsymbol{k}}$ transforms the plane wave into a representation explicitly expressed in terms of vector spherical harmonics

$$\begin{aligned} e_{\lambda\boldsymbol{k}} e^{i\boldsymbol{k}\cdot\boldsymbol{r}} &= e_{\lambda\boldsymbol{k}} \sum_l i^l \sqrt{4\pi(2l+1)} j_l(kr) Y_{l0}(\Omega) \\ &= \sum_l \sum_J i^l \sqrt{4\pi(2l+1)} j_l(kr) \langle l\ 0\ 1\ \lambda |\ l\ 1\ J\ \lambda\rangle \mathbf{Y}^\lambda_{Jl1}\ . \end{aligned} \tag{2.3.8}$$

The allowed contributions to this expansion are determined by angular momentum selection rules. The Clebsch–Gordan coefficients in this expression can be evaluated through their relationship to $3j$ symbols [63, 64], resulting in a significant simplification. Following this procedure, the expansion assumes the form

$$\begin{aligned} e_{\lambda\boldsymbol{k}} e^{i\boldsymbol{k}\cdot\boldsymbol{r}} = -\sum_{J\geq 1} \sqrt{2\pi(2J+1)}\, i^J \Bigg[& \lambda\, j_J(kr)\, \mathbf{Y}^\lambda_{JJ1} \\ & + i\sqrt{\frac{J+1}{2J+1}}\, j_{J-1}(kr)\, \mathbf{Y}^\lambda_{J\,J-1\,1} \\ & - i\sqrt{\frac{J}{2J+1}}\, j_{J+1}(kr)\, \mathbf{Y}^\lambda_{J\,J+1\,1} \Bigg]\ . \end{aligned} \tag{2.3.9}$$

This expression clearly reveals the structure of the multipole decomposition in terms of well-defined angular momentum components.

A more concise formulation is achieved by utilizing the properties of vector spherical harmonics (see Appendix J). In particular, the previous expression can be expressed in terms of a transverse component and a curl term, leading to the following multipole

expansion [31]

$$e_{\lambda \boldsymbol{k}} e^{i\boldsymbol{k}\cdot\boldsymbol{r}} = -\sum_{J\geq 1} \sqrt{2\pi(2J+1)}\, i^J \left[\lambda j_J(kr)\mathbf{Y}^{\lambda}_{JJ1} + \frac{1}{k}\nabla \wedge \left(j_J(kr)\mathbf{Y}^{\lambda}_{JJ1}\right)\right]. \tag{2.3.10}$$

The corresponding adjoint relation is derived as follows [31]

$$e^{\dagger}_{\lambda \boldsymbol{k}} e^{-i\boldsymbol{k}\cdot\boldsymbol{r}} = -\sum_{J\geq 1} \sqrt{2\pi(2J+1)}\, (-i)^J \left[\lambda j_J(kr)\mathbf{Y}^{-\lambda}_{JJ1} + \frac{1}{k}\nabla \wedge \left(j_J(kr)\mathbf{Y}^{-\lambda}_{JJ1}\right)\right] . \tag{2.3.11}$$

For clarity, we adopt the notation $\boldsymbol{k} = |\boldsymbol{q}|$. Additionally, it is useful to consider the longitudinal component of the expansion. Beginning with Eq. (2.3.6), an alternative representation involving the scalar polarization component can be derived as follows:

$$\begin{aligned} e^{i\boldsymbol{k}\cdot\boldsymbol{x}} e_{k0} &= \sum_{J=0}^{\infty} [4\pi(2J+1)]^{1/2}\ \ i^J\ j_J(kx) e_{\boldsymbol{k}0} Y_{J0}(\Omega) \\ &= \sum_{J=0}^{\infty} [4\pi(2J+1)]^{1/2}\, i^J\ j_J(kx)\ \langle l\ 0\ 1\ 0 | l\ 1\ J\ 0\rangle \mathbf{Y}^0_{Jl1}(\Omega)\ . \end{aligned} \tag{2.3.12}$$

This result is obtained by applying the properties outlined in Appendix (J):

$$e^{-i\boldsymbol{k}\cdot\boldsymbol{x}} e_{k0} = \sum_{J=0}^{\infty} \sqrt{4\pi(2J+1)}\, (i)^J \nabla(j_J(kx), Y_{J0}(\Omega))\ . \tag{2.3.13}$$

The corresponding adjoint representation is given by:

$$e^{-i\vec{k}\cdot\vec{x}} e_{k0} = \sum_{J=0}^{\infty}\ \sqrt{4\pi(2J+1)}(-i)^J\, \nabla(j_J(kx) Y_{J0}(\Omega))\ . \tag{2.3.14}$$

Multipole analysis

The multipole expansion of the leptonic plane wave in terms of vector spherical harmonics, as established in the previous section, forms the basis for a systematic decomposition of the current matrix element. Expressing the leptonic current in this basis enables the matrix element to be written in terms of irreducible tensor operators (ITOs), thereby allowing identification and classification of the contributing nuclear multipoles.

A systematic angular momentum decomposition is achieved by considering the leptonic current $\boldsymbol{l}$ in the spherical basis [26], which is particularly sizable for coupling to tensor operators in isospin space. The current is expanded as $\boldsymbol{l} = \sum_\lambda l_\lambda e^{\dagger}_{\lambda}$, where the spherical basis vectors e_λ are defined with respect to the momentum transfer direction $\boldsymbol{q}$ as [31, 65]:

$$e_{\pm} \equiv \mp\frac{1}{\sqrt{2}}(e_{q1} \pm i e_{q2}), \qquad e_0 \equiv \frac{\boldsymbol{q}}{|\boldsymbol{q}|}, \qquad e^{\dagger}_{\lambda} = (-1)^{\lambda} e_{-\lambda}\ . \tag{2.3.15}$$

The corresponding spherical components $l_\lambda = e_\lambda \cdot \boldsymbol{l}$ are given explicitly by

$$l_{\pm 1} = \pm\frac{1}{\sqrt{2}}(l_1 \mp i l_2), \qquad l_0 = l_3\ . \tag{2.3.16}$$

Substituting this decomposition into Eq. (2.3.5) and separating the vector and scalar contributions of the nuclear current, one obtains:

$$\langle f|\hat{H}_{\rm w}|i\rangle = -\frac{G_{\rm F}}{\sqrt{2}}\int d\boldsymbol{x} e^{-i\boldsymbol{q}\cdot\boldsymbol{x}}\big[\sum_{\lambda} l_\lambda e^\dagger_\lambda \cdot \boldsymbol{\mathcal{J}}(\boldsymbol{x})_{fi} - l_0\mathcal{J}(x)_{fi}\big] \ . \tag{2.3.17}$$

The analysis begins with the vector contribution, specifically $\sum_\lambda e^{-i\boldsymbol{q}\cdot\boldsymbol{x}} l_\lambda e^\dagger_\lambda \cdot \boldsymbol{\mathcal{J}}(\boldsymbol{x})_{fi}$. Applying the multipole expansion of the plane wave from Eq. (2.3.11) and Eq. (2.3.14), the expression is transformed as follows:

$$\begin{aligned}\sum_{\lambda} e^{-i\boldsymbol{q}\cdot\boldsymbol{x}} l_\lambda e^\dagger_\lambda \cdot \boldsymbol{\mathcal{J}}(\boldsymbol{x})_{fi} = \Bigg[&\sum_{\lambda=\pm1} l_\lambda \times -\sum_{J\geq 1}\sqrt{2\pi(2J+1)}(-i)^J \\ &\left\{\lambda\, j_J(kr)\mathbf{Y}^{-\lambda}_{JJ1} + \frac{1}{k}\nabla\wedge\big(j_J(kr)\mathbf{Y}^{-\lambda}_{JJ1}\big)\right\} \\ &+ l_3\frac{i}{k}\sum_{J\geq 0}\sqrt{4\pi(2J+1)}(-i)^J\nabla(j_J(kr)Y_{J0})\Bigg]\cdot\boldsymbol{\mathcal{J}}(\boldsymbol{x}) \ ,\end{aligned} \tag{2.3.18}$$

Collecting terms, the vector contribution to the matrix element takes the form:

$$\begin{aligned}-\frac{G_{\rm F}}{\sqrt{2}}\int d^3\boldsymbol{x}\, e^{-i\boldsymbol{q}\cdot\boldsymbol{x}}\sum_\lambda l_\lambda e^\dagger_\lambda\cdot\boldsymbol{\mathcal{J}}(\boldsymbol{x})_{fi} = -\frac{G_{\rm F}}{\sqrt{2}}\langle f|\Bigg\{ &\sum_{\lambda=\pm1} l_\lambda \sum_{J\geq 1}\sqrt{2\pi(2J+1)}(-i)^J \\ &\Bigg[\lambda\int d^3\boldsymbol{x}\, j_J(kr)\mathbf{Y}^{-\lambda}_{JJ1}\cdot\boldsymbol{\mathcal{J}} \\ &\quad + \frac{1}{k}\int d^3\boldsymbol{x}\,\nabla\wedge\big(j_J(kr)\mathbf{Y}^{-\lambda}_{JJ1}\big)\cdot\boldsymbol{\mathcal{J}}\Bigg] \\ &+ l_3\sum_{J\geq 0}\sqrt{4\pi(2J+1)}(-i)^J\int d^3\boldsymbol{x}\,\frac{i}{k}\nabla\left(j_J(kr)Y_{J0}\right)\cdot\boldsymbol{\mathcal{J}}\Bigg\}|i\rangle \ .\end{aligned} \tag{2.3.19}$$

The scalar contribution is evaluated in an analogous manner. By applying the plane wave expansion from Eq. (2.3.6), the following expression is obtained:

$$\frac{G_{\rm F}}{\sqrt{2}}\int d^3\boldsymbol{x}\, e^{-i\boldsymbol{q}\cdot\boldsymbol{x}} l_0\mathcal{J}_{0_{fi}} = \frac{G_{\rm F}}{\sqrt{2}}\langle f|\ l_0\sum_{J=0}(-i)^J\sqrt{4\pi(2J+1)}\int d^3\boldsymbol{x}\big[j_J(kr)Y_{J0}\mathcal{J}_0\big]\ |i\rangle \ . \tag{2.3.20}$$

Equations (2.3.19) and (2.3.20) both reveal the presence of multipole operators [31]:

$$\hat{\mathcal{M}}_{JM}(k) = \hat{M}_{JM} + \hat{M}^5_{JM} = \int d^3x\ j_J(kx)\, Y_{JM}(\Omega_x)\,\hat{\mathcal{J}}_0(\boldsymbol{x}) \ , \tag{2.3.21}$$

$$\hat{\mathcal{L}}_{JM}(k) = \hat{L}_{JM} + \hat{L}^5_{JM} = \frac{i}{k}\int d^3x\ \big[\nabla\big(j_J(kx)Y_{JM}(\Omega_x)\big)\big]\cdot\hat{\boldsymbol{\mathcal{J}}}(\boldsymbol{x}) \ , \tag{2.3.22}$$

$$\hat{\mathcal{T}}^{\rm el}_{JM}(k) = \hat{T}^{\rm el}_{JM} + \hat{T}^{\rm el\,5}_{JM} = \frac{1}{k}\int d^3x\ \Big[\nabla\times\big(j_J(kx)\,\vec{Y}^M_{JJ1}(\Omega_x)\big)\Big]\cdot\hat{\boldsymbol{\mathcal{J}}}(\boldsymbol{x}) \ , \tag{2.3.23}$$

$$\hat{\mathcal{T}}^{\rm mag}_{JM}(k) = \hat{T}^{\rm mag}_{JM} + \hat{T}^{\rm mag\,5}_{JM} = \int d^3x\; j_J(kx)\, \vec{Y}^M_{JJ1}(\Omega_x) \cdot \hat{\boldsymbol{\mathcal{J}}}(\boldsymbol{x}) \; . \tag{2.3.24}$$

These correspond to the Coulomb, longitudinal, transverse electric, and transverse magnetic multipole operators, respectively. Each operator contains both vector and axial-vector components, reflecting the V-A structure of the weak interaction as established in Section 2.2.3 as defined by

$$\hat{\mathcal{J}}_\mu = \hat{J}_\mu + \hat{J}_{\mu 5} \; . \tag{2.3.25}$$

By combining Eqs. (2.3.19) and (2.3.20) with the previously defined multipole operators, the Hamiltonian matrix element for semileptonic processes is expressed as

$$\begin{aligned}\langle f|\hat{H}_{\rm W}|i\rangle = -\frac{G_{\rm F}}{\sqrt{2}}\langle f| \Bigg\{ &-\sum_{J\geq 1}\sqrt{2\pi(2J+1)}(-i)^J \sum_{\lambda=\pm} l_\lambda \big[\lambda \hat{\mathcal{T}}^{\rm mag}_{J\,-\lambda}(k) + \hat{\mathcal{T}}^{\rm el}_{J\,-\lambda}(k)\big] \\ &+ \sum_{J=0}\sqrt{4\pi(2J+1)}(-i)^J \big[l_3 \hat{\mathcal{L}}_{J0}(k) - l_0 \hat{\mathcal{M}}_{J0}(k)\big] \Bigg\} \mid i\rangle \; ,\end{aligned} \tag{2.3.26}$$

$\hat{\mathcal{M}}$, $\hat{\mathcal{L}}$, $\hat{\mathcal{T}}^{\rm el}$, and $\hat{\mathcal{T}}^{\rm mag}$ are spherical tensor operators [64] encoding the multipole structure of the nuclear current, allowing the transition amplitude to be decomposed into contributions of definite angular momentum transfer.

2.3.4 Matrix element squared for semileptonic process

Since the nucleus is heavy and can be localized, it undergoes transitions between states of definite angular momentum J_i and J_f. The matrix elements of the tensor operators are evaluated via the Wigner–Eckart theorem [63, 64],

$$\langle J_f\; M_f\; |\hat{\mathcal{T}}_{JM}|\; J_i\; M_i\; \rangle = (-1)^{J_f - M_f} \begin{pmatrix} J_f & J & J_i \\ -M_f & M & M_i \end{pmatrix} \langle J_f||\hat{\mathcal{T}}_J||J_i\rangle \; . \tag{2.3.27}$$

Here the $3j$-symbols encode the dependence on the magnetic quantum numbers M_i, M_f, and M, while all nuclear structure information is contained in the reduced matrix element $\langle J_f||\hat{\mathcal{T}}_J||J_i\rangle$. Applying this theorem to Eq. (2.3.26), the Hamiltonian matrix element takes the form:

$$\begin{aligned}\langle f|\hat{H}_{\rm W}|i\rangle = \frac{G}{\sqrt{2}} \Bigg\{ &\sum_{\lambda=\pm 1} l_\lambda \sum_{J\geq 1} \sqrt{2\pi(2J+1)}\,(-i)^J \Bigg[(-1)^{J_F - M_f} \begin{pmatrix} J_f & J & J_i \\ -M_f & M & M_i \end{pmatrix} \langle J_f||\lambda \hat{\mathcal{T}}^{\rm mag}_J + \hat{\mathcal{T}}^{\rm el}_J||J_i\rangle \Bigg] \\ &- \sum_{J=0}\sqrt{4\pi(2J+1)}(-i)^J \Bigg[l_3 (-1)^{J_f - M_f} \begin{pmatrix} J_f & J & J_i \\ -M_f & 0 & M_i \end{pmatrix} \langle J_f||\hat{\mathcal{L}}_J||J_i\rangle \\ &- l_0 (-1)^{J_f - M_f} \begin{pmatrix} J_f & J & J_i \\ -M_f & 0 & M_i \end{pmatrix} \langle J_f||\hat{\mathcal{M}}_J||J_i\rangle \Bigg] \Bigg\} \; .\end{aligned} \tag{2.3.28}$$

The reaction rates $\Gamma_{i\to f}$ between initial $|i\rangle$ and final $|f\rangle$ discrete nuclear states in semileptonic processes are typically expressed in terms of matrix elements of an effective Hamiltonian

$$\Gamma_{i\to f} \sim |\langle f|\hat{H}_{\rm W}|i\rangle|^2 \; . \tag{2.3.29}$$

To compute the squared matrix element, Eq. (2.3.28) yields the following expression:

$$\begin{aligned}\frac{1}{2J_i+1}\sum_{M_i}\sum_{M_f}|\langle f|\hat{H}_{\rm W}|i\rangle|^2 = \frac{G_{\rm F}^2}{2}\frac{1}{2J_i+1}\\ \left\{\sum_{\lambda=\pm1}\sum_{J\geq1} l_\lambda l_\lambda^* \times (2\pi)|\langle J_f||\lambda\hat{\mathcal{T}}^{\rm mag}_J + \hat{\mathcal{T}}^{\rm el}_J||J_i\rangle|^2\right.\\ +\sum_{J\geq0}(4\pi)\Big[l_3l_3^*\ |\langle J_f||\hat{\mathcal{L}}_J||J_i\rangle|^2 + l_0l_0^*\ |\langle J_f||\hat{\mathcal{M}}_J||J_i\rangle|^2\\ \left.-2{\rm Re}\left(l_3l_0^*\langle J_f||\hat{\mathcal{L}}_J||J_i\rangle\ \langle J_f||\hat{\mathcal{M}}_J||J_i\rangle^*\right)\Big]\right\}.\end{aligned} \tag{2.3.30}$$

It is important to note that the cross terms involving products of components of $\boldsymbol{l}$ vanish due to their orthogonality. Additionally, the $\delta_{M,M'}$ factor ensures that the product of transverse tensors with the Coulomb tensor is zero. There is also no interference between the transverse and longitudinal or charge density terms, as the transverse contribution corresponds to $M = \lambda = \pm1$, whereas the others have $M = 0$.

Furthermore, this result can be simplified using the notation introduced in [31]:

$$\begin{aligned}\sum_{\lambda=\pm1}|l_\lambda^*|^2\,|a+\lambda b|^2 &= |a+b|^2\frac{1}{2}\left(l_1l_1^*+l_2l_2^*+il_2l_1^*-il_1l_2^*\right)\\ &\quad+|a-b|^2\frac{1}{2}\left(l_1l_1^*+l_2l_2^*-il_2l_1^*+il_1l_2^*\right)\\ &= \left(|a|^2+|b|^2\right)(\mathbf{l}\cdot\mathbf{l}^*-l_3l_3^*) - i(\mathbf{l}\times\mathbf{l}^*)_3\,2\,{\rm Re}(ab^*)\ .\end{aligned} \tag{2.3.31}$$

Therefore, Eq. (2.3.30) can be written as [26, 31]:

$$\frac{1}{2J+1}\sum_{M_iM_f}\sum_{\lambda}\left|\langle f\,|\,\hat{H}_{\rm W}\,|\,i\rangle\right|^2 = \frac{G^2}{2}\frac{4\pi}{2J+1} \tag{2.3.32}$$

$$\begin{aligned}&\times\left\{\sum_{J\geq1}\left[\frac{1}{2}\left(l_1l_1^*+l_2l_2^*\right)\right]\left|\langle J_f\|\hat{\mathcal{T}}^{\rm mag}_J\|J_i\rangle\right|^2+\left|\langle J_f\|\hat{\mathcal{T}}^{\rm el}_J\|J_i\rangle\right|^2\right.\\ &\quad-\frac{i}{2}\left(\vec{l}\times\vec{l}^*\right)_3\,2\,{\rm Re}\left(\langle J_f\|\hat{\mathcal{T}}^{\rm mag}_J\|J_i\rangle\langle J_f\|\hat{\mathcal{T}}^{\rm el}_J\|J_i\rangle^*\right)\\ &\quad+\sum_{J=0}\left[l_3l_3^*\left|\langle J_f\|\hat{\mathcal{L}}_J\|J_i\rangle\right|^2+l_0l_0^*\left|\langle J_f\|\hat{\mathcal{M}}_J\|J_i\rangle\right|^2\right]\\ &\quad\left.-2\,l_3l_0^*\langle J_f\|\hat{\mathcal{M}}_J\|J_i\rangle\langle J_f\|\hat{\mathcal{L}}_J\|J_i\rangle^*\right\}.\end{aligned} \tag{2.3.33}$$

Equation (2.3.33) constitutes the central result of this chapter: a general expression for the squared matrix element of any semileptonic multipole process. Resting on two assumptions alone : the existence of a local weak nuclear current operator, and the identification of the initial and final nuclear states as eigenstates of angular momentum.

Chapter 3

Nuclear Structure and Neutrino Sources for CEνNS

This chapter presents the fundamental components necessary for describing CEνNS, with a focus on axial contributions. The nuclear structure framework is introduced, including the model for nucleon states and the decomposition of nuclear currents into irreducible tensor operators in a harmonic oscillator basis. The principal neutrino production mechanisms relevant to CEνNS experiments, such as pion decay-at-rest sources and nuclear reactors, are analyzed in terms of their impact on neutrino energy spectra and fluxes. The chapter concludes by explicitly summarizing the introduction of the CEνNS process and the presentation of the differential cross section as formulated by Hoferichter, Menéndez, and Schwenk [28], highlighting their roles as the foundation for the subsequent results and discussion.

3.1 Nuclear structure

3.1.1 Shell Model

The present analysis of nuclear structure employs the Nuclear Shell Model, proposed in 1949 by Mayer and Jensen [66], who explained the origin of the shell structure in nuclei and its connection with the so-called magic numbers; discontinuities observed in the binding energy and stability limits of nuclei. This model provides a robust single-particle description of nuclear states, essential for the evaluation of the nuclear form factors.

The nuclear interaction demonstrates isospin symmetry, indicating that the strong force does not differentiate between protons and neutrons. As a result, nuclear forces tend to favor configurations with equal numbers of protons and neutrons. However, the repulsive Coulomb interaction necessitates an increasing neutron excess to preserve nuclear stability. For two isotopes of even-Z elements, ${}_{Z}X_{N}$ and ${}_{Z+2}X'_{N'}$, it is generally expected that $N' > N$. Mayer and Jensen identified notable exceptions in which the heaviest isotopes of even-Z elements possess the same neutron number despite an increase in proton number Mayer and Jensen [66]:

$$\begin{aligned}
&\text{Xenon and Barium :} \ {}^{136}\text{Xe} \ , \ {}^{138}\text{Ba} \quad (N = 82),\\
&\text{Krypton and Strontium :} \ {}^{86}\text{Kr} \ , \ {}^{88}\text{Sr} \quad (N = 50),\\
&\text{Calcium and Titanium} \ : \ {}^{48}\text{Ca} \ , \ {}^{50}\text{Ti} \quad (N = 28).
\end{aligned}$$

A similar situation is observed for the lightest isotopes that differ only by the addition

of two protons. These include the lightest isotopes of:

$$\begin{aligned} \text{Neodymium and Samarium : } & {}^{142}\text{Nd},\ {}^{144}\text{Sm} \qquad (N = 82), \\ \text{Zireonium and Molybdenum: } & {}^{90}\text{Zr},\ {}^{92}\text{Mo} \qquad (N = 50). \end{aligned}$$

The stability limits for both heavy and light isotopes display a pronounced increase at $N = 28, 50, 82$ in the nuclear stability diagram. This observation indicates that these neutron numbers are energetically exceptional, independent of the corresponding proton number, and provides strong empirical evidence for the existence of shell closures.

The masses of lighter nuclei were sufficiently well established to enable a detailed study of binding energy patterns, which revealed discontinuities at proton or neutron numbers $2, 8, 20$, corresponding to the closed-shell nuclei ${}^{4}_{2}\text{He}$, ${}^{16}_{8}\text{O}$, and ${}^{40}_{20}\text{Ca}$ [66]. While the binding energy of the $(N+1)^{\text{st}}$ neutron typically increases with atomic weight, a pronounced decrease occurs at the magic numbers. This decrease indicates that the added nucleon is less tightly bound, providing direct evidence that the previous shell is closed and a new shell must be initiated.

Discontinuities in nuclear stability observed at specific neutron numbers, along with similar discontinuities in binding energy in lighter elements, indicate significant energy gaps between single-particle levels. This pattern implies that, once a neutron shell is filled, any additional neutron must occupy a higher energy state. A nuclear shell is defined as a group of energy levels separated from others by wide energy gaps [66]. Furthermore, the independence of magic numbers from the proton count demonstrates that nucleons within the nucleus retain a degree of individuality and can be approximated as particles moving in a mean-field potential that represents the nuclear force.

In this model, each nucleon is considered to move within an average field of force $V(r)$ that exhibits spherical symmetry and does not depend on the instantaneous positions of other nucleons. This central mean-field potential characterizes spherical nuclei. The nuclear potential must generate substantial energy gaps to explain shell closures at the magic numbers, subject to two conditions [66]

- $V(r)$ represents the influence of the other nucleons, which are assumed to be uniformly distributed throughout the nuclear volume. The nucleon density at r=0 is approximately equal to that at any other point within the nucleus. Because $V(r)$ is a spherically symmetrical potential, it must satisfy the following more restrictive condition:
$$\left(\frac{dV}{dr}\right)_{r=0} = 0 \ . \tag{3.1.1}$$
- The potential must go to zero rather abruptly at the nuclear surface that is when r approaches the nuclear radius R.

Both conditions are satisfied by a potential of the form given above,

$$V(r) = \begin{cases} -V_0\left[1 - \left(\frac{r}{R}\right)^2\right] & \text{for } r < R \ , \\ 0 & \text{for } r < R \ , \end{cases} \tag{3.1.2}$$

which inside the nucleus reduces to the harmonic oscillator potential $V(r) = -V_0 + \frac{1}{2}m\omega^2 r^2$.

Because the potential depends solely on r, the Schrödinger equation is separable, and its solutions are given by (see Appendix K):

$$\psi_{nlm} = R_{nl} Y_{lm}(\Omega) \ . \tag{3.1.3}$$

Discrete energy levels are determined by the following expression [67, 68]:

$$\begin{aligned} E_{nl} &= \left(2n_r + l + \frac{3}{2}\right)\hbar\omega \\ &= \left(N + \frac{3}{2}\right)\hbar\omega \ , \end{aligned} \tag{3.1.4}$$

Here, the eigenvalues and eigenfunctions depend on two quantum numbers: the radial quantum number n_r and the orbital quantum number l, where N denotes the energy level. Consequently, the following relation holds:

$$l = N - 2n_r \ .$$

Given $n_r = 0, 1, 2, 3...$, the possible values of l are $N, N-2, N-4, ..., 0$ or 1 .

For the oscillator potential, degeneracy occurs because states with different values of l can share the same principal quantum number N, resulting in identical energy levels. For a fixed l, there are $2l+1$ possible states. Taking into account the two possible spin projections $m_s = \pm 1/2$ for nucleons, the total number of protons or neutrons with a given value of N is:

$$\mathcal{N}_N = \sum_l 2(2l+1) \ , \tag{3.1.5}$$

where l runs over all values allowed by Eq. (3.1.1). Energy levels are denoted by (n_r, l), according to spectroscopic notation: $s, p, d, f, g, h, \ldots$ for $l = 0, 1, 2, 3, 4, 5, \ldots$. The orbital occupancies, computed with $\hat{n} = n_r + 1$ according nuclear notation [64], are summarized in Table 3.1.

N	Energy	Orbitals ($\hat{n}$,l)	$\mathcal{N}_N$	$\sum_N \mathcal{N}_N$
0	3/2	$1s$	2	2
1	5/2	$1p$	6	8
2	7/2	$1d, 2s$	12	20
3	9/2	$1f, 2p$	20	40
4	11/2	$1g, 2d, 3s$	30	70

Table 3.1: Allowed values of the orbital angular momentum quantum number l for a given principal quantum number N in the three-dimensional harmonic oscillator, defined by the relation $N = 2n_r + l$, where n_r is the radial quantum number and use the shell notation ($\hat{n}$,l) with $\hat{n} = n_r + 1$. The table presents the corresponding orbitals $(\hat{n}, l)$, the degeneracy $\mathcal{N}_N$ at each shell, and the cumulative sum $\sum_N \mathcal{N}_N$ [67].

A central potential modeled solely as a harmonic oscillator does not account for all experimentally observed magic numbers. As indicated in Table 3.1, only those corresponding to the first three shells are reproduced. To address this, Goeppert-Mayer and Jensen introduced a spin-orbit potential of the form $v_{LS}(r)\ \boldsymbol{L}\cdot\boldsymbol{S}$ [66, 64]. With this

modification, the shell model describes the nucleon as follows [64]:

$$H(\boldsymbol{x})\phi_\alpha(\boldsymbol{x}) = \varepsilon_\alpha\phi_\alpha(\boldsymbol{x}) \quad \text{with} \quad H(\boldsymbol{x}) = \frac{p^2}{2m} + \frac{1}{2}m\omega^2 r^2 + V_{so}(r)\ \boldsymbol{L}\cdot\boldsymbol{S}\ . \tag{3.1.6}$$

Here α denotes the complete set of quantum numbers characterizing the single-particle state and $\phi_\alpha(\boldsymbol{x})$ the corresponding eigenfunction. In the angular momentum coupling formalism [63], two angular momenta $\boldsymbol{L}$ and $\boldsymbol{S}$ couple to a total $\boldsymbol{J} = \boldsymbol{L} + \boldsymbol{S}$, yielding the coupled basis $|l\, s\, j\, m\rangle$. The spin-orbit operator is evaluated using $\boldsymbol{L}\cdot\boldsymbol{S} = \frac{1}{2}(J^2 - L^2 - S^2)$, giving:

$$L\cdot S\,|l,s,j,m\rangle = \frac{\hbar^2}{2}\left\{j(j+1) - l(l+1) - s(s+1)\right\}|l,s,j,m\rangle\ . \tag{3.1.7}$$

In conclusion, the single-particle eigenstates of the shell model are elements of the coupled basis of the harmonic oscillator, with nucleon spin $s = \frac{1}{2}$ included. Each single-particle state is characterized by the conserved quantum numbers (n, l, j, m) and takes the form:

$$|\phi_\alpha\rangle \equiv |n\left(l\frac{1}{2}\right)jm\rangle\ . \tag{3.1.8}$$

The coordinate representation of the state vector is given by [64]:

$$\langle x \mid \alpha\rangle = \phi_\alpha(x) = R_{n_\alpha l_\alpha}(r)\,[Y_{l_\alpha m_{l_\alpha}}(\Omega)\,\chi_{\frac{1}{2}}]_{j_\alpha m_\alpha}\ , \qquad \Omega = (\theta,\phi)\ , \tag{3.1.9}$$

where $R_{nl}(r)$ is the harmonic oscillator radial function and $[Y_{lm_l}(\Omega)\,\chi_{\frac{1}{2}}]_{jm}$ is the tensor product of the spherical harmonic and the nucleon spinor, coupling orbital and spin angular momenta to definite j.

The addition of the spin-orbit term $\boldsymbol{L}\cdot\boldsymbol{S}$ to the shell model Hamiltonian breaks the degeneracy of each orbital l, splitting it into two levels characterized by $j = l + \frac{1}{2}$ and $j = l - \frac{1}{2}$. The associated eigenvalues, as derived from Eq. (3.1.7), are [69]:

$$L\cdot S\,|n,l,s,j,m\rangle = \frac{\hbar^2}{2}\left\{j(j+1) - l(l+1) - \frac{3}{4}\right\}\left|n,l,\frac{1}{2},j,m\right\rangle \tag{3.1.10}$$

$$= \begin{cases} \frac{1}{2}l & \text{for } j = l + \frac{1}{2}\ , \\ -\frac{1}{2}(l+1) & \text{for } j = l - \frac{1}{2}\ , \end{cases} \tag{3.1.11}$$

As the splitting increases with l, orbitals with large l exhibit significant energy gaps between the two j states. This mechanism produces new shell closures that correspond exactly to the empirically observed magic numbers, thereby defining the nuclear shell structure. The resulting level scheme is shown in Figure 3.1.

3.1.2 Harmonic Oscillator single-particle matrix elements

Following the establishment of the nuclear shell model in the previous section, the single-particle basis is employed to evaluate the matrix elements of the multipole operators present in the semileptonic Hamiltonian Eq. (2.3.33). The harmonic oscillator basis is especially suitable for this purpose, as it is widely utilized in many-body nuclear calculations and enables the analytical determination of matrix elements in terms of finite polynomials.

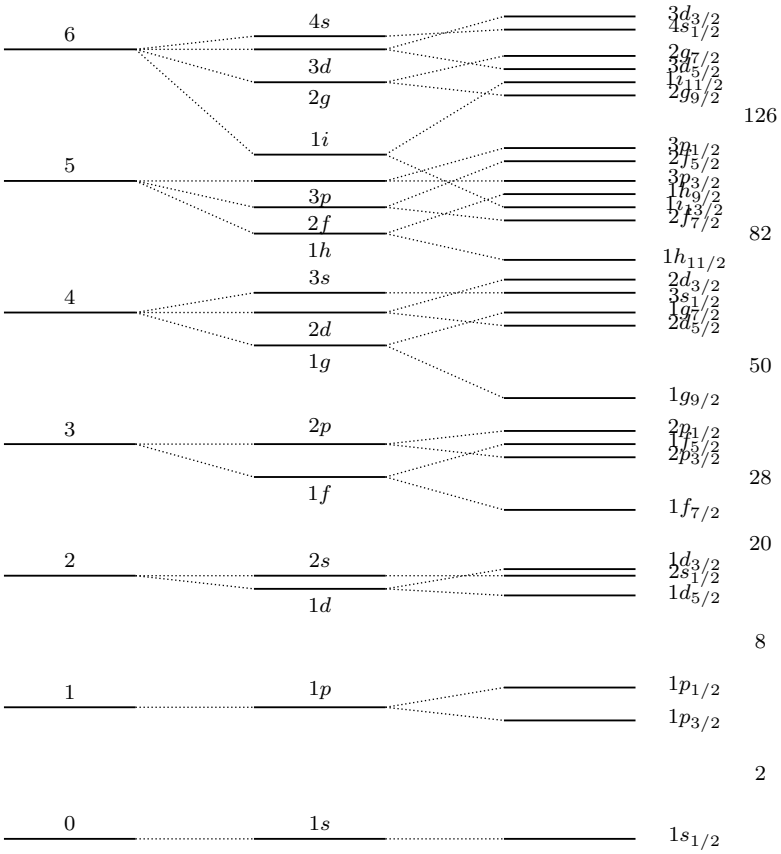

Figure 3.1: Single-particle level ordering scheme for the nuclear shell model. The diagram presents energy levels arising from the harmonic oscillator potential (left) and the inclusion of a spin-orbit coupling term $\ell \cdot s$ (center), as well as the resulting states labeled by single-particle $n\ell_j$ (right). The numbers on the far right indicate the cumulative nucleon occupation at each shell closure, thereby illustrating the magic numbers [31, 67].

Multipole operators

A prescription for the nuclear weak current is required [70]. The matrix elements of the current between nucleon states are considered, employing Lorentz invariance, parity invariance, and isospin invariance. Representing the nucleon as a Dirac spinor enables the general form of these matrix elements to be expressed [71]. The derivation of these currents is provided in Appendix L:

$$\langle p'\lambda'; \tfrac{1}{2}m_t'|J_{\mu\ JM_J}|p\lambda; \tfrac{1}{2}m_t\rangle = i\,\bar{u}(p',\lambda')\left[F_1^{(J)}\gamma_\mu + F_2^{(J)}\sigma_{\mu\nu}q^\nu\right]u(p,\lambda) \times \left\langle \tfrac{1}{2}m_t' \left| I^1_{JM_J} \right| \tfrac{1}{2}m_t \right\rangle, \tag{3.1.12}$$

$$\langle p'\lambda'; \tfrac{1}{2}m_t'|J^5_{\mu\ JM_J}|p\lambda; \tfrac{1}{2}m_t\rangle = i\,\bar{u}(p',\lambda')\left[F_A^{(J)}\gamma_5\gamma_\mu - iF_P^{(J)}\gamma_5 q_\mu\right]u(p,\lambda) \times \left\langle \tfrac{1}{2}m_t' \left| I^1_{JM_J} \right| \tfrac{1}{2}m_t \right\rangle. \tag{3.1.13}$$

Here, the plane-wave single-nucleon states are characterized by three-momentum $\boldsymbol{p}$ ($\boldsymbol{p'}$), helicities λ (λ'), and isospin quantum numbers.

In addition, we adopt the conserved vector current hypothesis, which implies the absence of induced scalar (second-class vector) currents and we assume that there are no induced tensor (second-class axial-vector) currents. The single-nucleon form factors

$F_X^{(J)}(q^2)$, where $J = 0, 1$ and $X = 1, 2, A, P$ (representing vector (Dirac), vector (Pauli), axial, and pseudoscalar, respectively), are all functions of q^2 [71]. The isospin dependence in Eqs. (3.1.13) and (3.1.12) is incorporated through the isospin operator $I_T^{M_T}$ [72]. Wigner-Eckart theorem in isospin space yields immediately [72]

$$\langle \tfrac{1}{2} m_t' \,|\, I_T^{M_T} \,|\, \tfrac{1}{2} m_t \rangle = (-1)^{\frac{1}{2} - m_t'} \begin{pmatrix} \frac{1}{2} & T & \frac{1}{2} \\ -m_t' & M_T & m_t \end{pmatrix} \langle \tfrac{1}{2} \| I_T \| \tfrac{1}{2} \rangle \ ,$$

$$\text{with} \quad \langle \tfrac{1}{2} \| I_T \| \tfrac{1}{2} \rangle = \sqrt{[T]} = \sqrt{2T+1} \ . \tag{3.1.14}$$

The relevant $\boldsymbol{q}^2$ region is determined by the nuclear form factors, and within the target, nucleons can be treated nonrelativistically. The nonrelativistic reduction yields operators such as ∇ and σ [71]. By substituting the current expressions from Eqs. (3.1.13) and (3.1.12) into the multipole operators defined in Eqs. (2.3.21), (2.3.22), (2.3.23), and (2.3.24), the expressions for the multipole tensors are obtained (a detailed derivation is provided in Ref. [26]):

$$M_{JM_J;TM_T}(qx) = F_1^{(T)} \, M_J^{M_J}(qx) \, I_T^{M_T} \ , \tag{3.1.15.a}$$

$$T^{el}_{JM_J;TM_T}(qx) = \frac{q}{M_N} \left[F_1^{(T)} \, \Delta_J^{M_J}(qx) + \frac{1}{2} \mu^{(T)} \, \Sigma_J^{M_J}(qx) \right] I_T^{M_T} \ , \tag{3.1.15.b}$$

$$iT^{mag}_{JM_J;TM_T}(qx) = -\frac{q}{M_N} \left[F_1^{(T)} \, \Delta_J^{M_J}(qx) - \frac{1}{2} \mu^{(T)} \, \Sigma'^{M_J}_J(qx) \right] I_T^{M_T} \ , \tag{3.1.15.c}$$

$$iM^5_{JM_J;TM_T}(qx) = \frac{q}{M_N} \left[F_A^{(T)} \, \Omega_J^{M_J}(qx) + \frac{1}{2} q_0 F_P^{(T)} \, \Sigma''^{M_J}_J(qx) \right] I_T^{M_T} \ , \tag{3.1.15.d}$$

$$-iL^5_{JM_J;TM_T}(qx) = \left[F_A^{(T)} - \frac{q^2}{2M_N} F_P^{(T)} \right] \Sigma''^{M_J}_J(qx) \, I_T^{M_T} \ , \tag{3.1.15.e}$$

$$-iT^{el5}_{JM_J;TM_T}(qx) = F_A^{(T)} \, \Sigma'^{M_J}_J(qx) \, I_T^{M_T} \ , \tag{3.1.15.f}$$

$$T^{mag5}_{JM_J;TM_T}(qx) = F_A^{(T)} \, \Sigma_J^{M_J}(qx) \, I_T^{M_T} \ , \tag{3.1.15.g}$$

where M_N is the nucleon mass and $\mu^{(1)}(q_\mu^2) = F_1^{(1)}(q_\mu^2) + 2M_N F_2^{(1)}(q_\mu^2)$. These operators are described in terms of the seven basic multipole operators:

$$\xi = 1, \quad M_J^{M_J}(qx), \tag{3.1.16.a}$$

$$\xi = 2, \quad \Delta_J^{M_J}(qx) \equiv M_J^{M_J}(qx) \left(\frac{1}{q} \nabla \right), \tag{3.1.16.b}$$

$$\xi = 3, \quad \Delta'^{M_J}_J(qx) \equiv -i \left[\frac{1}{q} \nabla \times M_J^{M_J}(qx) \right] \cdot \frac{1}{q} \nabla \tag{3.1.16.c}$$

$$= [J]^{-1} \left[-\sqrt{J} \, M^{M_J}_{J,J+1}(qx) + \sqrt{J+1} \, M^{M_J}_{J,J-1}(qx) \right] \cdot \frac{1}{q} \nabla, \tag{3.1.16.d}$$

$$\xi = 4, \quad \Sigma_J^{M_J}(qx) \equiv M_J^{M_J}(qx) \cdot \sigma, \tag{3.1.16.e}$$

$$\xi = 5, \quad \Sigma'^{M_J}_J(qx) \equiv -i \left[\frac{1}{q} \nabla \times M_J^{M_J}(qx) \right] \cdot \sigma \tag{3.1.16.f}$$

$$= [J]^{-1} \left[-\sqrt{J} \, M^{M_J}_{J,J+1}(qx) + \sqrt{J+1} \, M^{M_J}_{J,J-1}(qx) \right] \cdot \sigma, \tag{3.1.16.g}$$

$$\xi = 6, \quad \Sigma''^{M_J}_J(qx) \equiv \left[\frac{1}{q}\nabla M^{M_J}_J(qx)\right]\cdot\sigma \tag{3.1.16.h}$$

$$= [J]^{-1}\left[\sqrt{J+1}\, M^{M_J}_{J,J+1}(qx) + \sqrt{J}\, M^{M_J}_{J,J-1}(qx)\right]\cdot\sigma, \tag{3.1.16.i}$$

$$\xi = 7, \quad \Omega^{M_J}_J(qx) \equiv M^{M_J}_J(qx)\,\sigma\cdot\left(\frac{1}{q}\nabla\right)\ , \tag{3.1.16.j}$$

defined within the Walecka-Donelly method [27, 72, 71] as nuclear responses, in which these operators are independent of the form factors and

$$\begin{aligned} M^{MJ}_J(q\boldsymbol{x}) &= j_J(qx)Y^{M_J}_J(\Omega)\ , \\ \mathbf{M}^J_M(q\boldsymbol{x}) &= j_J(qx)\mathbf{Y}^M_{JL1}(\Omega)\ . \end{aligned} \tag{3.1.17}$$

The Single-particle matrix elements

The shell-model single-particle basis $|n_a(l\tfrac{1}{2})j_a m_a\rangle$ is employed within the harmonic oscillator potential, as described in Eq. (3.1.9). By applying the Wigner-Eckart theorem (Eq. (2.3.27)) and the angular momentum recoupling relations of Edmonds [63], the reduced matrix elements are derived analytically. Explicit expressions are available in Refs. [72, 71, 73]:

$$\langle n'l'j'||M_J(qx)||nlj\rangle = \frac{1}{\sqrt{4\pi}}(-)^{J+j+1/2}[l'][l][j'][j][J]\begin{Bmatrix} l' & j' & \frac{1}{2} \\ j & l & J\end{Bmatrix}\begin{pmatrix} l' & J & l \\ 0 & 0 & 0\end{pmatrix}\langle n'l'j'|j_J(\rho)|nlj\rangle\ , \tag{3.1.18.a}$$

$$\langle n'l'j'||\boldsymbol{M}_{JL}(q\boldsymbol{x})\cdot\boldsymbol{\sigma}||nlj\rangle = \sqrt{\frac{3}{2\pi}}(-)^{l'}[l'][l][j'][j][L][J]\begin{Bmatrix} l' & l & L \\ \frac{1}{2} & \frac{1}{2} & 1 \\ j' & j & J\end{Bmatrix}$$

$$\begin{pmatrix} l' & L & l \\ 0 & 0 & 0\end{pmatrix}\langle n'l'j'|j_L(\rho)|nlj\rangle\ , \tag{3.1.18.b}$$

$$\langle n'l'j'||\boldsymbol{M}_L(q\boldsymbol{x})\cdot\frac{1}{q}\boldsymbol{\nabla}||nlj\rangle = \frac{1}{\sqrt{4\pi}}(-)^{L+j+1/2}[l'][j'][j][L][J]\begin{Bmatrix} l' & j' & \frac{1}{2} \\ j & l & J\end{Bmatrix}$$

$$\times\left\{-(l+1)^{1/2}[l+1]\begin{Bmatrix} L & 1 & J \\ l & l' & l+1\end{Bmatrix}\begin{pmatrix} l' & L & l+1 \\ 0 & 0 & 0\end{pmatrix}\langle n'l'j'|j_L(\rho)\left(\frac{d}{d\rho}-\frac{l}{\rho}\right)|nlj\rangle\right.$$

$$\left.+\, l^{1/2}[l-1]\begin{Bmatrix} L & 1 & J \\ l & l' & l-1\end{Bmatrix}\begin{pmatrix} l' & L & l-1 \\ 0 & 0 & 0\end{pmatrix}\langle n'l'j'|j_L(\rho)\left(\frac{d}{d\rho}+\frac{l+1}{\rho}\right)|nlj\rangle\right\}\ , \tag{3.1.18.c}$$

$$\langle n'l'j'||M_J(q\boldsymbol{x})\boldsymbol{\sigma}\cdot\frac{1}{q}\boldsymbol{\nabla}||nlj\rangle = \frac{1}{\sqrt{4\pi}}(-)^{l'}[l'][j'][j][2j-l][J]\begin{Bmatrix} l' & j' & \frac{1}{2} \\ j & 2j-l & J\end{Bmatrix}\begin{pmatrix} l' & J & 2j-l \\ 0 & 0 & 0\end{pmatrix}$$

$$\times\left\{-\delta_{j,l+1/2}\langle n'l'j'|j_J(\rho)\left(\frac{d}{d\rho}-\frac{l}{\rho}\right)|nlj\rangle + \delta_{j,l-1/2}\langle n'l'j'|j_J(\rho)\left(\frac{d}{d\rho}+\frac{l+1}{\rho}\right)|nlj\rangle\right\}\ . \tag{3.1.18.d}$$

For multipole operators in Eq. (3.1.16) with $\rho = qx$, the angular components are determined using recoupling relations and the $3-j$ and $6-j$ symbols, while radial matrices are defined by [72, 70]

$$\langle n'l'j'|\theta(\rho)|nlj\rangle = \int x^2 dx\, R^*_{n'l'j'}(x)\,\theta(\rho)\,R_{nlj}(x)\ . \tag{3.1.19}$$

$$\text{with} \quad \theta(\rho) = \begin{cases} j_J(\rho)\ , \\ j_J(\rho)\left(\dfrac{d}{d\rho} - \dfrac{l}{\rho}\right)\ , \\ j_J(\rho)\left(\dfrac{d}{d\rho} + \dfrac{l+1}{\rho}\right)\ . \end{cases}$$

The radial matrix elements in Eq. (3.1.19) are evaluated using harmonic oscillator wave functions, the natural choice since the shell model is formulated within this potential and the radial functions are known analytically (Appendix K). Following Refs. [26, 72, 71], the radial solution is:

$$R_{nl} = \left[\frac{2e^z}{b^3(n-1)!\Gamma(n+l+\frac{1}{2})z^{l+1}}\right]^{\frac{1}{2}} \frac{d^{n-1}}{dz^{n-1}}\left\{z^{n+l-\frac{1}{2}}e^{-z}\right\}\ , \tag{3.1.20}$$

where $z = (x/b)^2$ and b is the oscillator length parameter. Substituting into the radial integrals (Appendix M), the results take the form of exponential and hypergeometric functions, reducing the single-particle matrix elements to the closed-form expression:

$$\langle n'l'j'|T_J(qx)|nlj\rangle = \frac{1}{\sqrt{4\pi}} y^{(J-K)/2} e^{-y} p(y)\ . \tag{3.1.21}$$

3.2 Neutrino production

3.2.1 Neutrinos at the Spallation Neutron Source

The first mechanism under consideration is neutrino production via spallation. In physics, spallation refers to a high-energy nuclear reaction in which a target nucleus, when impacted by an energetic incident particle, emits multiple lighter particles and is transformed into a residual nucleus of lower mass [74]. Spallation neutron sources generate neutrons by accelerating protons with a high-powered accelerator and directing them onto a heavy metal target, such as mercury or tungsten. This process leads to the emission of free neutrons as a result of the impact [75].

The SNS at ORNL, specifically its First Target Station (FTS), is one of the most powerful neutron sources in the world and provides, as a by-product, a high-flux stopped-pion neutrino source [76]. At the FTS, H^- ions are accelerated to 1 GeV by a superconducting linac and stripped to protons via a diamond foil before accumulation in the Proton Accumulator Ring. The resulting 1 GeV proton pulses, delivered at 60 Hz and 1.4 MW with 10^{16} POT/s, bombard a steel vessel containing 20 tons of liquid mercury; each high-energy proton striking a mercury nucleus releases 20–30 spalled neutrons, which are guided into beam tubes attached to the instrument stations [21, 75].

As a by-product of the spallation, charged and neutral pions are also produced. About 99% of π^- are captured by nuclei, while π^+ particles come to rest and subsequently decay.

As shown in Figure 3.2, π^+ decay via $\pi^+ \to \mu^+ + \nu_\mu$, resulting in mono-energetic muon neutrinos at 30 MeV. The subsequent three-body muon decay, $\mu^+ \to e^+ + \bar{\nu}_\mu + \nu_e$, produces a continuous spectrum of electron neutrinos and muon antineutrinos with energies up to 52.6 MeV [21].

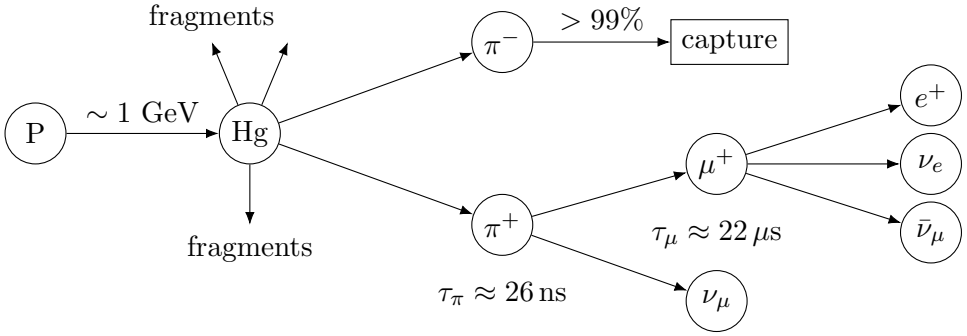

Figure 3.2: Decay chain for neutrino production at the SNS: a proton beam at $\sim$ 1 GeV impacts a mercury (Hg) target, generating π^+ and π^- mesons, whose subsequent decay at rest produces muons and neutrinos. [21].

The Proton Power Upgrade (PPU) will double the current accelerator power, increasing the brightness of pulsed neutron beams and enabling the construction of a Second Target Station (STS). Unlike the FTS, which employs a liquid mercury target in a steel casing with a rectangular cross section of 39.9×10.4 cm^2, the STS design assembles 21 tungsten wedges in a ring of 1.1 m diameter, together with an additional experimental hall, substantially expanding the scientific reach of the SNS [76].

A comparable facility is the ESS, currently under construction in Lund, Sweden. As at the SNS, neutrons at the ESS are produced by spallation, and the facility will soon provide the largest pulsed neutrino flux suitable for CEνNS detection. The ESS accelerator delivers proton pulses at $\sim$ 2 GeV with an average beam power of 5 MW at 14 Hz, directed onto a rotating tungsten target where spallation reactions occur [77, 25]. Notably, the neutrino energy spectrum from spallation sources is largely independent of the proton beam characteristics, making it essentially identical for both the SNS and the ESS.

3.2.2 Neutrinos from nuclear reactors

Nuclear reactors serve as significant sources of neutrinos. In 1956, a nuclear reactor provided the flux required for the first detection of neutrinos via the inverse beta decay process $\nu_- + p^+ \to \beta^+ + n^0$ [78]. In this experiment, the intense antineutrino flux produced by fission-fragment decay was directed onto a detector containing a high density of target protons within a hydrogenous liquid scintillator, enabling the identification of a free neutrino signal.

A nuclear reactor operates through the process of nuclear fission, as illustrated in Figure 3.3. During fission, a neutron collides with a heavy atomic nucleus, which subsequently captures the neutron, becomes unstable, and splits into two smaller nuclei referred to as fission products. This reaction also emits additional neutrons, which can sustain a chain reaction [79]. The fission process within the reactor ultimately generates antineutrino flux via β decays, described by the following form:

$$ {}^{A}_{Z}X \to {}^{A}_{Z+1}Y + e^- + \bar{\nu}_e \ . \tag{3.2.1} $$

This process occurs in the neutron-rich fission fragments of heavy nuclei, primarily uranium and plutonium isotopes [80].

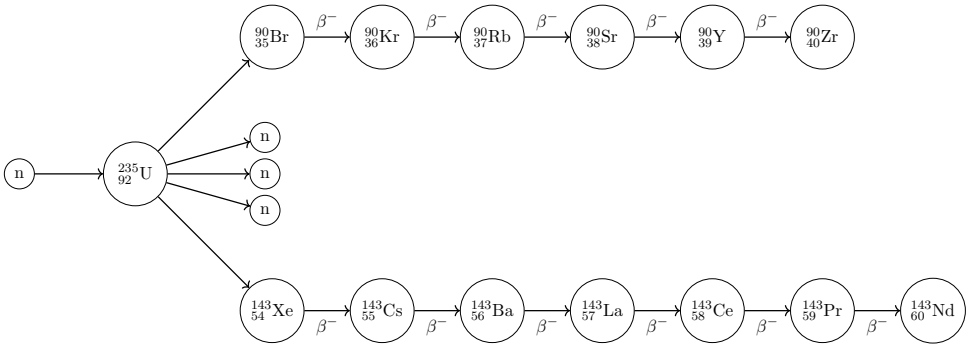

Figure 3.3: Illustration of the nuclear fission of $^{235}_{92}$U and the subsequent β^- decay chains. Electron antineutrinos are produced in these β^- decays. [81]

In commercial nuclear reactors, the primary fission isotopes are ^{235}U, ^{238}U, ^{239}Pu, and ^{241}Pu. Although ^{238}U constitutes approximately 99.3% of natural uranium and does not fission with thermal neutrons, it can do so with fast neutrons; upon neutron absorption it undergoes β^- decay to produce the fissile isotope ^{239}Pu, which in turn can breed ^{241}Pu. The fission of these isotopes generates neutron-rich fragments that are unstable, and the difference in binding energy between the original heavy nucleus and the fission products is released as approximately 200 MeV per event [81].

As a result, these nuclei undergo a series of β^- decays before reaching stable isotopes [81]. Figure 3.3 illustrates these processes. Each β^- decay is accompanied by the emission of an electron and an electron antineutrino, as described by

$$n \to p + e^- + \bar{\nu}_e. \tag{3.2.2}$$

On average, each fission event produces approximately 6 $\bar{\nu}_e$. Neutron capture by ^{238}U nuclei represents another significant source of antineutrino flux. This process occurs via the following reaction: $^{238}\text{U} + n \to^{239}$ U $\to^{239}$ Np $\to^{239}$ Pu. The β decay of ^{239}U results in the production of two $\bar{\nu}_e$ [81, 80].

3.3 Coherent Elastic Neutrino–Nucleus Scattering

This investigation focuses on the process CEνNS, with particular emphasis on its axial contribution, motivated by the emerging precision era. CEνNS was first predicted by Freedman in 1974 [14]. The initial experimental observation occurred in 2017, when the COHERENT collaboration detected CEνNS using CsI detectors at the SNS [16]. More recently, in 2024, the CONUS+ experiment observed CEνNS with reactor neutrinos using high-purity germanium (HPGe) detectors [82]. The detection challenge arises because the only observable is a nuclear recoil in the few-keV range.

This process involves low-energy neutrinos scattering coherently from the entire nucleus through Z^0 exchange, resulting in ground-state-to-ground-state transitions. The coherence condition, $qR_A \lesssim 1$, where $q^2 = 2m_N E_{nr}$ and R_A denotes the nuclear radius, is typically satisfied for reactor, solar, supernova, and artificial neutrino sources, as their momentum transfers remain well below the inverse nuclear size.

3.3.1 Diferential Cross section for CEνNS

The neutrino-nucleus cross section is calculated in the regime of low momentum transfer, where the interaction reduces to an effective four-fermion coupling, as derived in Section 2.3.1. This approximation is valid because the incident neutrino energies are significantly below the Z boson mass. The analysis proceeds by transitioning from the quark level to the nuclear level, utilizing multipole analysis and nuclear form factors to characterize the nucleon distribution within the nucleus.

The initial stage involves the quark-neutrino interaction within the SM framework. Based on the results presented in Section (2.2.5), the effective Lagrangian describing neutrino–quark interactions is derived from Eqs. (2.2.35) and (2.2.39) as follows:

$$\mathcal{L}_{nq}^{\text{eff}} = \frac{G_F}{\sqrt{2}} \sum_{\substack{q=u,d \\ \alpha=e,\mu,\tau}} [\ \bar{\nu}_\alpha\ \gamma^\mu(g_V^\nu - g_A^\nu\ \gamma_5)\nu_\alpha\ ][\ \bar{q}\ \gamma_\mu(g_V^q - g_A^q\ \gamma_5)q\ ]\ . \tag{3.3.1}$$

In this context $g_{V,A}$ denote the Standard Model (SM) vector and axial-vector couplings, which take the following values:

$$\begin{aligned} g_V^\nu &= \frac{1}{2}\ \ ,\ \ g_A^\nu = \frac{1}{2}\ , \\ g_V^{u,c,t} &= \frac{1}{2} - \frac{4}{3}\sin^2\theta_W\ \ ,\ \ g_A^{u,c,t} = \frac{1}{2}\ , \\ g_V^{d,s,b} &= -\frac{1}{2} + \frac{2}{3}\sin^2\theta_W\ \ ,\ \ g_A^{d,s,b} = -\frac{1}{2}\ . \end{aligned} \tag{3.3.2}$$

These couplings describe the interactions between quarks and the Z boson and depend on the weak mixing angle, which has a value of $\sin^2\theta_W(q=0) = 0.23857$ [83].

At the nucleon level, electroweak processes are generally modeled as one-body processes, with additional corrections included as necessary. In this framework, nuclear current operators are represented as the sum of the currents of the constituent nucleons [31]. The most general structure of the matrix element of the current for a free nucleon is provided in Eqs. (3.1.12) and (3.1.13), as described in [31, 28]:

$$\langle \boldsymbol{p}'\sigma'\rho'|\mathcal{J}_\mu|\boldsymbol{p}\sigma\rho\rangle = \bar{u}(\boldsymbol{p}',\sigma')\eta_{\rho'}^\dagger\,[J_\mu - J_{\mu 5}]\,\eta_\rho u(\boldsymbol{p},\sigma)\ . \tag{3.3.3}$$

The matrix elements for J_μ and for $J_{\mu 5}$ are, respectively [28],

$$\langle N(p')|\bar{q}\gamma_\mu q|N(p)\rangle = \bar{u}(p')\eta_{\rho'}^\dagger\left[F_1^{q,N}(t)\gamma_\mu - F_2^{q,N}(t)\frac{i\sigma_{\mu\nu}q^\nu}{2m_N}\right]\eta_\rho u(p)\ , \tag{3.3.4}$$

$$\langle N(p')|\bar{q}\gamma_\mu\gamma_5 q|N(p)\rangle = \bar{u}(p')\eta_{\rho'}^\dagger\left[\gamma_\mu\gamma_5\,G_A^{q,N}(t) - \gamma_5\frac{q_\mu}{2m_N}G_P^{q,N}(t)\right]\eta_\rho u(p)\ . \tag{3.3.5}$$

Here $\bar{u}$, u are Dirac spinors, η_p, η_n Pauli isospinors, $q = p - p'$ the four-momentum transfer, and $F_1(q^2)$, $F_2(q^2)$ form factors encoding the nucleon distribution within the composite nucleus.

To construct the nuclear current density operator, we use the following expression in second quantization [31]:

$$\hat{J}_\mu = \sum_{\boldsymbol{p'}\sigma'\rho'} \sum_{\boldsymbol{p}\sigma\rho} c^\dagger_{\boldsymbol{p'}\sigma'\rho'} \langle \boldsymbol{p'}\sigma'\rho' | J_\mu | \boldsymbol{p}\sigma\rho \rangle c_{\boldsymbol{p}\sigma\rho} \tag{3.3.6}$$

with

$$\langle p'\sigma'\rho' | J_\mu(x) | p\sigma\rho \rangle = \int d^3y \, \phi^*_{p'\sigma'\rho'}(y) \left\{ J_\mu(y) \, \delta^{(3)}(x-y) \right\} \phi_{p\sigma\rho}(y) \ , \tag{3.3.7}$$

where the nuclei current is defined as the sum of the currents of the constituent nucleons. The set $\{\boldsymbol{p}\sigma\rho\}$ denotes a complete basis of momentum, spin, and isospin quantum numbers for each nucleon. The operators c and $c^\dagger$ correspond to the annihilation and creation operators of nucleons in the nuclear Hilbert space.

This approach establishes the final connection with nuclear physics by employing second-quantized transitions for multipole operators within the nuclear many-particle space:

$$\hat{T}_{JM} = \sum_{\alpha\beta} c^\dagger_\alpha \langle \alpha | T_{JM} | \beta \rangle c_\beta \ . \tag{3.3.8}$$

Here, T_{JM} denotes any of the operators in Eqs. (3.1.15), which are constructed from single-nucleon currents. The matrix elements of these operators, evaluated between nuclear many-body states labeled $|J_i \ M_{Ji}; T_i \ M_{Ti}\rangle$, can be expressed in terms of the one-body density matrix [72, 70, 31]:

$$\langle J_f; T_f || \hat{T}_{J,T} || J_i; T_i \rangle = \sum_{|\alpha|,|\beta|} \psi^{f,i}_{JT}(\alpha, \beta) \langle \alpha; \tfrac{1}{2} || T_{J,T} || \beta; \tfrac{1}{2} \rangle \ . \tag{3.3.9}$$

In this expression, $|J_f, T_f\rangle$ and $|J_i, T_i\rangle$ denote the angular momentum and isospin of the operator, as well as those of the final and initial nuclear states, respectively. The state $|\alpha\rangle = \{n_\alpha(l_\alpha \tfrac{1}{2}) j_\alpha\}$ specifies the set of single-nucleon quantum numbers.

The matrix elements are evaluated by assuming a specific model for the initial and final nuclear states. In this analysis, shell model wave functions are employed, utilizing the formalism presented in Section 3.1.2. Within the Donnelly-Walecka multipole decomposition framework, the relevant nuclear matrix element for the dominant coherent channel is determined by the Coulomb operator $\mathcal{M}_0$ [84]:

$$|\langle gs || \hat{\mathcal{M}}_0 || gs \rangle|^2 = [g_V^p Z F_Z(q^2) + g_V^n N F_N(q^2)]^2 \ . \tag{3.3.10}$$

The vector couplings of protons (g_V^p) and neutrons (g_V^n) are normalized according to their valence-quark content, leading to the following relations [12]:

$$g_V^n = g_V^u + 2g_V^d = -\frac{1}{2} \ , \qquad g_V^p = 2g_V^u + g_V^d = \frac{1}{2} - 2\sin^2\theta_W \ . \tag{3.3.11}$$

$F_{Z(N)}$ represent the corresponding nuclear form factors. These form factors are functions of the transferred four-momentum q^2, which is primarily determined by the energy of the incident neutrino.

The momentum transfer determines the spatial resolution of the interaction and the extent to which the neutrino probes nuclear structure. For very small momentum transfer, $q^2 \to 0$, the wavelength associated with the probe exceeds the nuclear size, preventing resolution of the internal nucleon distribution. In this regime, the vector form factors approach unity, $F_V^{n,p}(q^2 \to 0) = 1$, and the nuclear weak form factor is normalized to the coherent sum of the individual nucleon vector couplings [12]

$$F_{\mathrm{W}}(q^2 \to 0) = g_V^n N + g_V^p Z = Q_{\mathrm{W}} \ . \tag{3.3.12}$$

Here N and Z are the neutron and proton numbers, Q_{W} is the nuclear weak charge quantifying the Z boson coupling strength, and the limit corresponds to the fully coherent regime where all nucleon contributions add constructively.

For nuclei with odd mass number and ground-state-to-ground-state transitions, axial-vector couplings are present, giving rise to contributions from transverse multipole operators. These nuclear responses are derived from the hadronic matrix elements, which are determined by the action of the multipole operators at the single-nucleon level. The nuclear structure factors then encode the many-body nuclear matrix elements of these single-nucleon currents, as described in Eq. (3.3.9). Within this framework and following Ref. [28], the axial contribution can be expressed as a combination of proton and neutron responses, as encoded in the Eq. (3.1.21).

After accounting for the kinematic development of the traces, the differential cross section, which includes the axial vector contribution, is expressed as the sum of the standard coherent term and the pure axial term[28, 85]:

$$\begin{aligned}\frac{d\sigma}{dE_r} = &\frac{G_F^2 m_N}{4\pi}\left(1 - \frac{m_N E_r}{2E_\nu^2} - \frac{E_r}{E_\nu}\right) Q_{\mathrm{W}}^2 |F_{\mathrm{W}}(q^2)|^2 \\ &+ \frac{G_F^2 m_N}{4\pi}\left(1 + \frac{m_N E_r}{2E_\nu^2} - \frac{E_r}{E_\nu}\right) F_{\mathrm{A}}(q^2) \ .\end{aligned} \tag{3.3.13}$$

here $G_F = 1.1663787 \times 10^{-5}\mathrm{GeV}^{-2}$ denotes the Fermi constant [83], m_N represents the nuclear mass, E_r is the nuclear recoil energy, E_ν is the energy of the incoming neutrino, and Q_{W} is the vector charge. F_{W} denotes the weak form factor, while F_{A} represents the axial form factor.

Chapter 4

Results and Discussion

With the theoretical framework for CEνNS established in the preceding chapters, this section presents the results and analysis of key observables: the differential cross section, nuclear form factors and predicted event rates for a specified detector configuration.

The isotopes studied are selected on two grounds: their connection to active CEνNS experiments and nuclear spin properties. Targets with non-zero ground-state spin are of particular interest because they enable investigation of the axial-vector contribution, which is nuclear-spin dependent. The COHERENT collaboration employs CsI and Ge targets at the SNS and has recently expanded its program to include reactor neutrinos with germanium detectors. Additionally, xenon targets have been employed by dark matter detection experiments to measure CEνNS.

Furthermore, ^{19}F is examined as a representative light nucleus with non-zero ground-state spin ($J^\pi = 1/2^+$). Its small atomic mass makes it especially sensitive to the axial-vector contribution. Studying ^{19}F provides a complementary case to the heavier targets discussed above and allows assessment of how nuclear structure effects evolve across the mass table. This comparison is relevant for evaluating the dependence of the CEνNS cross section on nuclear spin and size.

4.1 Form Factors

The Standard Model CEνNS cross section is governed by the nuclear response, which is encoded in the proton and neutron form factors. These quantities carry information about the internal nuclear structure and, in general, differ between protons and neutrons [12]. Nevertheless, in most practical treatments, they are taken to be equal, thereby reducing the nuclear form factor to a single global factor multiplying the cross section [86].

The form factors are introduced to account for the spatial distribution of nucleons within the nucleus and are defined as the Fourier transform of the nucleon density distribution [86, 87],

$$F(q^2) = \int e^{i\boldsymbol{q}\cdot\boldsymbol{r}}\rho(r)d^3\boldsymbol{r} \ , \tag{4.1.1}$$

here $\boldsymbol{q}$ denotes the momentum transfer in the scattering process, and ρ represents the probability density of the charge distribution [87]. This function is normalized such that $\int \rho(r)d^3\boldsymbol{r} = 1$ [88]. The form factor quantifies deviations from point-like nuclear behavior and suppresses the cross section as coherence diminishes with increasing momentum

transfer.

4.1.1 Coherent Form factor

In CEνNS, the axial contribution is nuclear spin-dependent, whereas the vector contribution is the dominant, coherent component. This coherent contribution is characterized by the weak form factor F_{W}. In principle, F_{W} can be constructed a priori using chiral effective field theory and nuclear many-body theoretical frameworks. However, these approaches introduce intrinsic theoretical uncertainties. Consequently, phenomenological parametrizations are generally preferred, as the associated theoretical uncertainty can be incorporated into the systematic uncertainty during statistical analysis [89].

This analysis uses a phenomenological form factor based on the Helm parametrization [88], with parameters set by experimental data and their uncertainties [86, 90]. In this model, the nuclear density is a uniform sphere of radius R_0 convolved with a Gaussian smearing kernel f_{G} of width s, to account for the finite diffuseness of the nuclear surface [11, 86]. The Helm density is [86]

$$\rho_{\mathrm{H}}(r) = \frac{3}{4\pi R_0^3} \int f_{\mathrm{G}}(\boldsymbol{r} - \boldsymbol{r}')\, \Theta(R_0 - |\boldsymbol{r}'|)\, d^3\boldsymbol{r}' \,, \tag{4.1.2}$$

where $\Theta(x)$ is the Heaviside step function enforcing the sharp boundary, and the Gaussian distribution

$$f_{\mathrm{G}}(\boldsymbol{x}) = \frac{e^{-x^2/2s^2}}{(2\pi)^{3/2} s^3} \tag{4.1.3}$$

acts as a smoothing kernel that replaces the hard edge with a realistic, continuously falling surface profile. The skin depth s controls how quickly the density drops from its bulk value to zero at the nuclear periphery.

The corresponding form factor, obtained as the Fourier transform of ρ_{H}, takes the compact analytical form

$$F_{\mathrm{H}}(q^2) = 3\, \frac{j_1(qR_0)}{qR_0}\, e^{-q^2 s^2/2} \,, \tag{4.1.4}$$

where $j_1(x) = \sin(x)/x^2 - \cos(x)/x$ is the first-order spherical Bessel function, and the parameter R_0 is related to the mean nuclear radius $R = 1.2\, A^{1/3}\,\mathrm{fm}$ and the surface thickness $s = 0.5\,\mathrm{fm}$ via $R_0 = \sqrt{R^2 - 5s^2}$ [11].

The form factor in Eq. (4.1.4) can be expressed as the product of two physically distinct contributions. The Bessel term encodes the diffraction pattern resulting from the finite nuclear volume, which leads to the characteristic oscillatory structure and zeros at large momentum transfer. In contrast, the exponential factor $e^{-q^2 s^2/2}$ introduces an overall damping that increases with s, indicating the suppression of high-q components due to the diffuse nuclear surface [86, 90]. Within the framework of coherent elastic neutrino–nucleus scattering, $F_H(q^2)$ determines the loss of coherence as q increases, thereby providing a quantitative relationship between measured cross sections and the spatial extent of the neutron distribution [11]..

4.1.2 Nuclear responses for axial contribution: Spin-dependent structure factors

In contrast to the vector contribution, the axial scattering rate has an intrinsic dependence on the nuclear spin and is therefore sensitive to nuclear structure. As a result, the axial form factor is governed by the nuclear response to an external axial-vector current and is significantly suppressed. Accurate determination of the axial form factor requires $ab-initio$ calculations that evaluate the relevant multipole matrix elements between nuclear states within a specified nuclear model.

The present analysis adopts the approach outlined in Ref. [28], which introduces a function for nuclear structure results for CEνNS based on nuclear shell model calculations. The methodology employs harmonic-oscillator single-particle matrix elements, as established in studies of nuclear structure factors relevant to direct dark matter detection. This framework enables analytical evaluation of the multipole operators and provides closed-form expressions for the nuclear response functions.

The full multipole expansion of the scattering amplitude, as presented in Eq. (2.3.33), includes contributions from the longitudinal ($\mathcal{L}$), Coulomb ($\mathcal{M}$), transverse electric ($\mathcal{T}^{\text{el}}$), and transverse magnetic ($\mathcal{T}^{\text{mag}}$) multipoles. Each term is weighted by the corresponding leptonic coefficients $l_3 l_3^*$, $l_0 l_0^*$, and $l_\lambda l_\lambda^*$. Analysis of the leptonic trace demonstrates that the longitudinal and Coulomb components are strongly suppressed in the kinematic regime $E_r \ll m_N$ relevant for CEνNS [28].

While the transverse magnetic multipoles vanish in elastic scattering as a result of time-reversal invariance [91]. Therefore, only the transverse electric multipoles $\mathcal{T}_L^{\text{el}}$ contribute with non-vanishing and kinematically unsuppressed terms, since they are even under time reversal and remain finite in the $T \to 0$ limit. These operators are directly associated with the transverse spin current of nucleons, and their nuclear matrix elements determine the spin-dependent structure factors when an appropriate parametrization is applied.

The parametrization of this multipole matrix element corresponds to the nuclear response $\mathcal{F}_{\pm}^{\Sigma'}$, where Σ' represents one of the seven fundamental operators associated with transverse electric multipoles (see Eq. (3.1.15)). This function arises as a proton or neutron combination, denoted $\mathcal{F}_{p,n}^{\Sigma'}$ [28]

$$\mathcal{F}_{\pm}^{\Sigma'_L}(q^2) = \mathcal{F}_p^{\Sigma'_L}(q^2) \pm \mathcal{F}_n^{\Sigma'_L}(q^2) \ . \tag{4.1.5}$$

The nuclear responses are parametrized through fit functions obtained from shell-model calculations performed in a harmonic oscillator single-particle basis [70].

As shown in Section 3.1.2, the evaluation of the corresponding radial integrals in the harmonic oscillator single-particle basis leads to a factorized structure. Specifically, this structure (present in the Eq. (3.1.21)) consists of a Gaussian term, multiplied by a polynomial in the dimensionless variable $u = \boldsymbol{q}^2 b^2/2$, where b is the oscillator length. This results in the compact expression

$$\mathcal{F}(u) = e^{-u/2} \sum_i c_i u^i \ , \tag{4.1.6}$$

the coefficients c_i represent the nuclear configuration information provided by the shell-model calculation.

The axial form factor, which includes contributions from all nucleons, consists of three components: the isoscalar term ($\mathcal{F}_+^{\Sigma'_L}$, p + n), the isovector term ($\mathcal{F}_-^{\Sigma'_L}$, p - n), and interference terms [90]. This formulation follows the approaches outlined in Refs. [28, 91].

$$F_{\mathrm{A}} = \frac{8\pi}{2J+1}\left[(g_{\mathrm{A}}^s)^2\mathcal{S}_{00}^{\mathcal{T}} - g_{\mathrm{A}}g_{\mathrm{A}}^s\mathcal{S}_{01}^{\mathcal{T}} + g_{\mathrm{A}}^2\mathcal{S}_{11}^{\mathcal{T}}\right] \ . \tag{4.1.7}$$

Here, J denotes the total angular momentum of the nucleus in its ground state. The parameter g_{A}^s represents the contribution of strange quarks to the spin structure, while g_{A} is the axial vector coupling of the nucleon and $\mathcal{S}_{ij}^{\mathcal{T}}$ are transverse spin-dependent structure factors.

The explicit expressions are given by:

$$\mathcal{S}_{00}^{\mathcal{T}} = \sum_L \left[\mathcal{F}_+^{\Sigma'_L}(\boldsymbol{q}^2)\right]^2 \ , \tag{4.1.8.a}$$

$$\mathcal{S}_{11}^{\mathcal{T}} = \sum_L \left[\left(1+\delta'(\boldsymbol{q}^2)\right)\mathcal{F}_-^{\Sigma'_L}(\boldsymbol{q}^2)\right]^2 \ , \tag{4.1.8.b}$$

$$\mathcal{S}_{01}^{\mathcal{T}} = \sum_L 2\left[1+\delta'(\boldsymbol{q}^2)\right]|\mathcal{F}_+^{\Sigma'_L}(\boldsymbol{q}^2)||\mathcal{F}_-^{\Sigma'_L}(\boldsymbol{q}^2)| \ . \tag{4.1.8.c}$$

In this expression, the sum extends over the contributing multipoles L. The term $\delta'(\boldsymbol{q}^2)$ denotes corrections beyond the leading spin-dependent coupling to the transverse response. The explicit form of this correction is provided in Refs. [28, 91].

This expression is employed to analyze the behavior of spin-dependent structure functions for selected isotopes, prioritizing those with the highest natural abundance and non-zero nuclear spin. The principal results presented here neglect quantum corrections. Within this approximation, the structure functions preserve the essential nuclear physics encoded, which are sufficient to capture the dominant features of the spin-dependent response at low momentum transfer. The justification for this omission, along with related analyses, is provided in Section 4.1.3.

Results for nuclear responses: Spin-dependent structure factors.

In studies of CEνNS, the COHERENT program is expected to incorporate various detector materials and detection technologies, all designed to measure low-energy nuclear recoils. These include the CsI[Na] scintillating crystal, which enabled the first observation of CEνNS, as well as an array of NaI crystals for charged-current measurements. In these configurations, measurements of nuclear recoil allow for the collection of both vector and axial current events, since both isotopes are odd-A, meaning they contain an unpaired nucleon and possess non-zero spin.

Furthermore, ESS is anticipated to achieve an order-of-magnitude increase in neutrino flux, thereby enabling precision studies of CEνNS. Advanced detector technologies, including those based on CsI, Xe, Ge, Ar, and C_3F_8, have been developed for this purpose [25]. In this context, only stable isotopes with non-zero spin ground states,

specifically ^{73}Ge, ^{129}Xe, ^{131}Xe, and ^{19}F, are capable of generating axial current events. The relevant isotopes, along with their natural abundances and ground-state spins, are summarized in Table. 4.1.

Isotope	Abundance (%)	Spin J
^{133}Cs	100	$\frac{7}{2}$
^{131}Xe	21.2	$\frac{3}{2}$
^{129}Xe	26.4	$\frac{1}{2}$
^{127}I	100	$\frac{5}{2}$
^{73}Ge	7.8	$\frac{9}{2}$
^{23}Na	100	$\frac{3}{2}$
^{19}F	100	$\frac{1}{2}$

Table 4.1: Isotopes relevant for CEνNS that possess non-zero nuclear ground-state spin ($J \neq 0$), along with their natural abundances [92], are of particular interest. Only isotopes with $J \neq 0$ contribute to the spin-dependent (axial) response, which is essential for investigating the axial-vector sector of the weak interaction.

To fully characterize the spin-dependent observables of the process, the transverse SD structure factors $\mathcal{S}_{ij}^{\mathcal{T}}(q^2)$ are evaluated from Eq. (4.1.8) for the isotopes of interest listed in Table 4.1, and are shown as a function of momentum transfer in Fig. 4.1. The structure factors exhibit the typical behavior of nuclear form factors: as the momentum transfer q increases, the nuclear response loses coherence because the probe begins to resolve the internal structure of the nucleus, leading to a progressive suppression of $\mathcal{S}_{ij}^{\mathcal{T}}$ at large q.

A key distinction from the coherent weak form factor, which is normalized to unity at $q^2 = 0$ [84, 12], is that the SD structure factors are normalized through the proton and neutron spin expectation values $\langle S_p \rangle$ and $\langle S_n \rangle$ [28]

$$\mathcal{F}_N^{\Sigma'}(0) = \sqrt{\frac{2}{3}} \sqrt{\frac{(2J+1)(J+1)}{4\pi J}} \langle S_N \rangle \ . \tag{4.1.9}$$

This normalization depends on the total spin of the nucleus J and the spin of the unpaired nucleon, which is why the values of $\mathcal{S}_{ij}^{\mathcal{T}}$ at $q^2 = 0$ differ between isotopes and are generally small.

For ^{133}Cs, ^{127}I, ^{23}Na, and ^{19}F, the nuclear spin is primarily determined by an unpaired proton. In contrast, for ^{129}Xe, ^{131}Xe, and ^{73}Ge, the dominant contribution arises from an unpaired neutron. This distinction facilitates direct interpretation of the structure factors in terms of the spin expectation values $\langle S_p \rangle$ and $\langle S_n \rangle$, which are shown in Table 4.2.

These results provide a consistent explanation for the behavior of the structure factors in the limit $q \to 0$. Comparing panels (a) and (b), clear differences emerge that can be traced back to both the nucleon spin content and the normalization factor, which is explicitly dependent on the total nuclear spin J. In particular, xenon isotopes exhibit significantly smaller values, indicating reduced effective spin contributions within their nuclear structure. In panel (c), the structure factor for ^{23}Na is suppressed relative to ^{19}F and ^{73}Ge, consistent with its lower value of $\langle S_p \rangle$. Although ^{19}F and ^{73}Ge possess similar spin expectation values, the response of germanium is enhanced due to the normalization factor's dependence on J, which increases its contribution.

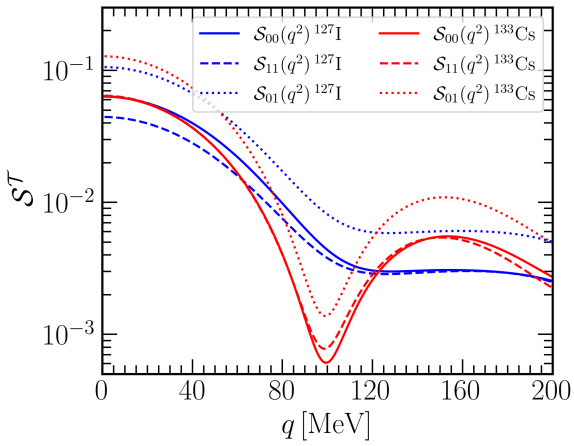

(a) ^{133}Cs and ^{127}I

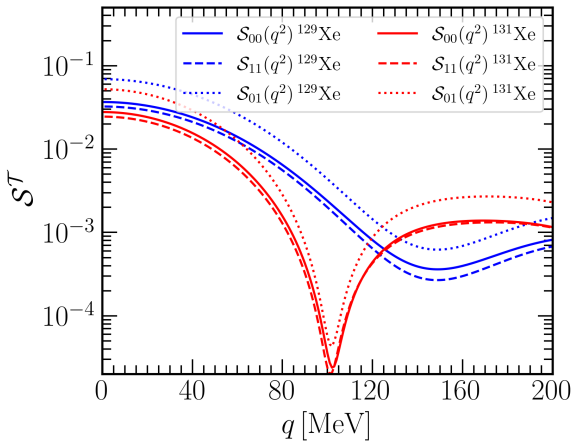

(b) ^{129}Xe and ^{131}Xe

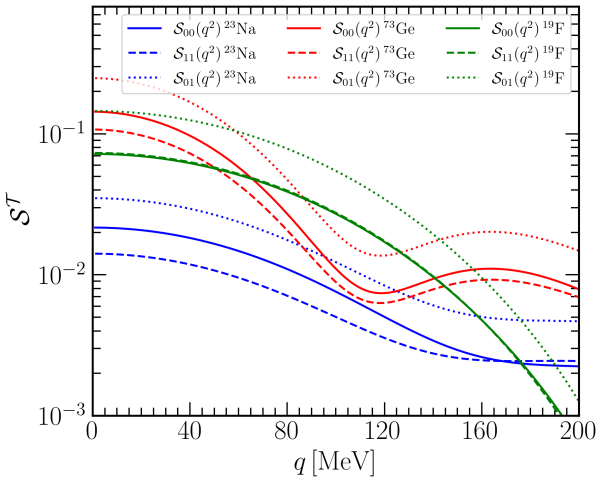

(c) ^{23}Na, ^{73}Ge, ^{19}F

Figure 4.1: Transverse spin-dependent (SD) structure factors $\mathcal{S}^{\mathcal{T}}_{ij}(q^2)$ $(i,j=0,1)$ as a function of the momentum transfer q, computed within the nuclear shell model. Components shown are the isoscalar $\mathcal{S}^{\mathcal{T}}_{00}$ (solid), isovector $\mathcal{S}^{\mathcal{T}}_{11}$ (dashed), and interference term $\mathcal{S}^{\mathcal{T}}_{01}$ (dotted). Panel (a): ^{133}Cs (red) and ^{127}I (blue). Panel (b): ^{129}Xe (blue) and ^{131}Xe. Panel (c): ^{23}Na (blue), ^{73}Ge (red), and ^{19}F (green).

Collectively, these results demonstrate that the normalization of the structure factors depends in a non-trivial manner on both the total nuclear spin and the spin expectation value of the unpaired nucleon. This combined dependence determines which nuclei exhibit a more pronounced axial response. Within this framework, isotopes such as ^{133}Cs and ^{127}I are suitable candidates, while ^{19}F and ^{73}Ge are particularly favorable due to their relatively large structure factor values, making them especially sensitive probes for extracting axial information.

The oscillatory behavior observed as a function of q originates mathematically from the spherical Bessel functions $j_L(qr)$ [93], which are encoded in the functions $\mathcal{F}^{\Sigma'}$ as expressed in Eqs. (4.1.8). At specific values of q, these functions exhibit minima that depend on the nuclear radius, following $q_{\min} = \frac{x_{\min}}{R_A}$, where $x_{\min}$ denotes the first minimum of the Bessel function and $R_A = 1.2A^{1/3}$ fm. Thus, the position of a pronounced minimum is determined by the size of the nucleus [84].

Isotope	^{19}F	^{23}Na	^{73}Ge	^{127}I	^{129}Xe	^{131}Xe	^{133}Cs
$\langle S_p \rangle$	0.478	0.224	0.032	0.346	0.010	-0.009	-0.343
$\langle S_n \rangle$	-0.002	0.024	0.439	0.031	0.329	-0.272	0.001

Table 4.2: Shell-model proton ($\langle S_p \rangle$) and neutron ($\langle S_n \rangle$) spin expectation values for the odd-mass isotopes analyzed in this study. The explicit values are taken from Hoferichter, Menéndez, and Schwenk [28]. These parameters characterize the dominant nuclear spin contribution and determine the overall magnitude of the spin-dependent structure factors in the low-momentum-transfer limit.

Physically, as q increases, the probe's de Broglie wavelength approaches the nuclear size, thereby satisfying the coherence condition. As a result, the contributions from nucleons within the nucleus acquire different phases, leading to destructive interference in the nuclear response. Heavier nuclei, therefore, exhibit peaks at lower values of q, as demonstrated by the comparison of the three panels in Fig. 4.1. Beyond this mass dependence, the nuclear spin plays an equally important role in shaping the structure factors, as discussed below.

The influence of nuclear spin is most clearly demonstrated by comparing isotopes of similar mass but different spin. Fig. 4.1b presents ^{129}Xe and ^{131}Xe, which have nearly identical masses but differ in nuclear spin: $J = 1/2$ for ^{129}Xe and $J = 3/2$ for ^{131}Xe (see Table 4.1). The higher spin of ^{131}Xe permits contributions from higher-order multipoles ($L = 1, 3$ rather than $L = 1$ alone), resulting in stronger destructive interference at specific values of q [28]. This effect is evident in the figure: the ^{131}Xe curves display a more pronounced minimum around $q \sim 100$–110 MeV, whereas the ^{129}Xe curves decrease more smoothly. An analogous behavior is observed in Fig. 4.1a, where ^{133}Cs and ^{127}I, despite having comparable masses, exhibit markedly different structure factors due to their distinct nuclear spins.

Figure 4.1c demonstrates the combined effect of varying both mass and spin by comparing three nuclei across a broad range of these parameters. At one extreme, ^{19}F has spin $J = 1/2$ and a small nuclear radius ($R = 2.8976$ fm [28]); its first minimum is shifted to $q > 200$ MeV, beyond the displayed range, resulting in a monotonically decreasing structure factor.

At the other extreme, ^{73}Ge is significantly heavier and has a high spin of $J = 9/2$. Its greater mass brings the first minimum within the shown range, while the high spin allows contributions from multiple multipoles ($L = 1, 3, 5, 7, 9$), producing the non-monotonic behavior visible in the figure. ^{23}Na represents an intermediate case: its moderate mass and spin $J = 3/2$ place it between these two extremes, exhibiting mild suppression at intermediate momentum transfers. These three examples collectively demonstrate that the interplay between nuclear mass and spin determines both the position and the shape of the minima in the spin-dependent structure factors.

At a fundamental level, the behavior of spin-dependent structure factors arises from their origin in the axial current. Unlike the coherent response, which is dominated by the charge operator and sums constructively over all nucleons, the factors $\mathcal{S}_{ij}^{\mathcal{T}}(q^2)$ are determined by operators proportional to the nucleon spin, $\boldsymbol{\sigma}_i$. Consequently, their magnitude depends on the spin structure of the nuclear ground state rather than the total nucleon

number.

Then as demonstrated in Ref. [28], the structure factors are constructed from combinations of the proton and neutron axial form factors

$$\begin{aligned} S_p &= \mathcal{S}_p^{\mathcal{T}} \\ &= \sum_L \left[2\mathcal{F}_p^{\Sigma'_L}(q^2) + \delta(q^2) \left(\mathcal{F}_p^{\Sigma'_L}(q^2) - \mathcal{F}_n^{\Sigma'_L}(q^2) \right) \right]^2 , \end{aligned} \tag{4.1.10}$$

$$\begin{aligned} S_n &= \mathcal{S}_n^{\mathcal{T}} \\ &= \sum_L \left[2\mathcal{F}_n^{\Sigma'_L}(q^2) - \delta(q^2) \left(\mathcal{F}_p^{\Sigma'_L}(q^2) - \mathcal{F}_n^{\Sigma'_L}(q^2) \right) \right]^2 \end{aligned} \tag{4.1.11}$$

This explicit construction demonstrates that the structure factors result from combinations of the proton and neutron axial form factors.

Consequently, for a given nucleus, the isovector and isoscalar response shapes are similar, as both are primarily governed by $S_p(q^2)$ in nuclei with an unpaired proton or by $S_n(q^2)$ in nuclei with an odd number of neutrons. This observation further supports the conclusion that spin-dependent structure factors are determined by the distribution and correlations of nucleon spin within the nucleus [28].

4.1.3 Axial Current Corrections in CEνNS

At leading order, the axial current is represented by a one-body (1b) operator. In this framework, each nucleon is considered independently, and the neutrino interacts with a single nucleon at a time. This approach establishes the baseline for describing the axial response in nuclei (Results Section 4.1.2). Nevertheless, beyond this leading contribution, additional corrections arise from the nuclei's internal structure.

Specifically, the finite spatial extent of the axial charge distribution is characterized by the axial root-mean-square (rms) radius. Under the assumption of spherical symmetry, the axial form factor is expanded at low momentum transfer as follows [94, 95]

$$F_{\mathrm{A}}(Q^2) = F_{\mathrm{A}}(0) - \frac{\langle r_{\mathrm{A}}^2 \rangle}{3!} q^2 + \frac{\langle r_{\mathrm{A}}^4 \rangle}{5!} q^4 + \cdots , \tag{4.1.12}$$

where $\langle r^2 \rangle_{\mathrm{A}}$ denotes the spatial distribution of the axial charge within the nucleon. This correction results in a moderate suppression of the axial response as the momentum transfer increases.

Chiral EFT provides a more fundamental and systematic basis for nuclear forces and electroweak currents [96]. Within this framework, nucleon-nucleon interactions are mediated by pion and meson exchanges [97]. These processes give rise to two-body (2b) currents, which contribute alongside standard one-body operators.

At leading order, the axial one-body (1b) current is governed by the coupling g_{A}, while the leading axial 2b-body contributions are characterized by the low-energy constants c_3, c_4, and c_D [96]. For the processes considered here, the dominant weak 2b-body currents

have only a spatial axial component [28]. The explicit form of these currents is given below:

$$\mathbf{J}_{2b} = \sum_{i<j}^{A} \mathbf{J}^3_{ij} \,, \tag{4.1.13}$$

where $\mathbf{J}^3_{ij}$ denotes the axial 2b-body current operator (see Refs. [28, 96] for explicit expressions).

To incorporate these contributions into nuclear structure calculations, it is necessary to account for the normal-ordered one-body component of chiral two-body currents. This component is obtained by summing the second nucleon j over occupied states within a spin- and isospin-symmetric reference state, assumed here to be a Fermi gas [96]:

$$\mathbf{J}^{\text{eff}}_{i,\,2\text{b}} = \sum_{j} (1 - P_{ij})\; \mathbf{J}^{(3)}_{ij} \,. \tag{4.1.14}$$

The exchange operator P_{ij} includes all 2b-body exchange contributions. Consequently, axial-vector two-body currents are transformed into effective one-body currents [28]. In the case where the total momentum $\mathbf{P} = 0$, the 2b-body current contribution to the axial component can be expressed as:

$$\mathbf{J}^{\text{eff}}_{i,2\text{b}}(\rho, \boldsymbol{q}) = g_{\text{A}} \boldsymbol{\sigma_i} \frac{\tau_i^3}{2} \delta_a(q^2) \;, \tag{4.1.15}$$

with

$$\begin{aligned} \delta a(q^2) = &- \frac{\rho}{F_\pi^2} \Bigg[\frac{c_4}{3} \left(3I_2^\sigma(\rho, |\mathbf{q}|) - I_1^\sigma(\rho, |\mathbf{q}|)\right) - \frac{1}{3} \left(c_3 - \frac{1}{4m_N} \right) I_1^\sigma(\rho, |\mathbf{q}|) \\ &- \frac{c_6}{12} I_{c_6}(\rho, |\mathbf{q}|) - \frac{c_D}{4 g_A \Lambda_\chi} \Bigg] \,. \end{aligned} \tag{4.1.16}$$

These contributions depend on the density of the reference state, $\rho = 2k_{\text{F}}^3/3\pi^2$, where k_{F} denotes the Fermi momentum, as well as on the low-energy couplings c_3, c_4, and c_D. The functions $I_1^\sigma(\rho, |\mathbf{q}|)$, $I_2^\sigma(\rho, |\mathbf{q}|)$, $I^P(\rho, |\mathbf{q}|)$, and $I_{c6}(\rho, |\mathbf{q}|)$ are defined by integrals arising from the summation over occupied states in the exchange terms. The low-energy coupling constants have been determined from experimental data [91].

By incorporating both nucleon finite-size effects and two-body contributions, the total correction to the axial current is given by

$$\delta'(q^2) = -\frac{q^2 \langle r_A^2 \rangle}{6} + \delta a(q^2) \,. \tag{4.1.17}$$

These corrections have a clear physical interpretation. The finite axial radius introduces a suppression of the form factor at increasing momentum transfer, while the 2b-body currents generate an additional term of the axial coupling due to nucleon–nucleon correlations.

Fig. 4.2 presents the spin-dependent structure functions for a representative set of isotopes chosen to probe contrasting regimes of nuclear mass and total spin. This selection allows for a direct comparative analysis of how each correction affects the axial response

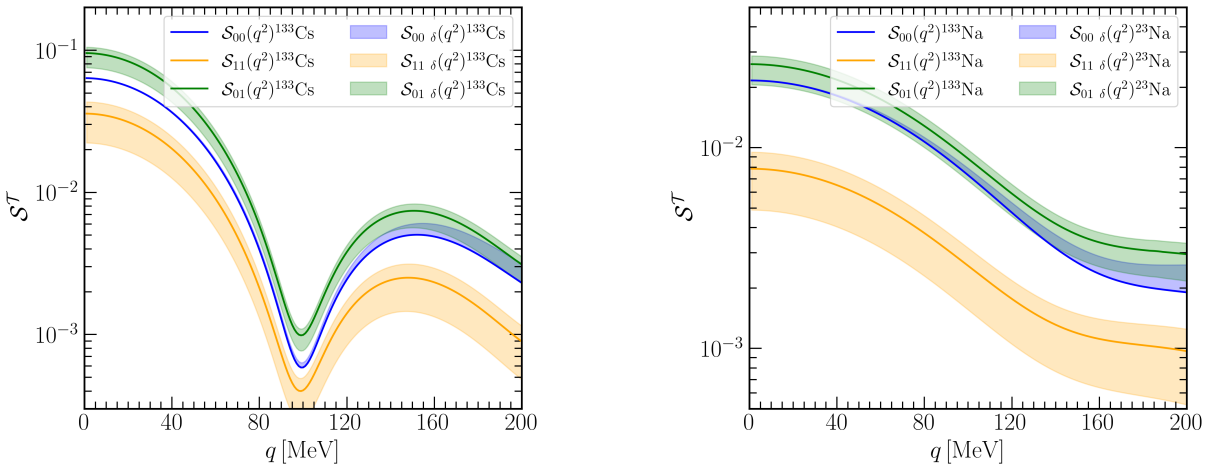

(a) ^{133}Cs **(b)** ^{23}Na

Figure 4.2: Structure factors $S^{\mathcal{T}}(q^2)$ including quantum corrections for two representative nuclei: (a) the heavy, large-spin nucleus ^{133}Cs, and (b) the lighter, small-spin nucleus ^{23}Na. Solid lines denote the uncorrected (one-body) results, while shaded bands represent the inclusion of two-body current contributions and radius corrections.

across different nuclear configurations. As a general trend, both the finite axial radius and the two-body currents reduce the overall magnitude of the structure functions, with the suppression becoming more pronounced at higher momentum transfer where the form factor effects are most significant.

Quantum corrections influence only $S^{\mathcal{T}}_{11}$ and $S^{\mathcal{T}}_{01}$, whereas $S^{\mathcal{T}}_{00}$ remains unaffected by 2b-body currents. This selectivity results from the isovector character of the axial 2b-body currents. These currents, mediated by pion exchange with isospin $T = 1$, depend on the isospin operator τ^3 and thus contribute exclusively to structure functions with isovector character. In contrast, the isoscalar component $S^{\mathcal{T}}_{00}$ only receives corrections through the axial radius term. This term becomes relevant at higher q^2.

At low momentum transfer, the width of the uncertainty band in $S^{\mathcal{T}}_{11}$ and $S^{\mathcal{T}}_{01}$ is primarily determined by the uncertainty in the low-energy coupling $c_D \in [-6.08, +0.30]$ [28]. This coupling appears as a constant term $c_D/(4g_A\Lambda_\chi)$ in $\delta a(q^2)$. More negative c_D values further suppress the structure functions, which broadens the band toward lower values. At higher momentum transfer, the dominant uncertainty arises from c_3 and c_4 through the loop functions $I^{\sigma}_{1,2}(\rho, |\mathbf{q}|)$. The axial radius term adds momentum dependence, further amplifying this uncertainty and increasing sensitivity to q in this regime.

Although momentum-dependent axial corrections are available, these corrections are not incorporated into the CEνNS calculations presented in this study. Two-body currents and the finite axial radius act to reduce the axial response; however, their influence on CEνNS observables remains minor. This is primarily due to the dominance of the coherent vector contribution dominates and current experimental limitations [98]. As a result, these effects are expected to be less significant than the experimental uncertainties associated with extracting the axial-current contribution itself [89]. This assumption is particularly justified for initial measurements that focus on the axial component in CEνNS.

4.2 Cross Sections and Event Rates

4.2.1 Cross Section for different isotopes

Following the determination of the coherent and axial form factors, the total ν-nucleus cross sections are computed using numerical integration of Eq. (3.3.13). The results, shown in Fig. 4.3, present the Standard Model cross section in cm^2 as a function of recoil energy E_r in keV for several relevant target nuclei. The cross section is separated into coherent (vector) and spin-dependent (axial-vector) contributions.

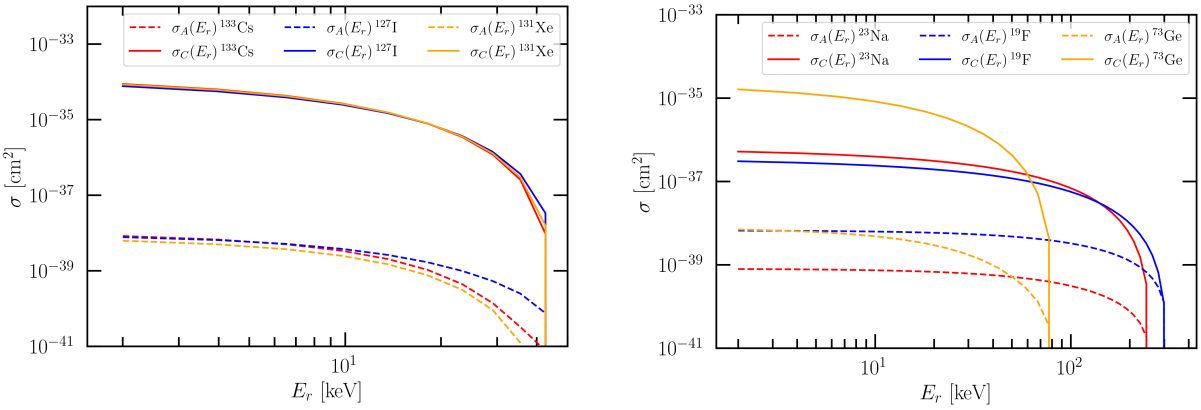

(a) ^{133}Cs ,^{127} I and ^{131}Xe **(b)** ^{23}Na, ^{19}F and ^{73}Ge

Figure 4.3: Total CEνNS cross sections in the Standard Model dictated by Ref. [28], are shown as a function of nuclear recoil energy E_r for selected target nuclei. Solid lines represent the coherent (vector) contribution σ_C, while dashed lines indicate the spin-dependent (axial-vector) contribution σ_A, which is suppressed due to its sensitivity only to the spin of the unpaired nucleon. The left panel presents results for heavy nuclei: ^{133}Cs, ^{127}I, and ^{131}Xe. The right panel displays results for light nuclei: ^{23}Na, ^{19}F, and ^{73}Ge.

The behavior of the vector current is governed by N^2. As shown in Q_{W}^2 (Eq. (3.3.12)), the value $\sin^2\theta_W \simeq 0.231$ is approximately $1/4$. As a result, the proton contribution, which is proportional to Z, is significantly suppressed compared to the neutron contribution. Electroweak theory thus predicts that the cross section scales as $\frac{d\sigma}{dT} \propto N^2$. This scaling characterizes the fully coherent regime, where contributions from all nucleons add constructively. However, this coherent enhancement is modulated by the nuclear form factor $F_{\mathrm{W}}(q^2)$, which accounts for the finite size of the nucleus and introduces a momentum-transfer-dependent suppression [99].

In contrast, the Standard Model (SM) axial vector contribution to the CEνNS cross section is subdominant relative to the vector component, as it is highly suppressed by nuclear spin. Although all nucleons couple to the axial current, in even-even nuclei the individual spin contributions cancel pairwise, resulting in $J = 0$ and, consequently, no axial response. In odd-mass nuclei, the axial contributions arise from unpaired nucleons that possess a non-zero net spin, for which the numbers are typically much smaller than the total number of nucleons. Therefore, the axial contribution survives [99], but it remains strongly suppressed, as illustrated in Fig. 4.3.

A comparison of the two panels indicates that the cross sections differ by one to two orders of magnitude between light and heavy nuclei for both coherent and spin-dependent contributions. This outcome demonstrates the pronounced dependence on nuclear mass

number and the corresponding form factor suppression.

Figure 4.3b demonstrates that the relative contributions of the axial-vector and coherent terms vary significantly among the three nuclei. In ^{19}F and ^{23}Na, the similar numbers of protons and neutrons result in the N^2 scaling of σ_C providing only a modest enhancement, which maintains a relatively small difference between σ_C and σ_A. Additionally, the substantial proton spin expectation values for both nuclei ($\langle S_p \rangle = 0.478$ and 0.224, respectively) [28] further amplify the axial structure functions and preserve a notable spin-dependent contribution.

The case of ^{73}Ge is qualitatively distinct. While its high nuclear spin ($J = 9/2$) produces a complex multipole structure capable of supporting a substantial axial response, the large neutron number ($N = 41$) causes $\sigma_C \propto N^2$ to greatly exceed σ_A. As a result, the spin-dependent contribution becomes negligible in the total cross section. This comparison between ^{73}Ge and lighter nuclei highlights a fundamental competition in CEνNS: although nuclear spin structure shapes the spin-dependent response, the coherent enhancement driven by the neutron number ultimately determines the dominant contribution.

This analysis indicates that light nuclei with an unpaired nucleon, such as ^{19}F or ^{23}Na, are preferable for maximizing the spin-dependent signal, as the minimum occurs at larger values of q and the axial contribution remains a non-negligible fraction of the total cross section. In contrast, heavy nuclei such as ^{133}Cs, ^{127}I, ^{131}Xe, or ^{73}Ge present an axial cross section of comparable absolute magnitude to that of lighter nuclei; however, it is overwhelmingly dominated by the coherent contribution, rendering the spin-dependent response effectively negligible in the total cross section.

4.2.2 Total Number of Events

The subsequent step in this procedure involves calculating the number of events. Given an expression for the cross section, the CEνNS differential event rate spectra are obtained by convoluting the CEνNS differential cross section with the neutrino fluxes $\Phi(E_\nu)$. For the α-th flux, the expression is given by [100, 98]:

$$\frac{dN}{dE_r} = \mathcal{N} \times \sum_{\alpha=\nu_e,\nu_\mu,\bar{\nu}_\mu} \int_{E_\nu^{\min}}^{E_\nu^{\max}} dE_\nu \, \frac{d\sigma(T, E_\nu)}{dT} \, \frac{d\phi_\alpha(E_\nu)}{dE_\nu} \tag{4.2.1}$$

and finally the total number is:

$$N = \int_{E_r^{\min}}^{E_r^{\max}} \frac{dN}{dE_r} \, dE_r \, . \tag{4.2.2}$$

here:

- $\mathcal{N}$ is a normalization factor and depends of detector parameters, the expression is:

$$\frac{m_{\text{det}} \, N_A \, n_{\text{POT}} \, r \, \varepsilon_f}{4\pi L^2 \, m_M} \, , \tag{4.2.3}$$

  with m_{det} represents the mass of the detector, $N_A = 6.02214076 \times 10^{23}$ mol^{-1} is Avogadro's number [83], n_{POT} denotes the total number of protons on target (POT) delivering neutrinos during the exposure period, r specifies the number of neutrinos

per flavor produced per proton on target, ε_f indicates the detector efficiency or acceptance, L is the distance from the detector to the neutrino source, and m_M is the molar mass of the detector [25, 13].

- Neutrino fluxes are determined by their source characteristics. At the SNS and ESS, as described in Section 3.2.1, low-energy neutrinos are produced from the decay of pions at rest, followed by subsequent muon decay. Muon neutrinos result from two-body decay processes; consequently, they are monochromatic, with their energy determined by the pion and muon masses: $E_{\nu_\mu} = \frac{m_\pi^2 - m_\mu^2}{2m_\pi} \simeq 30\,\text{MeV}$. In contrast, the signal from the three-body decay mode involves two continuous spectra governed by the differential decay rate of the muon. The differential neutrino energy spectra are given by [100, 85]:

$$\frac{d\Phi_{\nu_\mu}(E_\nu)}{dE_\nu} = \delta\left(E_\nu - \frac{m_\pi^2 - m_\mu^2}{2m_\pi}\right) \quad \text{(prompt)}\,, \tag{4.2.4a}$$

$$\frac{d\Phi_{\bar{\nu}_\mu}(E_\nu)}{dE_\nu} = \frac{64E_\nu^2}{m_\mu^3}\left(\frac{3}{4} - \frac{E_\nu}{m_\mu}\right) \quad \text{(delayed)}\,, \tag{4.2.4b}$$

$$\frac{d\Phi_{\nu_e}(E_\nu)}{dE_\nu} = \frac{192E_\nu^2}{m_\mu^3}\left(\frac{1}{2} - \frac{E_\nu}{m_\mu}\right) \quad \text{(delayed)}\,. \tag{4.2.4c}$$

  The total neutrino flux is considered to be the sum of the three previous contributions.

- The limits of the E_r integral are set by the detector threshold and the maximum recoil energy for a fixed E_ν, which can be approximated as $E_{r\max}(E_\nu) = 2E_\nu^2/M$. In comparison, the upper limit for the E_ν integral is 52.8 MeV, reflecting the highest neutrino energy produced by the SNS or ESS.

This study examines a specific experimental scenario for CEνNS. Two of the most intense spallation neutrino sources currently available are the SNS and the ESS. Both facilities generate neutrino fluxes through pion decay-at-rest, as detailed in Section 3.2.1, resulting in identical neutrino flavors and spectral distributions. Despite this similarity, the sources differ substantially in their operational characteristics, which leads to variations in total neutrino fluxes and, consequently, in total event rates.

Having characterized the coherent and spin-dependent cross sections, the analysis proceeds to the expected number of CEνNS events in realistic detector configurations. This quantity establishes a more direct connection to experimental observables and enables assessment of which target nuclei provide the greatest sensitivity to the axial-vector contribution under practical detection conditions.

Tables 4.3 and 4.4 show the expected CEνNS event rates at the SNS and ESS. Each table separates the rates into coherent and axial contributions for the detector targets of interest. All detector setups assume a mass of 50 kg, efficiency $\varepsilon = 80\%$, baseline $L = 20$ m, and energy threshold $E_r^{th} = 2$ keV [25]. The analysis accounts for the unique characteristics of each source. Average production rates are $r = 0.08$ and $r = 0.3$ neutrinos of each flavor per proton, with $n_{\text{POT}} = 1.76 \times 10^{23}$ for SNS and $n_{\text{POT}} = 2.8 \times 10^{23}$ for ESS.

The data indicate that ESS produces approximately 18 times more events than SNS across all targets and contributions. The reason for this is obviously the effective neutrino

Detector	Coherent Events	Axial Events
CsI	2 138	0.165
NaI	1 855	0.286
Ge	1 422	0.96
Xe	2 170	0.206

Table 4.3: Expected CEνNS event rates at SNS parameters for various detector targets, indicating the number of events from coherent and axial contributions. Calculations are based on Eqs. (4.2.1) and (4.2.2) with $m_{\text{det}} = 50$ kg and a 20 m baseline.

Detector	Coherent Events	Axial Events
CsI	38 273	3
NaI	33 209	5
Ge	25 467	17
Xe	38 838	3

Table 4.4: Expected CEνNS event rates at ESS parameters for various detector targets, indicating the number of events from coherent and axial contributions. Calculations are based on Eqs. (4.2.1) and (4.2.2) with $m_{\text{det}} = 50$ kg and a 20 m baseline.

yield, defined as the product $r \cdot n_{\text{POT}}$, which is 1.41×10^{22} at SNS and 8.4×10^{22} at ESS including the exposure time, where for SNS it is considered to be only 1 year, while for ESS it is 3 years. The higher yield at ESS makes it the optimal source for probing the axial-vector contribution. Therefore, ESS is used as the reference source for subsequent analyses of different targets.

It should be emphasized that despite this improvement, the axial-vector contribution remains highly suppressed at both neutrino sources, accounting for at most $\sim 7\%$ of the total event rate in the most favorable case, corresponding to ^{73}Ge. To further characterize this behavior, Fig. 4.4 presents the differential recoil energy spectra for both the coherent and spin-dependent contributions, assuming a 50 kg detector exposed to the ESS neutrino flux. The comparison focuses on the detector compounds most relevant to current CEνNS experiments: NaI, CsI, germanium, and xenon.

The coherent component dominates the event rate for all targets, exceeding the axial contribution by several orders of magnitude across the entire recoil energy range. The bulk of events is concentrated at low recoil energies and decrease rapidly with increasing E_r. The observed hierarchy in coherent rates directly confirms the expected $\propto N^2$ scaling. CsI, NaI, and ^{131}Xe yield comparable and dominant event rates, whereas ^{73}Ge exhibits suppression due to its lower neutron number. These results indicate that heavy targets are optimal for maximizing coherent statistics. However, this same characteristic renders them less suitable for isolating the axial-vector contribution, thereby establishing a fundamental experimental tension.

The spin-dependent event rates, as depicted in the right panel, are significantly suppressed across all targets. However, their relative magnitudes reflect the underlying nuclear spin structure. In particular, ^{73}Ge exhibits the highest axial event rate at low recoil energies. This is consistent with its complex multipole structure associated with its high

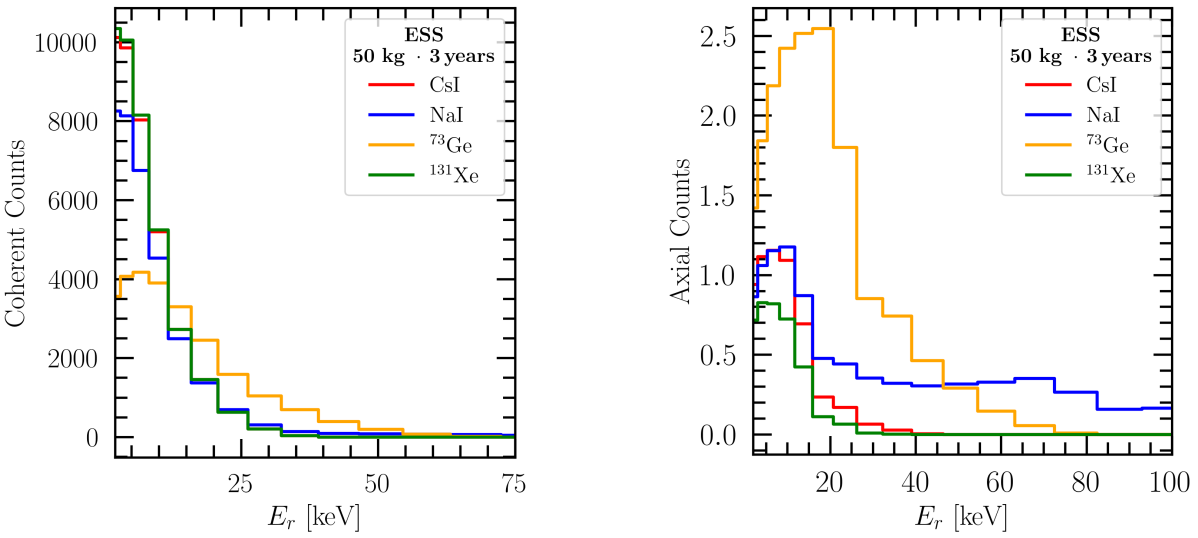

(a) Spectrum event rate coherent events.

(b) Spectrum event rate axial events.

Figure 4.4: Event-rate spectrum for the coherent (vector) and axial-current contributions to CEνNS are presented for a 50 kg detector exposed to a spallation neutron source neutrino flux over a three-year period at an ESS facility. The experimental configuration assumes a baseline of $L = 20$ m, a proton beam power of 1.3 MW, a uniform detection acceptance of 80%, and a nuclear recoil energy threshold of 2 keV. Panel (a) displays the coherent (vector) event-rate spectrum for CsI, considered as the primary odd-A nucleus, in comparison with NaI (^{23}Na and ^{127}I), ^{73}Ge, and ^{131}Xe targets. Panel (b) shows the axial-current event-rate spectrum for NaI and CsI detectors, along with the contributions from ^{73}Ge and ^{131}Xe, calculated using *ab initio* shell-model spin structure functions.

spin ($J = 9/2$), as previously in the structure factor analysis of Section 4.1.2. Other nuclei with substantial unpaired nucleon spin expectation values, such as ^{23}Na ($\langle S_p \rangle = 0.224$) and ^{127}I ($\langle S_p \rangle = 0.346$, $\langle S_n \rangle = 0.031$) [28], also display comparatively higher axial contributions. Nonetheless, even in these favorable scenarios, the axial signal is dominated by the coherent rate. This highlights the experimental difficulty in isolating the spin-dependent component in current CEνNS measurements.

The total event rates presented in Tables 4.3 and 4.4, as well as the curves shown in Fig. 4.4, demonstrate that the axial-vector contribution remains strongly subdominant for both the SNS and ESS sources across all targets considered. This suppression arises directly from nuclear structure. As established in Section 4.1.2, the spin-dependent response is governed by the unpaired nucleon spin, which is intrinsically limited in standard detector compounds. The coherent enhancement consistently dominates the axial signal for all neutrino sources.

The results demonstrate that the primary constraint in accessing the spin-dependent contribution is determined by the choice of target nucleus, rather than by experimental parameters. Coherent enhancement remains the dominant effect regardless of the neutrino source. Isolating the axial-vector component requires the use of nuclei with significant unpaired nucleon spin, as reflected by large $\langle S_p \rangle$ and $\langle S_n \rangle$ values, and a relatively low mass number to reduce form factor suppression. Representative examples are shown in the Table. 4.5:

Isotope	Abundance (%)	Spin J
^{29}Si	26.4	$\frac{1}{2}$
^{27}Al	100	$\frac{5}{2}$
^{19}F	100	$\frac{1}{2}$
^{3}He	0.013	$\frac{1}{2}$

Table 4.5: Candidate isotopes for spin-dependent CEνNS searches, selected on the basis of non-zero nuclear spin and relatively light mass number. Natural abundances are taken from Ref. [92].

Table 4.5 lists isotopes meeting these criteria, but a closer look reveals practical limitations. The natural abundance of ^{3}He is only parts per million, requiring much larger detector masses for reliable statistics. ^{27}Al has emerged as a candidate, yet there is currently no information on its use in CEνNS experiments. For ^{29}Si, the CONNIE experiment uses silicon-based detectors [80]. The detector installed in 2016 has an active mass of 73.2 g, which strongly limits the number of axial events. Although lowering the recoil-energy threshold could increase axial event rates in principle, the expected signal remains too small [89].

Among the candidate targets discussed above, fluorine-based compounds represent the most promising option for spin-dependent CEνNS searches. Materials such as C_4F_{10}, CF_4, and C_3F_8 [89] exhibit two advantageous characteristics: the carbon component ($A = 12$) possesses nearly equal numbers of protons and neutrons and zero nuclear spin, resulting in a negligible contribution to the coherent cross section. In contrast, fluorine (^{19}F, $J = 1/2$) has a large proton spin expectation value and a low mass number, both of which support a comparatively strong axial-vector response.

This combination reduces the N^2 coherent enhancement relative to heavier targets while preserving the spin-dependent signal, making fluorocarbon compounds particularly effective for isolating the axial contribution. Based on these findings, Fig. 4.5 displays the differential recoil energy spectra for these three compounds using the same ESS configuration as in the heavy-target analysis.

The left panel shows that the coherent event rates have nearly identical curves. This is expected, since the coherent rate depends on the square of the total neutron number, which is similar among the compounds. The spectral shape is similar to that of heavier compounds. However, the absolute event rates are substantially lower than those for CsI or NaI due to the lighter nuclear masses of fluorine and carbon. In contrast, the right panel displays a spectrum that differs from those of heavier compounds. The observed decrease follows a distinct structural pattern in fluoride. The spectral degeneration results directly from the axial nuclear responses of fluoride.

A key observation emerges from comparison with Fig. 4.4. In contrast to the heavy-target case, where the axial contribution was negligible, the difference between coherent and axial components is now significantly reduced. Consequently, the spin-dependent contribution constitutes a substantial portion of the total event rate. This effect is particularly pronounced at low recoil energies, where the axial response of fluorine is most significant, as indicated by the structure factor in Fig. 4.2.

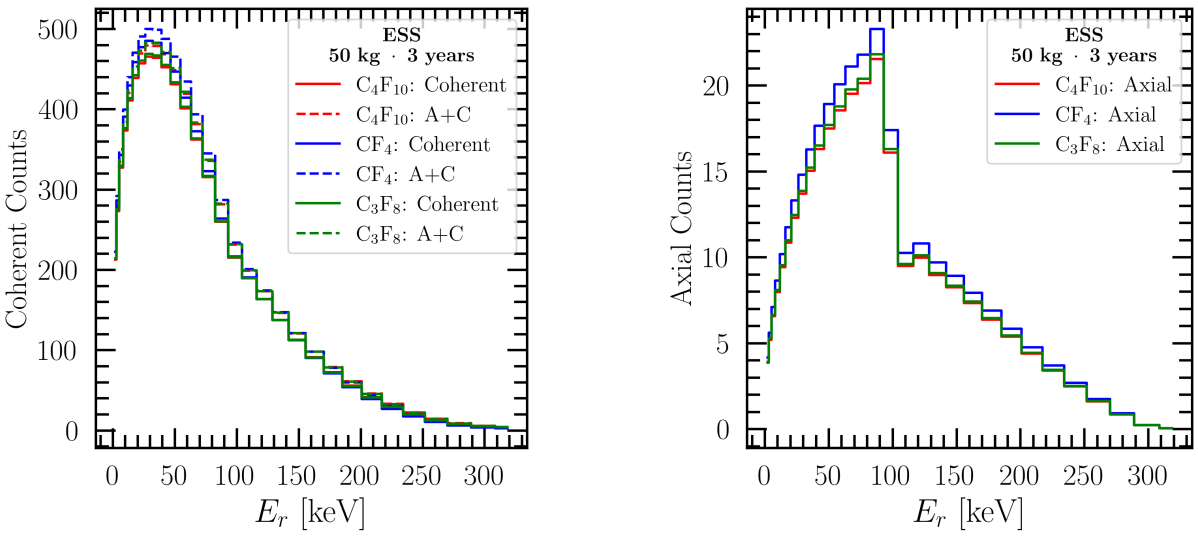

(a) Spectrum event rate coherent events

(b) Spectrum event rate axial events

Figure 4.5: Event-rate spectrum for the coherent (vector) and axial-current contributions to CEνNS are shown for a 50 kg detector exposed to a spallation neutron source neutrino flux over a three year run at an ESS. The setup assumes a baseline of $L = 20$ m, a proton beam power of 1.3 MW, a flat detection acceptance of 80%, and a nuclear recoil energy threshold of 2 keV. Panel (a)Coherent (vector) event-rate spectrum for C_4F_{10}, CF_4 and C_3F_8. Panel (b) Axial-current event-rate spectrum C_4F_{10}, CF_4 and C_3F_8.

A more quantitative understanding is obtained by analyzing the count rates as a function of recoil energy. At low recoil energies (approximately 0–50 keV), the coherent component reaches a maximum of about 500 counts. In contrast, the axial contribution is limited to roughly 15 counts. This produces a suppression factor of approximately 35. Near 100 keV, the coherent component falls below 200 counts. The axial contribution peaks at about 25 counts, reducing the suppression factor to about 8.

This trend is consistent with the observation that the weak-charge form factor, which determines the coherent component, decreases more rapidly with increasing momentum transfer than the axial form factor of ^{19}F (as illustrated by the structure factors in Fig. 4.1). This behavior is not observed in heavier isotopes, where the axial form factor exhibits pronounced peaks.

A suppression factor of approximately 25 provides a global estimate across the entire spectral range [89]. This sharply contrasts with the several orders of magnitude observed for targets such as CsI, NaI, germanium and xeonon. Where axial events number only 3–5 compared to thousands of coherent events. In contrast to heavy nuclear targets, the three fluorine compounds presented in Fig. 4.5 produce axial spectra that are statistically accessible. This effect is especially evident at recoil energies of 50-100 keV, where the spectra are pronounced due to the ^{19}F spin structure functions.

Advancing these results to the experimental stage requires a rigorous evaluation of each compound's practical viability. While all three fluorocarbons are theoretically attractive targets, practical constraints necessitate eliminating two of them. Specifically, CF_4 has been proposed for CEνNS measurements using the νBDX-DRIFT detector [101]. But with only 2 kg active mass is insufficient to achieve the statistical sensitivity required to resolve the axial contribution with precision.

A similar limitation applies to C_4F_{10}, previously utilized by the PICASSO experiment [29] in a traditional bubble chamber configuration with modest active mass, and thus it is excluded from the present analysis. In contrast, C_3F_8 is deployed by the PICO collaboration [30], whose PICO-60 detector operates a bubble chamber containing 52 kg of C_3F_8, with plans to scale to larger volumes [102]. This positions C_3F_8 as a particularly promising target for axial-current CEνNS measurements.

4.3 Sensitivity to the g_A

Although the axial-vector event ratio is relatively small, this subdominant contribution opens access to the calculation of quantities characteristic of the axial current in various processes. Based on these results, the next step is to extract the axial-vector coupling g_A for upcoming COHERENT experiments. In this analysis, we considered only the results for C_3F_8.

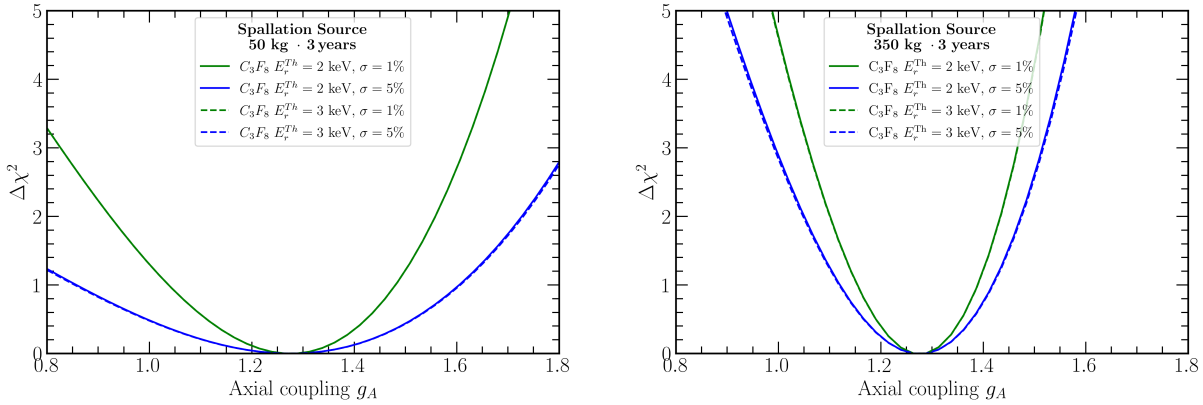

(a) $m_{\text{det}} = 50$ kg **(b)** $m_{\text{det}} = 350$ kg

Figure 4.6: Projected sensitivity to the axial-vector coupling g_A is presented as $\Delta\chi^2$ profiles for a spallation-source experiment using a C_3F_8 detector. Detector masses of 50 kg (Panel (a)) and 350 kg (Panel (b)) are considered under varying recoil-energy thresholds and neutrino flux uncertainties. Green and blue curves represent flux uncertainties of $\sigma_\alpha = 1\%$ and $\sigma_\alpha = 5\%$, respectively. Solid and dashed lines indicate recoil-energy thresholds of $E_r^{\text{th}} = 2$ keV and $E_r^{\text{th}} = 3$ keV, respectively.

Figure 4.6 presents projected sensitivities to g_A, based on previous C_3F_8 data. This analysis uses the χ^2 function, a statistical test that estimates parameters from a dataset using a probability distribution [103]. Forecasted data are simulated under the SM, with g_A ranging from 0.8 to 1.8 while g_A^s is fixed. The following form for χ^2 is used

$$\chi^2 = 2\sum_i \left[N_i^{\text{th}} - N_i^{\text{exp}} + N_i^{\text{exp}} \ln\left(\frac{N_i^{\text{exp}}}{N_i^{\text{th}}}\right)\right] + \left(\frac{\alpha}{\sigma_\alpha}\right)^2 . \tag{4.3.1}$$

Here, N_i^{th} is the theoretical event count per recoil energy bin, calculated using $g_A = 1.27641$ [83] and $g_A^s = -0.085$ [104]. N_i^{exp} is the expected event count for different g_A values. The parameter α reflects neutrino flux uncertainty, while the fractional uncertainty σ_α measures flux normalization precision. This parameter accounts for experimental,

kinematic, and systematic errors.

In this study, we vary three parameters to generate different experimental configurations:

- To characterize the uncertainty, two contrasting scenarios are considered. One is a realistic scenario with fixed uncertainty at $\sigma_\alpha = 5\%$. The other is a more favorable scenario, where the uncertainty is reduced to $\sigma_\alpha = 1\%$, highlighting the range studied.

- Two configurations of recoil-energy thresholds complement these scenarios: one with $E_r^{\text{th}} = 2$ keV and another with $E_r^{\text{th}} = 3$ keV.

- Finally, detector masses are varied to further explore these configurations. The left panel shows a detector mass of 50 kg, reflecting current experiments such as PICO [30]. The right panel presents a future setup with a detector mass of 350 kg. These parameters represent realistic configurations, given the planned construction of a ∼500 kg C_3F_8 detector by the PICO collaboration [102].

Analysis of the curves indicates that neutrino flux uncertainty is the parameter with the greatest influence on the precision of g_{A} extraction. In both panels, the green lines, which represent variations with neutrino flux uncertainty, exhibit significantly narrower $\Delta\chi^2$ wells compared to the blue curve, which corresponds to the baseline scenario. Additionally, the curves representing the recoil-energy thresholds, specifically the solid line for $E_r^{\text{th}} = 2$ keV and the dashed line for $E_r^{\text{th}} = 3$ keV, overlap. This overlap demonstrates that the effect of the recoil-energy threshold is negligible.

Comparing panels (a) and (b) shows that increasing detector mass from 50 kg to 350 kg substantially narrows all perfiles. This improvement exceeds what is achieved by reducing flux uncertainty alone. Detector mass thus emerges as the single most influential parameter in determining g_A through spin-dependent CEνNS measurements.

These results lead to the expected conclusion: the optimal experimental configuration corresponds to the combination of the maximum detector mass and the minimum flux uncertainty. Under these conditions, a measurement of g_A at the $\sim 10\%$ level appears achievable, a precision that would constitute a meaningful constraint on the axial-vector coupling in the neutrino sector. Notably, this target is consistent with the current development plans of the PICO collaboration, which aims to operate a ~ 500 kg C_3F_8 detector, positioning this experiment as a leading candidate for the first precision measurement of the spin-dependent CEνNS cross section.

Chapter 5

Conclusions

In anticipation of future CEνNS measurement programs, a comprehensive study of the subdominant axial current is required for targets with non-zero nuclear ground-state spin. Such analysis enables access to the complete neutrino-nucleus scattering signal and facilitates the investigation of spin-dependent sensitivity to potential new physics. In counting experiments, the axial current signal is significantly suppressed by the dominant vector contribution, leading to its omission in current measurements. A thorough understanding is essential to distinguish whether an observed signal arises from new physics or from previously unaccounted physics effects.

This study examined the principal variables relevant to measuring this subleading yet phenomenologically significant effect. The relative size of the axial contribution to the cross section, and consequently its impact on the total event rate, was quantified. This approach enabled the identification of the physical parameters governing this magnitude. The results demonstrate that, despite suppression effects, the axial contribution can be systematically characterized and experimentally extracted under certain conditions, provided that suitable target materials, neutrino sources, and detector configurations are utilized.

The study begins by examining the structure factors, which are derived from the nuclear response framework developed by Hoferichter, Menéndez, and Schwenk [28]. This framework provides a consistent description of spin-dependent nuclear responses using multipole decomposition of the nuclear current and the nuclear shell model. Building upon these results, the present work extends their application to fully characterize the axial form factor and subsequently evaluates the cross section and event rates in various isotopes relevant to neutrino-nucleus scattering.

The contributions were first examined for heavy targets: ^{133}Cs, ^{127}I, ^{131}Xe, and ^{73}Ge, as these are the most common targets employed in neutrino and dark matter experiments. Even when the neutrino flux is increased using the European Spallation Source and larger mass detectors are considered, the axial signal remains strongly suppressed due to the coherent enhancement of the vector contribution. In contrast, for lighter nuclei such as ^{23}Na and ^{19}F, the behavior differs. Although the axial contribution remains small, the degree of suppression is comparatively less pronounced.

Light nuclei with non-zero spin ground states have been identified as the most promising candidates for isolating the axial signal. In particular, ^{19}F emerges as the optimal target due to its large unpaired proton spin expectation, which results in a less restrictive

axial form factor and consequently reduced suppression of this contribution.

Fluorine-based compounds emerge as the most favorable targets for axial-current extraction in CEνNS: the coherent-to-axial suppression factor reaches only ~ 25 across the full spectral range, in stark contrast to targets such as CsI or NaI, where axial events number merely 3 to 5 against thousands of coherent events [89]. Among the three fluorocarbon candidates, practical experimental considerations single out C_3F_8 as the most viable option, supported by the PICO collaboration [30, 102], whose planned large-scale detectors make this compound not only physically optimal but also experimentally accessible for precision axial-current measurements.

An application of this analysis is demonstrated through the development of a forecast study for axial-current measurements, which evaluates the achievable precision in extracting the axial-vector coupling g_A under various experimental configurations. The results suggest that, in a realistic experimental setup employing a 350 kg C_3F_8 detector, a nuclear recoil threshold of 2 keV, and a 1% neutrino flux uncertainty, g_A can be extracted with approximately 10% precision. While measurements of CEνNS are less precise than those obtained from cold neutron experiments, they provide a complementary determination of g_A relative to traditional approaches and yield additional insights into the axial structure of weak interactions.

Despite the results obtained, this works present inherent limitations. In particular, the determination of the axial contribution is based on nuclear structure calculations considering the shell model and harmonic oscillator approximations, which introduce uncertainties for more complex nuclear configurations, this is translated as theoretical uncertainties in the spin-dependent form factors.

In addition, our results of the sensitivity analysis demands a exigent experimental configuration such as small range of nuclear recoil energy threshold, large detector masses available, and low value for uncertainty in the neutrino flux normalization, in the same line in a realistic experimental set; beam neutron backgrounds, electronic noise, and detector systematic uncertainties, would need to be modelled in detail. Overall, theoretical developments more precise will allow for a reduction in uncertainties in the results.

However, the results in this work provide a clear guide for future experimental and theoretical efforts. Where next-generation detectors assuming targets of light isotopes and non-spin zero ground states, with lower recoil-energy thresholds, larger target masses, and improved control of systematic uncertainties will be crucial to enhance the sensitivity to the axial-current contribution.

A particularly promising direction for future research is the extension of spin-dependent responses within frameworks beyond the Standard Model. In contrast to the Standard Model, where the axial contribution is subleading and tightly constrained, beyond Standard Model scenarios may introduce enhanced or qualitatively different couplings to nuclear spin, thereby modifying both the magnitude and momentum dependence of the spin-dependent structure factors. Additionally, extending the analysis to reactor neutrino sources, motivated by the recent detection of reactor-neutrino CEνNS by the CONUS+ experiment [82] and the emerging CONNIE collaboration [80], would complement the spallation-source results presented here. Finally, future work could focus on the experimental extraction of the axial contribution, given that in the present study this contribu-

tion is fully determined theoretically.

In this context, a precise measurement of the axial-current contribution is essential for a complete description of neutrino-nucleus scattering at low energies, and would establish CEνNS as a powerful probe of spin-dependent new physics that remains inaccessible in standard coherent analyses. The theoretical framework developed in this work provides the necessary foundation for such measurements, and the identification of C_3F_8 as the optimal experimental target opens a concrete and near-term path toward their realization.

Chapter 6

Appendix

A Infinitesimal Gauge Transformation of the Gauge Field

We start from the infinitesimal gauge transformation

$$U(\epsilon(x)) = 1 + i\,\epsilon(x) \cdot L \ , \tag{A.1}$$

and consider the transformation of the gauge field

$$A_\mu \cdot L \ \longrightarrow \ A'_\mu \cdot L = (1 + i\,\epsilon \cdot L)\left(A_\mu \cdot L - \frac{i}{g}\partial_\mu\right)(1 - i\,\epsilon \cdot L) \ . \tag{A.2}$$

We expand this expression up to first order in ϵ.

First term

Consider first the transformation of $A_\mu \cdot L$:

$$\begin{aligned}(1 + i\,\epsilon \cdot L)(A_\mu \cdot L)(1 - i\,\epsilon \cdot L) &= [A_\mu \cdot L + i(\epsilon \cdot L)(A_\mu \cdot L)]\,(1 - i\,\epsilon \cdot L) \\ &= A_\mu \cdot L + i(\epsilon \cdot L)(A_\mu \cdot L) - i(A_\mu \cdot L)(\epsilon \cdot L) + \mathcal{O}(\epsilon^2) \ .\end{aligned} \tag{A.3}$$

Neglecting terms of order $\mathcal{O}(\epsilon^2)$, we obtain

$$(1 + i\,\epsilon \cdot L)(A_\mu \cdot L)(1 - i\,\epsilon \cdot L) = A_\mu \cdot L + i[\epsilon \cdot L,\ A_\mu \cdot L] \ . \tag{A.4}$$

Second term

We now consider the derivative term:

$$(1 + i\,\epsilon \cdot L)\left(-\frac{i}{g}\partial_\mu\right)(1 - i\,\epsilon \cdot L) \ . \tag{A.5}$$

The derivative acts on the space-time dependent parameter $\epsilon(x)$, while the generators L_a are constant:

$$\partial_\mu(1 - i\,\epsilon \cdot L) = -i(\partial_\mu\epsilon) \cdot L \ . \tag{A.6}$$

Thus,

$$(1 + i\,\epsilon \cdot L)\left(-\frac{i}{g}\partial_\mu\right)(1 - i\,\epsilon \cdot L) = -\frac{i}{g}(1 + i\,\epsilon \cdot L)\,[-i(\partial_\mu \epsilon) \cdot L] \\ = -\frac{1}{g}(\partial_\mu \epsilon) \cdot L + \mathcal{O}(\epsilon^2)\ . \tag{A.7}$$

Again, higher-order terms are neglected.

Final result

Collecting both contributions, the transformed gauge field reads

$$A'_\mu \cdot L = A_\mu \cdot L + i[\epsilon \cdot L,\ A_\mu \cdot L] - \frac{1}{g}(\partial_\mu \epsilon) \cdot L\ . \tag{A.8}$$

Therefore, the infinitesimal variation of the gauge field is

$$\boxed{\delta A_\mu \cdot L = i[\epsilon \cdot L,\ A_\mu \cdot L] - \frac{1}{g}\,\partial_\mu \epsilon \cdot L}\ . \tag{A.9}$$

B Derivation of the Gauge Field Variation

Starting from Eq. (A.9), which is a matrix equation in the Lie algebra,

$$\sum_{a=1}^{N} \delta A^a_\mu\, L_a = -\sum_{a,b,c=1}^{N} f_{abc}\,\epsilon_a\, A^b_\mu\, L_c - \frac{1}{g}\sum_{a=1}^{N}(\partial_\mu \epsilon_a)\, L_a\ , \tag{B.1}$$

we aim to extract the variation of the gauge field components δA^a_μ.

The generators L_a form an orthonormal basis of the Lie algebra, satisfying the relation

$$\mathrm{Tr}(L_a L_b) = \frac{1}{2}\,\delta_{ab}\ . \tag{B.2}$$

To isolate the coefficient multiplying each generator, we project Eq. (A.9) onto a fixed generator L_d by multiplying both sides by L_d and taking the trace:

$$\mathrm{Tr}\left[L_d \sum_{a=1}^{N} \delta A^a_\mu\, L_a\right] = \mathrm{Tr}\left[L_d \left(-\sum_{a,b,c=1}^{N} f_{abc}\,\epsilon_a\, A^b_\mu\, L_c - \frac{1}{g}\sum_{a=1}^{N}(\partial_\mu \epsilon_a)\, L_a\right)\right]\ . \tag{B.3}$$

Using the linearity of the trace, the left-hand side becomes

$$\sum_{a=1}^{N} \delta A^a_\mu\ \mathrm{Tr}(L_d L_a) = \sum_{a=1}^{N} \delta A^a_\mu \left(\frac{1}{2}\delta_{da}\right) = \frac{1}{2}\,\delta A^d_\mu\ . \tag{B.4}$$

The first term on the right-hand side gives

$$-\sum_{a,b,c=1}^{N} f_{abc}\,\epsilon_a\, A^b_\mu\ \mathrm{Tr}(L_d L_c) = -\frac{1}{2}\sum_{a,b=1}^{N} f_{abd}\,\epsilon_a\, A^b_\mu\ , \tag{B.5}$$

while the second term yields

$$-\frac{1}{g}\sum_{a=1}^{N}(\partial_\mu\epsilon_a)\ \mathrm{Tr}(L_d L_a) = -\frac{1}{2g}\,\partial_\mu\epsilon_d\ . \tag{B.6}$$

Collecting all contributions, we obtain

$$\delta A^d_\mu = -\sum_{a,b=1}^{N} f_{abd}\,\epsilon_a\,A^b_\mu - \frac{1}{g}\,\partial_\mu\epsilon_d\ . \tag{B.7}$$

C Useful Identities and Gauge Field Transformations

In this appendix we present some identities and derivations that are used throughout the discussion of non-Abelian gauge theories. In particular, we derive an important identity involving the derivative of the inverse of a group element and show the equivalence between two common forms of the gauge field transformation.

C.1 Derivative of the Inverse Group Element

Let $U(x)$ be an element of a Lie group G, depending smoothly on the spacetime coordinates x^μ, with inverse $U^{-1}(x)$. By definition,

$$U(x)\,U^{-1}(x) = \mathbb{I}\ . \tag{C.1}$$

Taking the spacetime derivative of both sides, we obtain

$$\partial_\mu\big(UU^{-1}\big) = \partial_\mu\mathbb{I} = 0\ . \tag{C.2}$$

Using the product rule, this yields

$$(\partial_\mu U)\,U^{-1} + U\,(\partial_\mu U^{-1}) = 0\ . \tag{C.3}$$

Multiplying this expression from the left by U^{-1}, we find

$$U^{-1}(\partial_\mu U)U^{-1} + \partial_\mu U^{-1} = 0\ . \tag{C.4}$$

Solving for the derivative of the inverse, we arrive at the identity

$$\boxed{\partial_\mu U^{-1} = -\,U^{-1}(\partial_\mu U)\,U^{-1}\ .} \tag{C.5}$$

This identity plays a crucial role in the derivation of the transformation law of the non-Abelian gauge field under local gauge transformations.

C.2 Equivalence of Gauge Field Transformation Laws

Consider a non-Abelian gauge theory with gauge field

$$A_\mu(x) = A^a_\mu(x)L^a\ , \tag{C.6}$$

where L^a are the generators of the Lie algebra of the gauge group. Under a local gauge transformation

$$U(x) = e^{i\theta^a(x)L^a}\ , \tag{C.7}$$

the gauge field is often written to transform as

$$A'_\mu \cdot L = U(x)\left(A_\mu \cdot L - \frac{i}{g}\,\partial_\mu\right) U^{-1}(x)\ . \tag{C.8}$$

Expanding this expression explicitly, we obtain

$$A'_\mu = UA_\mu U^{-1} - \frac{i}{g}\,U(\partial_\mu U^{-1})\ . \tag{C.9}$$

Using the identity derived in Eq. (C.5), the second term becomes

$$-\frac{i}{g}\,U(\partial_\mu U^{-1}) = \frac{i}{g}(\partial_\mu U)U^{-1}\ . \tag{C.10}$$

Therefore, the gauge field transformation can be written as

$$\boxed{A'_\mu = UA_\mu U^{-1} + \frac{i}{g}(\partial_\mu U)U^{-1}\ .} \tag{C.11}$$

D Infinitesimal Gauge Transformation of b_μ

In this appendix we present explicitly the derivation of the infinitesimal gauge transformation of a non-Abelian gauge field.

D.1 Finite Gauge Transformation

The gauge field $B_\mu = B^a_\mu \tau^a$ transforms under a local gauge transformation $G(x)$ as

$$B'_\mu = GB_\mu G^{-1} + \frac{i}{g}(\partial_\mu G)G^{-1}\ , \tag{D.1}$$

where g is the gauge coupling constant and τ^a are the generators of the gauge group (for SU(2), the Pauli matrices).

D.2 Infinitesimal Transformation

For an infinitesimal transformation, the group element is written as

$$G(x) = 1 + \frac{i}{2}\,\tau\cdot\alpha(x), \qquad G^{-1}(x) = 1 - \frac{i}{2}\,\tau\cdot\alpha(x)\ , \tag{D.2}$$

where terms of order $\mathcal{O}(\alpha^2)$ have been neglected.

First Term: $GB_\mu G^{-1}$

Substituting Eq. (D.2) into the first term of Eq. (D.1), we obtain

$$\begin{aligned} GB_\mu G^{-1} &= \left(1 + \frac{i}{2}\,\tau\cdot\alpha\right) B_\mu \left(1 - \frac{i}{2}\,\tau\cdot\alpha\right) \\ &= B_\mu + \frac{i}{2}(\tau\cdot\alpha)B_\mu - \frac{i}{2}B_\mu(\tau\cdot\alpha) + \mathcal{O}(\alpha^2)\ . \end{aligned} \tag{D.3}$$

Second Term: $(\partial_\mu G)G^{-1}$

The derivative of the group element is

$$\partial_\mu G = \frac{i}{2}\,\tau\cdot(\partial_\mu\alpha)\ . \tag{D.4}$$

Multiplying by G^{-1} and keeping only linear terms, we find

$$\begin{aligned}(\partial_\mu G)G^{-1} &= \frac{i}{2}\,\tau\cdot(\partial_\mu\alpha)\left(1-\frac{i}{2}\,\tau\cdot\alpha\right)\\ &= \frac{i}{2}\,\tau\cdot(\partial_\mu\alpha)+\mathcal{O}(\alpha^2)\ .\end{aligned} \tag{D.5}$$

Therefore,

$$\frac{i}{g}(\partial_\mu G)G^{-1} = -\frac{1}{2g}\,\tau\cdot(\partial_\mu\alpha)\ . \tag{D.6}$$

Combining Eqs. (D.3) and (D.6), the infinitesimal gauge transformation of the gauge field is given by

$$B'_\mu = B_\mu + \frac{i}{2}(\tau\cdot\alpha)B_\mu - \frac{i}{2}B_\mu(\tau\cdot\alpha) + \mathcal{O}(\alpha^2) - \frac{1}{2g}\,\tau\cdot(\partial_\mu\alpha)\ .$$

This result explicitly displays the homogeneous (commutator) and inhomogeneous (derivative) contributions characteristic of non-Abelian gauge transformations. Neglecting the larger order terms and use Lie algebra Eq. (2.1.17), it is obtain for gauge fields:

$$\begin{aligned}\boldsymbol{\tau}\cdot\boldsymbol{b'_\mu} &= \boldsymbol{\tau}\cdot\boldsymbol{b_\mu} + i\,(\boldsymbol{\tau}\cdot\boldsymbol{\alpha}\ \boldsymbol{\tau}\cdot\boldsymbol{b_\mu} - \boldsymbol{\tau}\cdot\boldsymbol{b_\mu}\ \boldsymbol{\tau}\cdot\boldsymbol{\alpha}) - \frac{1}{g}\partial_\mu(\boldsymbol{\tau}\cdot\boldsymbol{\alpha})\\ &= \boldsymbol{\tau}\cdot\boldsymbol{b_\mu} + \alpha\times\boldsymbol{b}_\mu\cdot\tau - \frac{1}{g}\partial_\mu(\boldsymbol{\tau}\cdot\boldsymbol{\alpha})\ ,\end{aligned}$$

because the three isospin components of the gauge field are linearly independent, we have as the transformation law for infinitesimal gauge transformations:

$$\boldsymbol{b}'_\mu = \boldsymbol{b}_\mu - \boldsymbol{\alpha}\times\boldsymbol{b}_\mu - \frac{1}{g}\partial_\mu\boldsymbol{\alpha}\ . \tag{D.7}$$

As a result get the variation gauge vector under SU(2), and it is equivalent to Eq. (2.1.9).

E Gauge invariance of the free Lagrangian

E.1 Lepton

The free leptonic Lagrangian (disgard mass term) is given by

$$\mathcal{L}^{\rm lep}_{\rm free} = \bar{\ell}_R\, i\gamma^\mu\partial_\mu\ell_R + \bar{\psi}^{\rm lep}_{iL}\, i\gamma^\mu\partial_\mu\psi^{\rm lep}_{iL}\ , \tag{E.1}$$

where the left-handed lepton doublets are defined as

$$\psi^{\rm lep}_{iL} = \begin{pmatrix}\nu'_{iL}\\ \ell'_{iL}\end{pmatrix}, \qquad i = e,\mu,\tau\ . \tag{E.2}$$

and ℓ_R is a rigth handed singlet.

Local gauge invariance under the group $\mathrm{SU}(2)_L \times \mathrm{U}(1)_Y$ is ensured by replacing the ordinary derivative with the covariant derivative,

$$\partial_\mu \longrightarrow D_\mu. \tag{E.3}$$

For the right-handed charged leptons, which are singlets under $\mathrm{SU}(2)_L$, the covariant derivative reads

$$D_\mu \ell_R = \left(\partial_\mu + i g' \frac{Y_R^{\mathrm{lep}}}{2} B_\mu \right) \ell_R \ . \tag{E.4}$$

For the left-handed lepton doublets, transforming as doublets of $\mathrm{SU}(2)_L$, one has

$$D_\mu \psi_{iL}^{\mathrm{lep}} = \left(\partial_\mu + i g \frac{\tau^a}{2} A_\mu^a + i g' \frac{Y_L^{\mathrm{lep}}}{2} B_\mu \right) \psi_{iL}^{\mathrm{lep}} \ . \tag{E.5}$$

Substituting the covariant derivatives into the free Lagrangian, the leptonic Lagrangian including gauge interactions becomes

$$\begin{aligned} \mathcal{L}^{\mathrm{lep}} &= \bar{\ell}_R \, i\gamma^\mu \partial_\mu \ell_R + \bar{\psi}_{iL}^{\mathrm{lep}} \, i\gamma^\mu \partial_\mu \psi_{iL}^{\mathrm{lep}} \\ &\quad - g' \frac{Y_R^{\mathrm{lep}}}{2} \, \bar{\ell}_R \gamma^\mu B_\mu \ell_R - g \, \bar{\psi}_{iL}^{\mathrm{lep}} \gamma^\mu \frac{\tau^a}{2} A_\mu^a \psi_{iL}^{\mathrm{lep}} - g' \, \frac{Y_L^{\mathrm{lep}}}{2} \, \bar{\psi}_{iL}^{\mathrm{lep}} \gamma^\mu B_\mu \psi_{iL}^{\mathrm{lep}} \qquad \text{(E.6)} \\ &= \mathcal{L}_{free}^{lep} - g' \, \frac{Y_R^{\mathrm{lep}}}{2} \, \bar{\ell}_R \gamma^\mu B_\mu \ell_R - g \, \bar{\psi}_{iL}^{\mathrm{lep}} \gamma^\mu \frac{\tau^a}{2} A_\mu^a \psi_{iL}^{\mathrm{lep}} - g' \, \frac{Y_L^{\mathrm{lep}}}{2} \, \bar{\psi}_{iL}^{\mathrm{lep}} \gamma^\mu B_\mu \psi_{iL}^{\mathrm{lep}} \ . \qquad \text{(E.7)} \end{aligned}$$

Using the Gell-Mann–Nishijima relation

$$Q = T_3 + \frac{Y}{2} \ ,$$

the hypercharge assignments for the leptonic sector are fixed to be

$$Y_L^{\mathrm{lep}} = -1 \ , \qquad Y_R^{\mathrm{lep}} = -2 \ . \tag{E.8}$$

With it obtain the final lepton Lagrangian invariant under $\mathrm{SU}(2)_L \times \mathrm{U}(1)_Y$:

$$\boxed{\mathcal{L}^{\mathrm{lep}} = \mathcal{L}_{\mathrm{free}}^{\mathrm{lep}} + g' \, \bar{l}_R \gamma^\mu B_\mu l_R - g \, \bar{\psi}_{iL}^{\mathrm{lep}} \gamma^\mu \frac{\tau^a}{2} A_\mu^a \psi_{iL}^{\mathrm{lep}} + g' \, \frac{1}{2} \, \bar{\psi}_{iL}^{\mathrm{lep}} \gamma^\mu B_\mu \psi_{iL}^{\mathrm{lep}} \ .} \tag{E.9}$$

E.2 Quarks

The free quark Lagrangian (discarding mass terms) is given by

$$\mathcal{L}_{\mathrm{free}}^q = \bar{u}_{iR} \, i\gamma^\mu \partial_\mu u_{iR} + \bar{d}_{iR} \, i\gamma^\mu \partial_\mu d_{iR} + \bar{\psi}_{iL}^q \, i\gamma^\mu \partial_\mu \psi_{iL}^q \ , \tag{E.10}$$

where the left-handed quark doublets are defined as

$$\psi_{iL}^q = \begin{pmatrix} u'_{iL} \\ d'_{iL} \end{pmatrix} \ , \qquad i = 1, 2, 3 \ , \tag{E.11}$$

and u_{iR} and d_{iR} are right-handed singlets under $\mathrm{SU}(2)_L$. For the right-handed up-type quarks, singlets under $\mathrm{SU}(2)_L$, the covariant derivative reads

$$D_\mu u_{iR} = \left(\partial_\mu + ig' \frac{Y_R^{\mathrm{up}}}{2} B_\mu\right) u_{iR} \ , \tag{E.12}$$

while for the right-handed down-type quarks one has

$$D_\mu d_{iR} = \left(\partial_\mu + ig' \frac{Y_R^{\mathrm{down}}}{2} B_\mu\right) d_{iR} \ . \tag{E.13}$$

For the left-handed quark doublets, transforming as doublets of $\mathrm{SU}(2)_L$, the covariant derivative is

$$D_\mu \psi_{iL}^q = \left(\partial_\mu + ig \frac{\tau^a}{2} A_\mu^a + ig' \frac{Y_L^q}{2} B_\mu\right) \psi_{iL}^q \ . \tag{E.14}$$

Substituting the covariant derivatives into the free Lagrangian, the quark Lagrangian including gauge interactions becomes

$$\begin{aligned} \mathcal{L}^q = \mathcal{L}^q_{\mathrm{free}} &- g' \frac{Y_R^{\mathrm{up}}}{2} \bar{u}_{iR} \gamma^\mu B_\mu u_{iR} - g' \frac{Y_R^{\mathrm{down}}}{2} \bar{d}_{iR} \gamma^\mu B_\mu d_{iR} \\ &- g \, \bar{\psi}_{iL}^q \gamma^\mu \frac{\tau^a}{2} A_\mu^a \psi_{iL}^q - g' \frac{Y_L^q}{2} \bar{\psi}_{iL}^q \gamma^\mu B_\mu \psi_{iL}^q \ . \end{aligned} \tag{E.15}$$

The hypercharge values for the quarks are

$$Y_L^q = \frac{1}{3}, \qquad Y_R^{\mathrm{up}} = \frac{4}{3}, \qquad Y_R^{\mathrm{down}} = -\frac{2}{3} \ . \tag{E.16}$$

With these values, the final quark Lagrangian invariant under $\mathrm{SU}(2)_L \times \mathrm{U}(1)_Y$ reads

$$\begin{aligned} \mathcal{L}_I^q = \mathcal{L}^q_{\mathrm{free}} &- \frac{2}{3} g' \, \bar{u}_{iR} \gamma^\mu B_\mu u_{iR} + \frac{1}{3} g' \, \bar{d}_{iR} \gamma^\mu B_\mu d_{iR} \\ &- \frac{1}{2} \bar{\psi}_{iL}^q \left(g \gamma^\mu \tau^a A_\mu^a - \frac{1}{3} g' \gamma^\mu B_\mu \right) \psi_{iL}^q \ . \end{aligned} \tag{E.17}$$

F Detailed Derivation of the Neutral Current Lagrangian

In this appendix we present the explicit algebraic derivation of the neutral current interaction in the lepton sector of the electroweak theory, starting from the gauge–fermion couplings written in terms of the physical fields Z_μ and A_μ.

For convenience, we introduce the standard shorthand notation for the Weinberg angle,

$$s_{\mathrm{W}} \equiv \sin\theta_{\mathrm{W}} \ , \qquad c_{\mathrm{W}} \equiv \cos\theta_{\mathrm{W}} \ . \tag{F.1}$$

The neutral current interaction Lagrangian for leptons can be written as

$$\begin{aligned} \mathcal{L}_{I,L}^{(\mathrm{NC})} = -\frac{1}{2} \Big\{ & \bar{\nu}_{eL} \Big[(g \, c_{\mathrm{W}} + g' \, s_{\mathrm{W}}) \not{Z} + (g \, s_{\mathrm{W}} - g' \, c_{\mathrm{W}}) \not{A} \Big] \nu_{eL} \\ & - \bar{e}_L \Big[(g \, c_{\mathrm{W}} - g' \, s_{\mathrm{W}}) \not{Z} + (g \, s_{\mathrm{W}} + g' \, c_{\mathrm{W}}) \not{A} \Big] e_L \end{aligned}$$

$$- 2g\,\bar{e}_R\Big[- s_{\rm W}\,\not{Z} + c_{\rm W}\,\not{A}\Big] e_R \Bigg\} \ . \tag{F.2}$$

The electroweak gauge couplings satisfy the well-known relation

$$g\,s_{\rm W} = g'\,c_{\rm W} \quad \rightarrow \quad g' = g\frac{s_{\rm W}}{c_{\rm W}} \quad \text{and} \quad \tan\theta_{\rm W} = \frac{g'}{g} \ , \tag{F.3}$$

with it, replace in the Lagrangian:

$$\mathcal{L}_{I,L}^{(\rm NC)} = -\frac{1}{2}\Bigg\{ \bar{\nu}_{eL}\left(g\,c_{\rm W} + g\,\frac{s_{\rm W}^2}{c_{\rm W}} \right) \not{Z}\,\nu_{eL} \tag{F.4}$$

$$- \bar{e}_L\left[\left(g\,c_{\rm W} - g\,\frac{s_{\rm W}^2}{c_{\rm W}} \right) \not{Z} + \left(g\,s_{\rm W} + g\,\frac{s_{\rm W}c_{\rm W}}{c_{\rm W}} \right) \not{A} \right] e_L \tag{F.5}$$

$$- 2g\,\bar{e}_R\left[-\frac{s_{\rm W}^2}{c_{\rm W}}\not{Z} + \frac{c_{\rm W}s_{\rm W}}{c_{\rm W}}\not{A} \right] e_R \Bigg\} \tag{F.6}$$

$$= -\frac{g}{2c_{\rm W}}\Bigg\{ \bar{\nu}_{eL}\not{Z}\nu_{eL} - \bar{e}_L\left[\left(c_{\rm W}^2 - s_{\rm W}^2\right)\not{Z} + 2s_{\rm W}c_{\rm W}\not{A} \right] e_L - 2\bar{e}_R\left[-s_{\rm W}^2\not{Z} \right] e_R \Bigg\} \tag{F.7}$$

$$+ g\bar{e}_R s_{\rm W}\not{A} e_R \ . \tag{F.8}$$

Use trigonometric identities and finally obtain:

$$\boxed{\mathcal{L}_{I,L}^{(\rm NC)} = -\frac{g}{2c_{\rm W}}\left\{ \bar{\nu}_{eL}\not{Z}\nu_{eL} - \left(1 - 2s_{\rm W}^2\right)\bar{e}_L\not{Z}e_L + 2s_{\rm W}^2\bar{e}_R\not{Z}e_R \right\} + g s_{\rm W}\,\bar{e}\not{A}e} \tag{F.9}$$

G Notation Nuclear Physiscs

As we know in particle physics is usual use the natural units based in use only energy dimension and with it $c = h = 1$, and to use the notation of cuadrivector like $a^\mu = (a^0, \vec{a})$. However,this section it is based in "THEORETICAL NUCLEAR AND SUBNUCLEAR PHYSICS" of John Dirk Walecka [31] in wich he present the next table comparative for convertions that he use :

Bjorken and Drell [105]		Present text [31]
$g_{\mu\nu} = \begin{pmatrix} 1 & 0 & 0 & 0 \\ 0 & -1 & 0 & 0 \\ 0 & 0 & -1 & 0 \\ 0 & 0 & 0 & -1 \end{pmatrix}$	$\leftrightarrow$	$\delta_{\mu\nu}$
$a^\mu = (a^0, \vec{a})$	$\leftrightarrow$	$a_\mu = (a_1, a_2, a_3, a_4) = (\vec{a}, ia_0)$
$a_\mu b^\mu = g_{\mu\nu} a^\mu b^\nu = a^0 b^0 - \vec{a} \cdot \vec{b}$	$\leftrightarrow$	$a_\mu b_\mu = \vec{a} \cdot \vec{b} - a_0 b_0$
$x^\mu = (t, \vec{x})$	$\leftrightarrow$	$x_\mu = (\vec{x}, it)$
$x_\mu = g_{\mu\nu} x^\nu = (t, -\vec{x})$	$\leftrightarrow$	$x^\mu \equiv x_\mu$
$\partial_\mu = \frac{\partial}{\partial x^\mu} = \left(\frac{\partial}{\partial t}, \vec{\nabla}\right)$	$\leftrightarrow$	$\frac{\partial}{\partial x_\mu} = \left(\vec{\nabla}, \frac{\partial}{i\partial t}\right)$
$\gamma^\mu = (\beta, \beta\vec{\alpha})$	$\leftrightarrow$	$\gamma_\mu = (i\vec{\alpha}\beta, \beta)$
$\gamma^\mu \gamma^\nu + \gamma^\nu \gamma^\mu = 2g^{\mu\nu}$	$\leftrightarrow$	$\gamma_\mu \gamma_\nu + \gamma_\nu \gamma_\mu = 2\delta_{\mu\nu}$
$\gamma^{\mu\dagger} = \gamma^0 \gamma^\mu \gamma^0$	$\leftrightarrow$	$\gamma_\mu^\dagger = \gamma_\mu$
$(i\gamma^\mu \partial_\mu - M)\psi = 0$	$\leftrightarrow$	$(\gamma_\mu \partial/\partial x_\mu + M)\psi = 0$
$(k_\mu \gamma^\mu - M)u(k) = 0$	$\leftrightarrow$	$(i\gamma_\mu k_\mu + M)u(k) = 0$
$\gamma^5 = i\gamma^0\gamma^1\gamma^2\gamma^3$	$\leftrightarrow$	$\gamma_5 = \gamma_1\gamma_2\gamma_3\gamma_4$
$\sigma^{\mu\nu} = \frac{i}{2}[\gamma^\mu, \gamma^\nu]$	$\leftrightarrow$	$\sigma_{\mu\nu} = \frac{1}{2i}[\gamma_\mu, \gamma_\nu]$

Note: $g_{\mu\nu} = g^{\mu\nu}$.

Table 1: Convention comparison table ($\hbar = c = 1$).

So we follow the notation of Walecka in Section 2.3.

H Calculation of $\langle\ k_2\ |\ j_\mu^{\mathbf{lep}}|\ k_1\ \rangle$

Begin with lepton sector since the current it is SM, shows in previous sections. For the representation of the fields we use second quantization, in which particles are described by quantum field operators acting on a Fock space and refers to the integer of excitations of each modes, allowing for the creation and annihilation of particles from to creation and annihilation operators for each moment, written as[106],

$$\psi(\boldsymbol{x}) = \int \frac{d^3k}{(2\pi)^3} \frac{1}{\sqrt{2E_{\boldsymbol{k}}}} \sum_s \left(a_{\boldsymbol{k}}^s u^s(k) e^{-i\boldsymbol{k}\cdot\boldsymbol{x}} + b_{\boldsymbol{k}}^{s\dagger} v^s(k) e^{i\boldsymbol{k}\cdot\boldsymbol{x}} \right) , \tag{H.1}$$

$$\bar{\psi}(\boldsymbol{x}) = \int \frac{d^3k}{(2\pi)^3} \frac{1}{\sqrt{2E_{\boldsymbol{k}}}} \sum_s \left(a_{\boldsymbol{k}}^{\dagger s} \bar{u}^s(k) e^{-i\boldsymbol{k}\cdot\boldsymbol{x}} + b_{\boldsymbol{k}}^s \bar{v}^s(k) e^{-i\boldsymbol{k}\cdot\boldsymbol{x}} \right) . \tag{H.2}$$

In its expression, $u^s(\boldsymbol{k})e^{i\boldsymbol{k}\cdot\boldsymbol{x}}$ are eigenfunctions of the Dirac Hamiltonian with eigenvalues $E_{\boldsymbol{p}}$, similarly to the functions $v^s(k)e^{-i\boldsymbol{k}\cdot\boldsymbol{x}}$ (or equivalently $v^s(-\boldsymbol{k})e^{+i\boldsymbol{k}\cdot\boldsymbol{x}}$) are eigenfunctions of the Dirac Hamiltonian with eigenvalues $-E_{\boldsymbol{p}}$ and are described in the Heisenberg picture, the index s corresponds to helicity or spin.

Also $a_{\boldsymbol{k}}^s$ operator destroys a fermion using the fact that of vaccum $|0\rangle$ is defined to be

the state such that

$$a_k^s\,|0\rangle = b_k^s\,|0\rangle = 0\ , \tag{H.3}$$

while $a^{s\dagger}$ creates fermions, and $b^\dagger$ creates an antifermion by,

$$|\boldsymbol{k}, s\rangle \equiv \sqrt{2E_K}\ a_{\boldsymbol{k}}^{s\dagger}\,|0\rangle\ , \tag{H.4}$$

and this operators obey the anticonmutation rules:

$$\left\{a_k^r, a_p^{s\dagger}\right\} \;=\; \left\{b_k^r, a_p^{b\dagger}\right\} \;=\; (2\pi)^3\delta^{(3)}(\boldsymbol{k}-\boldsymbol{p})\delta^{rs}\ , \tag{H.5}$$

based on the above, the current lepton matrix is calculated.

We knows $j_\mu^{\rm lep}(\boldsymbol{x}) = \bar\nu(\boldsymbol{x})\gamma_\mu(1+\gamma_5)\nu(\boldsymbol{x})$, so for right handed of matrix element is, using the Eq. (H.1) for described $\nu(\boldsymbol{x})$, and we need create a fermion so projected in the state Eq. (H.4) we obtain:

$$\begin{aligned}\nu(\vec{x})\,|k_1,s\rangle &= \int \frac{d^3p}{(2\pi)^3}\frac{1}{\sqrt{2E_p}}\sum_r\left[a_r(p)\,u_r(p)\,e^{-i\vec{p}\cdot\vec{x}}\right]\sqrt{2E_{k_1}}\,a_s^\dagger(k_1)\,|0\rangle \\ &= \int \frac{d^3p}{(2\pi)^3}\frac{\sqrt{2E_{k_1}}}{\sqrt{2E_p}}\sum_r\left[u_r(p)\,e^{-i\vec{p}\cdot\vec{x}}a_r(p)\ a_s^\dagger(k_1)\,|0\rangle\right]\ ,\end{aligned} \tag{H.6}$$

we use anticommutation rules Eq. (H.5)

$$\begin{aligned}a_r(p)\,a_s^\dagger(k_1)\,|0\rangle &= \left[(2\pi)^3\delta^{(3)}(p-k_1)\,\delta^{rs} - a_s^\dagger(k_1)\,a_r(p)\right]|0\rangle \\ &= (2\pi)^3\delta^{(3)}(p-k_1)\,\delta^{rs}\,|0\rangle\end{aligned} \tag{H.7}$$

$$\begin{aligned}\Rightarrow \nu(\vec{x})\,|k_1,s\rangle &= \int \frac{d^3p}{(2\pi)^3}\frac{\sqrt{2E_{k_1}}}{\sqrt{2E_p}}\sum_r\left[u_r(p)\,e^{-i\vec{p}\cdot\vec{x}}\,(2\pi)^3\delta^{(3)}(p-k_1)\,\delta^{rs}\,|0\rangle\right] \\ &= u_s(k_1)\,e^{-i\vec{k}_1\cdot\vec{x}}\,|0\rangle\ .\end{aligned} \tag{H.8}$$

Likewise for the final state, for the form of current we need:

$$\begin{aligned}\langle k_2,s'|\bar\nu &= \int \frac{d^3q}{(2\pi)^3}\frac{1}{\sqrt{2E_q}}\sum_{r'}\left[a_{r'}^\dagger(q)\,\bar u_{r'}(q)\,e^{i\vec{q}\cdot\vec{x}}\right]\langle 0|\sqrt{2E_{k_2}}\,a_{s'}(k_2) \\ &= \int \frac{d^3q}{(2\pi)^3}\frac{\sqrt{2E_{k_2}}}{\sqrt{2E_q}}\sum_{r'}\left[\langle 0|a_{s'}(k_2)a_{r'}^\dagger(q)\bar u_{r'}(q)e^{i\vec{q}\cdot\vec{x}}\right]\end{aligned} \tag{H.9}$$

Use the anticommutation rules:

$$\begin{aligned}\Rightarrow \langle k_2,s'|\bar\nu &= \int \frac{d^3q}{(2\pi)^3}\frac{\sqrt{2E_{k_2}}}{\sqrt{2E_q}}\sum_{r'}\left[\langle 0|(2\pi)^3\delta^{(3)}(k_2-q)\delta^{r's'}\bar u_{r'}(q)e^{i\vec{q}\cdot\vec{x}}\right] \\ &= \langle 0|\bar u_{s'}(k_2)e^{i\vec{k}_2\cdot\vec{x}}\end{aligned} \tag{H.10}$$

Therefore the matrix element for leptons is:

$$\langle k_2,s'|\bar\nu\,\gamma^\mu(1+\gamma^5)\,\nu|k_1,s\rangle = \bar u_{s'}(k_2)e^{i\vec{k}_2\cdot\vec{x}}\gamma^\mu(1+\gamma^5)u_s(k_1)e^{-i\vec{k}_1\cdot\vec{x}}$$

$$= \hat{\ell}_\mu e^{-i\boldsymbol{q}\cdot\boldsymbol{x}} \qquad \text{with} \quad \boldsymbol{q} = k_1 - k_2 \ . \tag{H.11}$$

I Expansion of plane wave in spherical harmonics

We derive the expansion of a vector plane wave

$$e_{k\lambda} e^{i\vec{k}\cdot\vec{r}} \ , \tag{I.1}$$

in terms of vector spherical harmonics. If write the Hamiltonian that describes a free particle in spherical coordinates, obtain

$$H_0 = \frac{p_r^2}{2m} + \frac{L^2}{2mr^2} \ , \tag{I.2}$$

it is possible divided into radial part and angular part.

Carrying out the development to find the radial and angular wave function we find that the energy eigenstates of the free particle can be written like

$$\Psi_{\vec{k}} = N\, i^l\, j_l(kr)\, Y_{lm}(\Omega) \tag{I.3}$$

and since $e^{i\vec{k}\cdot\vec{r}}$ is solution for the free particle, we can write as superposition of $\Psi_{\vec{k}}$ so:

$$e^{i\vec{k}\cdot\vec{r}} = \sum_{l=0}^{\infty} \sum_{m=-l}^{l} C_{lm}(\vec{k})\, j_l(kr)\, Y_{lm}(\hat{r}) \ . \tag{I.4}$$

This equation demonstrates that a superposition resembling a plane wave can be constructed from waves originating at a point source. It is established that plane waves result from the superposition of spherical waves, particularly when observed at large distances.

The subsequent step involves determining the coefficients $C_{lm}(\vec{k})$. The z-axis may be oriented to align with $\vec{k}$ in the problem. For the case where $\vec{k} = k\hat{z}$,

$$\vec{k} \cdot \vec{r} = kr\cos\theta \ , \tag{I.5}$$

where θ is the polar angle of the vector $\vec{r}$ with respect to the z-axis. Hence the double sum in Eq. (3.5) must be independent of the azimuthal angle ϕ. This is possible only if

$$C_{lm}(k\hat{z}) = 0 \quad \text{for all } m \neq 0 \tag{I.6}$$

and it follows that only the $m = 0$ term survives and it follows that

$$e^{ikr\cos\theta} = \sum_{l=0}^{\infty} \ .a_l\, j_l(kr)\, Y_{l0}(\Omega) \tag{I.7}$$

We know that (property of Spherical armonics)

$$Y_l^m(\theta,\phi) = (-1)^m \sqrt{\frac{2l+1}{4\pi}\frac{(l-m)!}{(l+m)!}}\, P_l^m(\cos\theta)\, e^{im\phi} \ . \tag{I.8}$$

Inserting Eq.(I.8) into (I.7) with m=0

$$e^{ikr\cos\theta} = \sum_{l=0}^{\infty} a_l\, j_l(kr)\,\sqrt{\frac{2l+1}{4\pi}}\,P_l(\cos\theta)\ . \tag{I.9}$$

For calculate a_l use the orthogonality relation of the Legendre polynomials:

$$\int_{-1}^{1} P_l(x)\,P_{l'}(x)\,dx = \frac{2}{2l+1}\,\delta_{l,l'}\ , \tag{I.10}$$

$$\int_{-1}^{1} P_{l'}(x)\,e^{ikrx}\,dx = \sum_{l=0}^{\infty} a_l\, j_l(kr)\,\sqrt{\frac{2l+1}{4\pi}}\int_{-1}^{1} P_l(x)\,P_{l'}(x)\,dx\ , \tag{I.11}$$

$$\int_{-1}^{1} P_{l'}(x)\,e^{ikrx}\,dx = \sum_{l=0}^{\infty} a_l\, j_l(kr)\,\sqrt{\frac{2l+1}{4\pi}}\frac{2}{2l+1}\delta_{l,l'}\ , \tag{I.12}$$

$$a_l\, j_l(kr) = \sqrt{\pi(2l+1)}\int_{-1}^{1} P_l(x)\,e^{ikrx}\,dx\ , \tag{I.13}$$

with

$$\int_{-1}^{1} P_l(w)\,e^{ikrw}\,dw = 2\,i^l\,j_l(kr)\ , \tag{I.14}$$

and obtain that

$$a_l = \sqrt{4\pi(2l+1)}\,i^l\ . \tag{I.15}$$

Then the expansion of plane wave as a sum over Legendre polynomial

$$\begin{aligned} e^{ikr\cos\theta} &= \sum_{l=0}^{\infty}\sqrt{4\pi(2l+1)}\,i^l\,j_l(kr)\,\sqrt{\frac{2l+1}{4\pi}}\,P_l(\cos\theta) \\ &= \sum_{l=0}^{\infty} i^l(2l+1)j_l(kr)P_l(\cos\theta)\ , \end{aligned} \tag{I.16}$$

and back to harmonics sphericals

$$\boxed{e^{ikr\cos\theta} = \sum_{l=0}^{\infty}\sqrt{4\pi(2l+1)}\,i^l\,j_l(kr)\,Y_{l0}(\Omega)\ .} \tag{I.17}$$

J Properties of Spherical Harmonics

We have

$$Y_{lm}(\hat{r}) = \langle\hat{r}|lm\rangle\ , \qquad \hat{e}_\lambda = \langle\hat{r}|1\lambda\rangle\ . \tag{J.1}$$

So if $|l1JM\rangle = \sum_{m,\lambda}|lm1\lambda\rangle\langle lm1\lambda|l1JM\rangle$ and define the vector Spherical harmonics [63]:

$$\begin{aligned} \mathbf{Y}_{lm}\,\hat{e}_\lambda = \langle r|l\ 1\ J\ M\rangle &= \sum_{m\lambda}\langle r|l\ m\ 1\ \lambda\rangle\langle lm1\lambda|l1JM\rangle\ , \\ \text{use ec.(J.1)}\quad \mathbf{Y}_{lm}\,\hat{e}_\lambda &= \sum_{m\lambda}\langle lm1\lambda|l1JM\rangle Y_{lm}(r)e_\lambda\ , \end{aligned} \tag{J.2}$$

and the inverse relation, is obtain by way of the aid of the orthogonality propieties of Clebsh-Gordan coefficients [63]:

$$Y_{lm}\,\hat{e}_\lambda = \sum_{m\lambda} \langle lm1\lambda | l1JM\rangle \mathbf{Y}^M_{Jl1}\ . \tag{J.3}$$

Also we have the adjoint of vector Spherical harmonics:

$$Y^{\lambda\dagger}_{JJ1} = -(-1)^\lambda Y^\lambda_{JJ1}\ , \tag{J.4}$$

it can be demonstrated that vector spherical harmonics satisfy the following properties, which are useful for the calculation of multipole expansions. [26]:

$$\frac{1}{[l(l+1)]^{1/2}} L Y_{lm} = \frac{1}{[l(l+1)]^{1/2}} \frac{1}{i}(\mathbf{r}\wedge\nabla) Y_{lm} = Y^M_{ll1}\ , \tag{J.5}$$

$$\begin{aligned}\nabla\phi(r) Y^M_{Jl1} = i\left(\frac{d}{dr} - \frac{J}{r}\right)\phi(r)\left(\frac{J}{2J+1}\right)^{1/2} Y^M_{J,J+1,1} \\ + i\left(\frac{d}{dr} + \frac{J+1}{r}\right)\phi(r)\left(\frac{J+1}{2J+1}\right)^{1/2} Y^M_{J,J-1,1}\ ,\end{aligned} \tag{J.6}$$

$$\nabla\cdot\phi(r) Y^M_{JJ1} = 0\ , \tag{J.7}$$

$$\begin{aligned}\nabla\Phi(r)\, Y_{JM} = -\left(\frac{J+1}{2J+1}\right)^{1/2}\left(\frac{d}{dr} - \frac{J}{r}\right)\Phi(r)\,\mathcal{Y}^M_{J,J+1,1} \\ + \left(\frac{J}{2J+1}\right)^{1/2}\left(\frac{d}{dr} + \frac{J+1}{r}\right)\Phi(r)\,\mathcal{Y}^M_{J,J-1,1}\ ,\end{aligned} \tag{J.8}$$

$$\begin{aligned}\nabla\times\left[j_J(\rho)\,\mathbf{Y}^M_{J,J,1}\right] = -i\left(\frac{J}{2J+1}\right)^{1/2} j_{J+1}(\rho)\,\mathbf{Y}^M_{J,J+1,1} \\ + i\left(\frac{J+1}{2J+1}\right)^{1/2} j_{J-1}(\rho)\,\mathbf{Y}^M_{J,J-1,1}\ ,\end{aligned} \tag{J.9}$$

K The Isotropic Harmonic Oscillator

In this appendix, we derive the radial solution for the three-dimensional quantum harmonic oscillator. This system is fundamental in nuclear structure models, especially within the shell model, as it underpins the understanding of level degeneracies and magic numbers.

A nucleon is assumed to move independently within a spherically symmetric harmonic oscillator potential. The corresponding Schrödinger equation is given by:

$$\left(-\frac{\hbar^2}{2m}\nabla^2 + V(r)\right)\Psi(r) = E\Psi(r)\ , \tag{K.1}$$

Here, $V(r) = \frac{1}{2}m\omega^2 r^2$. Due to the spherical symmetry of the potential, the Schrödinger equation is most appropriately solved in spherical coordinates.

Let us write ∇^2 in spherical coordinates [93]

$$\nabla^2 = \frac{1}{r^2}\frac{\partial}{\partial r}\left(r^2\frac{\partial}{\partial r}\right) + \frac{1}{r^2\sin\theta}\frac{\partial}{\partial\theta}\left(\sin\theta\frac{\partial}{\partial\theta}\right) + \frac{1}{r^2\sin^2\theta}\frac{\partial^2}{\partial\phi^2} \ . \tag{K.2}$$

The angular part is related to angular momentum operator:

$$\vec{L} = \vec{r}\times\vec{p} \ ,$$

$$L^2 = (\vec{r}\times\vec{p})^2 \ ,$$

using property $(\vec{a}\times\vec{b})^2 = a^2b^2 - (\vec{a}\cdot\vec{b})^2 + i\hbar\vec{a}\cdot\vec{b}$, obtain the expression:

$$L^2 = r^2p^2 - (\vec{r}\cdot\vec{p})^2 + i\hbar\vec{r}\cdot\vec{p} \ . \tag{K.3}$$

We solve it term by term:

$$\begin{aligned}\vec{r}\cdot\vec{p} &= -i\hbar\,\vec{r}\cdot\vec{\nabla} \\ &= -i\hbar\left[\hat{r}\frac{\partial}{\partial r} + \hat{\theta}\frac{1}{r}\frac{\partial}{\partial\theta} + \hat{\phi}\frac{1}{r\sin\theta}\frac{\partial}{\partial\phi}\right]\cdot\vec{r} \\ &= -i\hbar\, r\frac{\partial}{\partial r} \ .\end{aligned}$$

$$\begin{aligned}(\vec{r}\cdot\vec{p})^2 - i\hbar\vec{r}\cdot\vec{p} &= (-i\hbar r\partial_r)^2 - i\hbar(-i\hbar r\partial_r) \\ &= -\hbar^2\left[r^2\frac{\partial^2}{\partial r^2} + 2r\frac{\partial}{\partial r} \ .\right]\end{aligned}$$

From Eq. (K.3):

$$p^2 = \frac{L^2 + (\vec{r}\cdot\vec{p})^2 - i\hbar\vec{r}\cdot\vec{p}}{r^2} \ . \tag{K.4}$$

Replacing the previous result into Eq. (K.4),we find:

$$p^2 = \frac{L^2}{r^2} - \frac{\hbar^2}{r^2}\left[\frac{\partial}{\partial r}\left(r^2\frac{\partial}{\partial r}\right)\right] \ . \tag{K.5}$$

In comparison with Eq. (K.2), we find:

$$L^2 = -\hbar^2\left[\frac{1}{\sin\theta}\frac{\partial}{\partial\theta}\left(\sin\theta\frac{\partial}{\partial\theta}\right) + \frac{1}{\sin^2\theta}\frac{\partial^2}{\partial\phi^2}\right] \ . \tag{K.6}$$

Since L^2, as shown in Eq. (K.6), does not depend on r, H commutes with both L^2 and L_z.

$$[H, L^2] = 0$$

Thus H, L^2 have common eigenfunctions and we know that the solution is given by the spherical harmonics, as form:

$$L^2Y_{lm}(\theta,\phi) = l(l+1)\hbar^2Y_{lm}(\theta,\phi) \ . \tag{K.7}$$

Since the Hamiltonian consists of a radial component and an angular component, we can

separate the variables, and the solution becomes:

$$\Psi(r) = \langle \boldsymbol{r}|n,l,m\rangle = \Psi(r,\theta,\phi) = R_{nl}(r)Y_{lm}(\theta,\phi)\ , \tag{K.8}$$

here the quantum number n is introduced to identify the eigenvalues of H. So replace Eqs. (K.6) an (K.8) in the hamiltonian Eq. (K.1):

$$\left[-\frac{\hbar^2}{2m}\frac{\partial}{\partial r}\left(r^2\frac{\partial}{\partial r}\right)+\frac{L^2}{2mr^2}\right]R_{nl}(r)Y_{lm}(\theta,\phi) = (E-V(r))\,R_{nl}(r)Y_{lm}(\theta,\phi)\ . \tag{K.9}$$

Using the eigenvalue Eq. (K.7), we obtain the radial eqaution [68]:

$$-\frac{\hbar^2}{2m}\frac{d^2}{dr^2}R_{nl}(r)+\left[\frac{1}{2}m\omega^2r^2+\frac{l(l+1)\hbar^2}{2mr^2}\right]R_{nl}(r) = ER_{nl}(r) \tag{K.10}$$

The solutions are evaluated at the asymptotic limits as follows:

When $r \to 0$

When $r \to 0$ the E and $\frac{1}{2}m\omega^2r^2$ become very small compared to $\frac{l(l+1)\hbar^2}{2mr^2}$ hence Eq.(K.10) is:

$$-\frac{\hbar^2}{2m}\frac{d^2}{dr^2}R_{nl}(r)+\frac{l(l+1)\hbar^2}{2mr^2}R_{nl}(r) = 0\ .$$

The solutions are of the form:

$$R(r) = r^{l+1}$$

When $r \to \infty$

When $r \to \infty$, E and $\frac{l(l+1)\hbar^2}{2mr^2}$ become too small compared to $\frac{1}{2}m\omega^2r^2$:

$$-\frac{\hbar^2}{2m}\frac{d^2}{dr^2}R(r)+\frac{1}{2}m\omega^2r^2R(r) = 0\ .$$

Which admits solutions:

$$R(r) \sim e^{-\frac{m\omega r^2}{2\hbar}}\ .$$

Finally the solution of eq.(K.10) is

$$R(r) = f(r)\,r^{l+1}e^{-\frac{m\omega r^2}{2\hbar}}\ .$$

Substituting this function:

$$-\frac{\hbar^2}{2m}\frac{d^2}{dr^2}\left[f(r)r^{l+1}e^{-\frac{m\omega r^2}{2\hbar}}\right]+\left[\frac{1}{2}m\omega^2r^2+\frac{l(l+1)\hbar^2}{2mr^2}\right]f(r)r^{l+1}e^{-\frac{m\omega r^2}{2\hbar}} = Ef(r)r^{l+1}e^{-\frac{m\omega r^2}{2\hbar}}\ . \tag{K.11}$$

Calculate of derivate

We define $\alpha = \frac{M\omega}{2\hbar}$ and first compute:

$$\frac{d}{dr}\left[f(r)r^{\ell+1}e^{-\alpha r^2}\right] \ . \tag{K.12}$$

Using the product rule:

$$\begin{aligned}\frac{d}{dr}\left[f(r)r^{\ell+1}e^{-\alpha r^2}\right] &= \left(f'(r)r^{\ell+1} + (\ell+1)r^{\ell}f(r)\right)e^{-\alpha r^2} - 2\alpha r f(r)r^{\ell+1}e^{-\alpha r^2} \\ &= e^{-\alpha r^2}\left[f'(r)r^{\ell+1} + (\ell+1)r^{\ell}f(r) - 2\alpha r^{\ell+2}f(r)\right] \ .\end{aligned} \tag{K.13}$$

Now the second derivative:

$$\begin{aligned}\frac{d^2}{dr^2}\left[f(r)r^{\ell+1}e^{-\alpha r^2}\right] = e^{-\alpha r^2}\Bigg\{ & f''(r)r^{\ell+1} + 2(\ell+1)r^{\ell}f'(r) - 4\alpha r^{\ell+2}f'(r) \\ & + (\ell+1)\ell r^{\ell-1}f(r) - 2\alpha(2\ell+3)r^{\ell+1}f(r) + 4\alpha^2 r^{\ell+3}f(r)\Bigg\} \ .\end{aligned} \tag{K.14}$$

Therefore,

$$\begin{aligned}\frac{d^2R(r)}{dr^2} = e^{-\alpha r^2}r^{\ell+1}\Bigg[& f''(r) + 2\left(\frac{\ell+1}{r} - 2\alpha r\right)f'(r) \\ & + \left(-2\alpha(2\ell+3) + 4\alpha^2 r^2 + \frac{\ell(\ell+1)}{r^2}\right)f(r)\Bigg] \ .\end{aligned} \tag{K.15}$$

Replace in Eq (K.11) and obtain:

$$\frac{d^2}{dr^2}f(r) + 2\left(\frac{l+1}{r} - \frac{m\omega}{\hbar}r\right)f' + \left[\frac{2mE}{\hbar^2} - (2l+3)\frac{m\omega}{\hbar}\right]f = 0 \ . \tag{K.16}$$

Let us try a power series solution

$$f(r) = \sum_{n=0}^{\infty} a_n r^n \ ,$$

so in the Eq. (K.16):

$$\sum_{n=0}^{\infty}\left\{\left[\frac{2ME}{\hbar^2} - \frac{(2\ell+3)M\omega}{\hbar}\right]a_n r^n + \left[-\frac{2M\omega}{\hbar}n + \frac{2ME}{\hbar^2} - \frac{(2\ell+3)M\omega}{\hbar}\right]a_n r^{n-2}\right\} = 0 \ . \tag{K.17}$$

Evaluating some values for a_n we found the recurrence formula:

$$(n+2)(n+2l+3)a_{n+2} = \left[-\frac{2mE}{\hbar^2} + \frac{m\omega}{\hbar}(2n+2l+3)\right]a_n \ . \tag{K.18}$$

Consequently, the function $f(r)$ must contain only even powers of r:

$$f(r) = \sum_{n=0}^{\infty} a_{2n}r^{2n} = \sum_{n'=0,2,4,\ldots}^{\infty} a_{n'}r^{n'} \ . \tag{K.19}$$

Note that when $n \to +\infty$ the function $f(r)$ diverges. So to obtain a finite solution we must require that Eq. (K.19) to stop at a maximum power $r^{n'}$.

For Eq. (K.19), the term $a_{n'+2}$ must be zero. Substituting this result into the recurrence formula Eq. (K.18) yields the quantization condition:

$$\begin{aligned} \frac{2m}{\hbar^2} E_{n'l} - \frac{m\omega}{\hbar}(2n' + 2l + 3) &= 0 \\ E_{n'l} &= (2n' + 2l + 3)\,\frac{\hbar\omega}{2} \\ &= \left(n' + l + \frac{3}{2}\right)\hbar\omega \ , \end{aligned} \tag{K.20}$$

where n' is even and can denoting $n' = 2N$ where $N = 0, 1, 2, 3, \ldots$ and we can write this energy expression:

$$E_{Nl} = \left(2N + l + \frac{3}{2}\right)\hbar\omega \ .$$

Reduction to the Associated Laguerre Equation

We start from the differential equation for $f(r)$:

$$f''(r) + 2\left(\frac{l+1}{r} - \frac{m\omega}{\hbar} r\right) f'(r) + \left[\frac{2mE}{\hbar^2} - (2l+3)\frac{m\omega}{\hbar}\right] f(r) = 0. \tag{K.21}$$

Introduce the oscillator length

$$b = \sqrt{\frac{\hbar}{m\omega}} \ , \tag{K.22}$$

so that

$$\frac{m\omega}{\hbar} = \frac{1}{b^2}. \tag{K.23}$$

Define the dimensionless variable

$$\xi = \frac{r^2}{b^2} \ . \tag{K.24}$$

Then,

$$\frac{d}{dr} = \frac{2r}{b^2}\frac{d}{d\xi} \ ,$$

$$f'(r) = \frac{2r}{b^2} f_\xi \ ,$$

$$f''(r) = \frac{2}{b^2} f_\xi + \frac{4\xi}{b^2} f_{\xi\xi} \ .$$

Substituting into the differential equation and simplifying, we obtain

$$\xi f_{\xi\xi} + \left(l + \frac{3}{2} - \xi\right) f_\xi + \left[\frac{E}{2\hbar\omega} - \frac{2l+3}{4}\right] f = 0 \ . \tag{K.25}$$

Defining

$$n = \frac{E}{2\hbar\omega} - \frac{2l+3}{4} \ . \tag{K.26}$$

The equation takes the standard associated Laguerre form:

$$\xi f_{\xi\xi} + \left(l + \frac{3}{2} - \xi\right) f_\xi + nf = 0 \ . \tag{K.27}$$

This is the differential equation satisfied by the associated Laguerre polynomials. The acceptable solutions correspond to polynomial solutions of degree $n = 0, 1, 2, \ldots$, which requires:

$$n = \frac{E}{2\hbar\omega} - \frac{2l+3}{4} \ . \tag{K.28}$$

This leads to the energy quantization:

$$E_{nl} = \hbar\omega \left(2n + l + \frac{3}{2}\right) \ . \tag{K.29}$$

The solutions of the differential equation are the associated Laguerre polynomials [26]

$$f(\xi) = L_n^{l+1/2}(\xi), \tag{K.30}$$

where the associated Laguerre polynomials are defined by

$$L_n^\alpha(x) = \frac{\Gamma(n+\alpha+1)}{\Gamma(\alpha+1)} x^{-\alpha} e^x \frac{d^n}{dx^n} \left(e^{-x} x^{n+\alpha}\right) \ . \tag{K.31}$$

The radial wave functions are therefore

$$R_{nl}(r) = N_{nl}\, r^l e^{-r^2/(2b^2)} L_n^{l+1/2}\left(\frac{r^2}{b^2}\right) \ , \tag{K.32}$$

where $b = \sqrt{\hbar/(m\omega)}$.

The normalization condition

$$\int_0^\infty |R_{nl}(r)|^2 r^2 dr = 1 \tag{K.33}$$

gives the normalization constant:

$$N_{nl} = \sqrt{\frac{2\,n!}{b[\,\Gamma\left(n + l + \frac{1}{2}\right)]^3}}. \tag{K.34}$$

L Reduction of Current for a Single Nucleon

In this work, we employ Lorentz covariance and current conservation to derive the general form of the electromagnetic current for an on-shell nucleon, following the approaches of Bjorken and Drell and Peskin [105, 106]. This study analyzes the electromagnetic current structure of mesons and nucleons. Motivated by the anomalously large magnetic moment, the modification of minimal electromagnetic coupling is attributed to strong interactions.

The electromagnetic current of the nucleon is influenced by its spin degree of freedom, which permits additional form factors associated with the magnetic structure of a spin–1/2 particle. The proton electromagnetic vertex and its corrections are considered in their most general form:

$$\bar{u}(p')\, e\, \Gamma_\mu(p', p)\, u(p) \ . \tag{L.1}$$

Because the proton current transforms as a four-vector, the only vectors that can be inserted between proton spinors are p_μ, p'_μ, and γ_μ. Therefore, by Lorentz covariance, the most general structure is:

$$\bar{u}(p')\, e\, \Gamma_\mu(p', p)\, u(p) = e\, \bar{u}(p') \left[p_\mu \Gamma_1(q^2) + p'_\mu \Gamma_2(q^2) + \gamma_\mu \Gamma_3(q^2) \right] u(p) \ , \tag{L.2}$$

where $\Gamma_i(q^2)$, $i = 1, 2, 3$, are scalar functions of q^2, with

$$q^2 = (p' - p)^2 \ . \tag{L.3}$$

Identical arguments lead to the same general form for the neutron current.

We now impose current conservation, which gives

$$q^\mu \bar{u}(p') \Gamma_\mu(p', p) u(p) = 0 \ . \tag{L.4}$$

Using $q^\mu = (p' - p)^\mu$, one obtains the constraint

$$\Gamma_1(q^2) = \Gamma_2(q^2) \ . \tag{L.5}$$

As a consequence, the nucleon current takes the more compact form:

$$\bar{u}(p')\, e\, \Gamma_\mu(p', p)\, u(p) = e\, \bar{u}(p') \left[(p_\mu + p'_\mu) \Gamma_1(q^2) + \gamma_\mu \Gamma_3(q^2) \right] u(p) \ . \tag{L.6}$$

To eliminate the vector $(p_\mu + p'_\mu)$, we use the Gordon identity [106]:

$$\bar{u}(p') \gamma_\mu u(p) = \bar{u}(p') \left[\frac{(p + p')_\mu}{2M} + \frac{i \sigma_{\mu\nu} q^\nu}{2M} \right] u(p) \ . \tag{L.7}$$

From this relation, we obtain:

$$\bar{u}(p')(p + p')_\mu u(p) = 2M\, \bar{u}(p') \gamma_\mu u(p) - i\, \bar{u}(p') \sigma_{\mu\nu} q^\nu u(p) \ . \tag{L.8}$$

Replacing this expression in the previous result, we obtain

$$e\, \bar{u}(p') \left[\gamma_\mu (2M \Gamma_1 + \Gamma_3) - i\, \Gamma_1\, \sigma_{\mu\nu} q^\nu \right] u(p) \ . \tag{L.9}$$

Finally, redefining the form factors in terms of the Dirac and Pauli form factors, we obtain

$$\bar{u}(p')\, e\, \Gamma_\mu(p', p)\, u(p) = e\, \bar{u}(p') \left[\gamma_\mu F_1(q^2) + \frac{i \sigma_{\mu\nu} q^\nu}{2M} F_2(q^2) \right] u(p) \ . \tag{L.10}$$

For axial current, the construction is similar of the electromagnetic the onlu difference being the insertion of γ_5 to form the axial vector. Furthermore, in the present work we will assume that there are no induced tensor (second-class axial-vector), so the general axial current is [106]:

$$\langle N | j^5_\mu | N \rangle = \bar{u}(p') \left[\gamma_\mu \gamma_5 F_A(q^2) + q^\nu \gamma_5 F_P(q^2) \right] u(p) \ . \tag{L.11}$$

M Radial integrals

This appendix presents the results of the radial integrals, calculated using the harmonic oscillator wave function. This function describes the radial component found in the reduced

matrix elements of the seven basic operators defined in the Walecka-Donelly method.

To get this elements it is necessary some proprieties of spherical Bessel functions [65]:

$$\left(\frac{d}{d\rho} - \frac{l}{\rho}\right) j_l(\rho) = -\, j_{l+1}(\rho) \tag{M.1.a}$$

$$\left(\frac{d}{d\rho} + \frac{l+1}{\rho}\right) j_l(\rho) = j_{l-1}(\rho), \qquad l > 0 \tag{M.1.b}$$

$$j_{l-1}(\rho) + j_{l+1}(\rho) = \frac{2l+1}{\rho}\, j_l(\rho), \qquad l > 0 \tag{M.1.c}$$

$$\frac{d}{d\rho}\big[\rho^{l+1} j_l(\rho)\big] = \rho^{l+1} j_{l-1}(\rho), \qquad l > 0 \tag{M.1.d}$$

$$j_l(\rho) \xrightarrow[\rho\to 0]{} \frac{\rho^l}{(2l+1)!!} \tag{M.1.e}$$

here $\rho = qx$. With this and the definition of radial wave function of harmonic oscillator finally it is get the subsequent form of the radials integrals [26, 65, 70]:

$$\begin{aligned}\langle n'l'|j_L(\rho)|nl\rangle = {} & \frac{2^L}{(2L+1)!!}\, y^{L/2} e^{-y} \sqrt{(n-1)!(n'-1)!\Gamma\big(n'+l'+\tfrac{1}{2}\big)\,\Gamma\big(n+l+\tfrac{1}{2}\big)} \\ & \times \sum_{k=0}^{n-1}\sum_{k'=0}^{n'-1} \frac{(-1)^{k+k'}}{k!k!'}\, \frac{1}{(n-1-k)!(n'-1-k')!} \\ & \times \frac{\Gamma\big[\frac{1}{2}(l+l'+L+2k+2k'+3)\big]}{\Gamma\big(l+k+\frac{3}{2}\big)\,\Gamma\big(l'+k'+\frac{3}{2}\big)} \\ & \times {}_1F_1\big(\tfrac{1}{2}(L-l-l'-2k-2k'); L+\tfrac{3}{2}; y\big)\ ,\end{aligned} \tag{M.2}$$

$$\begin{aligned}\langle n'l'|j_L(\rho)\left(\frac{d}{dr} - \frac{l}{r}\right)|nl\rangle = {} & \frac{2^{L-1}}{(2L+1)!!}\, y^{(L-1)/2} e^{-y} \\ & \sqrt{(n-1)!(n'-1)!\Gamma\big(n'+l'+\tfrac{1}{2}\big)\,\Gamma\big(n+l+\tfrac{1}{2}\big)} \\ & \times \sum_{k=0}^{n-1}\sum_{k'=0}^{n'-1} \frac{(-1)^{k+k'}}{k!k!'}\, \frac{1}{(n-1-k)!(n'-1-k')!} \\ & \times \frac{\Gamma\big[\frac{1}{2}(L+l+l'+2k+2k'+2)\big]}{\Gamma\big(l+k+\frac{3}{2}\big)\,\Gamma\big(l'+k'+\frac{3}{2}\big)} \\ & \times \Big\{ -\tfrac{1}{2}(l+l'+L+2k+2k'+2) \\ & \quad \times {}_1F_1\big(\tfrac{1}{2}(L-l-l'-2k-2k'-1); L+\tfrac{3}{2}; y\big) \\ & \quad + (2k)\, {}_1F_1\big(\tfrac{1}{2}(L-l-l'-2k-2k'+1); L+\tfrac{3}{2}; y\big) \Big\}\ ,\end{aligned} \tag{M.3}$$

$$\langle n'l'|j_L(\rho)\left(\frac{d}{dr}+\frac{l+1}{r}\right)|nl\rangle = \frac{2^{L-1}}{(2L+1)!!}\,y^{(L-1)/2}e^{-y}$$
$$\sqrt{(n-1)!(n'-1)!\Gamma\left(n'+l'+\tfrac{1}{2}\right)\Gamma\left(n+l+\tfrac{1}{2}\right)}$$
$$\times\sum_{k=0}^{n-1}\sum_{k'=0}^{n'-1}\frac{(-1)^{k+k'}}{k!k!'}\,\frac{1}{(n-1-k)!(n'-1-k')!}$$
$$\times\,\frac{\Gamma\left[\frac{1}{2}(L+l+l'+2k+2k'+2)\right]}{\Gamma\left(l+k+\frac{3}{2}\right)\Gamma\left(l'+k'+\frac{3}{2}\right)}$$
$$\times\left\{-\tfrac{1}{2}(l+l'+L+2k+2k'+2)\right.$$
$$\times\,{}_1F_1\left(\tfrac{1}{2}(L-l-l'-2k-2k'-1);L+\tfrac{3}{2};y\right)$$
$$\left.+\,(2l+2k+1)\,{}_1F_1\left(\tfrac{1}{2}(L-l-l'-2k-2k'+1);L+\tfrac{3}{2};y\right)\right\}, \tag{M.4}$$

where $y=\left(\frac{qb}{2}\right)^2$ and ${}_1F_1$ is a confluent hypergeometric function:

$${}_1F_1(\alpha;\beta;y)=1+\frac{\alpha}{\beta}y+\frac{\alpha(\alpha+1)}{\beta(\beta+1)}\frac{y^2}{2!}+\cdots \tag{M.5}$$

In its present context α is a negative integer, so that the series in Eq. (M.5) is a polynomial of order $-\alpha$ in y.

Bibliography

[1] W. Pauli. "Dear radioactive ladies and gentlemen". In: *Phys. Today* 31N9 (1978), p. 27.

[2] Anthony Mezzacappa and O.E.B. Messer. "Neutrino transport in core collapse supernovae". In: *Journal of Computational and Applied Mathematics* 109.1 (1999), pp. 281–319. ISSN: 0377-0427. DOI: https://doi.org/10.1016/S0377-0427(99)00162-4. URL: https://www.sciencedirect.com/science/article/pii/S0377042799001624.

[3] K. Hirata et al. "Observation of a neutrino burst from the supernova SN1987A". In: *Phys. Rev. Lett.* 58 (14 Apr. 1987), pp. 1490–1493. DOI: 10.1103/PhysRevLett.58.1490. URL: https://link.aps.org/doi/10.1103/PhysRevLett.58.1490.

[4] Shaomin Chen and Xun-Jie Xu. *Solar neutrinos*. 2025. arXiv: 2501.09971 [hep-ph]. URL: https://arxiv.org/abs/2501.09971.

[5] J LESGOURGUES and S PASTOR. "Massive neutrinos and cosmology". In: *Physics Reports* 429.6 (July 2006), pp. 307–379. ISSN: 0370-1573. DOI: 10.1016/j.physrep.2006.04.001. URL: http://dx.doi.org/10.1016/j.physrep.2006.04.001.

[6] Gary Steigman. "Primordial Nucleosynthesis in the Precision Cosmology Era". In: *Annual Review of Nuclear and Particle Science* 57.1 (Nov. 2007), pp. 463–491. ISSN: 1545-4134. DOI: 10.1146/annurev.nucl.56.080805.140437. URL: http://dx.doi.org/10.1146/annurev.nucl.56.080805.140437.

[7] Samoil Bilenky. *Introduction to the physics of massive and mixed neutrinos*. Vol. 817. 2010. DOI: 10.1007/978-3-642-14043-3.

[8] D.K. Papoulias et al. "Constraining nuclear physics parameters with current and future COHERENT data". In: *Physics Letters B* 800 (Jan. 2020), p. 135133. ISSN: 0370-2693. DOI: 10.1016/j.physletb.2019.135133. URL: http://dx.doi.org/10.1016/j.physletb.2019.135133.

[9] T.S. Kosmas et al. "Probing neutrino magnetic moments at the Spallation Neutron Source facility". In: *Physical Review D* 92.1 (July 2015). ISSN: 1550-2368. DOI: 10.1103/physrevd.92.013011. URL: http://dx.doi.org/10.1103/PhysRevD.92.013011.

[10] O. G. Miranda, G. Sanchez Garcia, and O. Sanders. *Coherent elastic neutrino-nucleus scattering as a precision test for the Standard Model and beyond: the COHERENT proposal case*. 2019. arXiv: 1902.09036 [hep-ph]. URL: https://arxiv.org/abs/1902.09036.

[11] D.K. Papoulias and T.S. Kosmas. "COHERENT constraints to conventional and exotic neutrino physics". In: *Physical Review D* 97.3 (Feb. 2018). ISSN: 2470-0029. DOI: 10.1103/physrevd.97.033003. URL: http://dx.doi.org/10.1103/PhysRevD.97.033003.

[12] M. Abdullah et al. *Coherent elastic neutrino-nucleus scattering: Terrestrial and astrophysical applications*. 2022. arXiv: 2203.07361 [hep-ph]. URL: https://arxiv.org/abs/2203.07361.

[13] D. Aristizabal Sierra et al. "Impact of COHERENT measurements, cross section uncertainties and new interactions on the neutrino floor". In: *Journal of Cosmology and Astroparticle Physics* 2022.01 (Jan. 2022), p. 055. ISSN: 1475-7516. DOI: 10.1088/1475-7516/2022/01/055. URL: http://dx.doi.org/10.1088/1475-7516/2022/01/055.

[14] Daniel Z. Freedman. "Coherent effects of a weak neutral current". In: *Phys. Rev. D* 9 (5 Mar. 1974), pp. 1389–1392. DOI: 10.1103/PhysRevD.9.1389. URL: https://link.aps.org/doi/10.1103/PhysRevD.9.1389.

[15] COHERENT Collaboration et al. *The COHERENT Experiment at the Spallation Neutron Source*. 2016. arXiv: 1509.08702 [physics.ins-det]. URL: https://arxiv.org/abs/1509.08702.

[16] D. Akimov et al. "Observation of coherent elastic neutrino-nucleus scattering". In: *Science* 357.6356 (Sept. 2017), pp. 1123–1126. ISSN: 1095-9203. DOI: 10.1126/science.aao0990. URL: http://dx.doi.org/10.1126/science.aao0990.

[17] D. Akimov et al. "First Measurement of Coherent Elastic Neutrino-Nucleus Scattering on Argon". In: *Physical Review Letters* 126.1 (Jan. 2021). ISSN: 1079-7114. DOI: 10.1103/physrevlett.126.012002. URL: http://dx.doi.org/10.1103/PhysRevLett.126.012002.

[18] D. Akimov et al. "Sensitivity of the COHERENT experiment to accelerator-produced dark matter". In: *Physical Review D* 102.5 (Sept. 2020). ISSN: 2470-0029. DOI: 10.1103/physrevd.102.052007. URL: http://dx.doi.org/10.1103/PhysRevD.102.052007.

[19] V. De Romeri et al. "Physics implications of a combined analysis of COHERENT CsI and LAr data". In: *Journal of High Energy Physics* 2023.4 (Apr. 2023). ISSN: 1029-8479. DOI: 10.1007/jhep04(2023)035. URL: http://dx.doi.org/10.1007/JHEP04(2023)035.

[20] S. Adamski et al. *Evidence of Coherent Elastic Neutrino-Nucleus Scattering with COHERENT's Germanium Array*. 2025. arXiv: 2406.13806 [hep-ex]. URL: https://arxiv.org/abs/2406.13806.

[21] D. Akimov et al. *Coherent Scattering Investigations at the Spallation Neutron Source: a Snowmass White Paper*. 2013. arXiv: 1310.0125 [hep-ex]. URL: https://arxiv.org/abs/1310.0125.

[22] E. Aprile et al. "First Indication of Solar Neutrinos via Coherent Elastic Neutrino-Nucleus Scattering with XENONnT". In: *Physical Review Letters* 133.19 (Nov. 2024). ISSN: 1079-7114. DOI: 10.1103/physrevlett.133.191002. URL: http://dx.doi.org/10.1103/PhysRevLett.133.191002.

[23] PandaX Collaboration et al. *First Indication of Solar ^8B Neutrino Flux through Coherent Elastic Neutrino-Nucleus Scattering in PandaX-4T*. 2024. arXiv: 2407.10892 [hep-ex]. URL: https://arxiv.org/abs/2407.10892.

[24] D. S. Akerib et al. *Searches for Light Dark Matter and Evidence of Coherent Elastic Neutrino-Nucleus Scattering of Solar Neutrinos with the LUX-ZEPLIN (LZ) Experiment*. 2025. arXiv: 2512.08065 [hep-ex]. URL: https://arxiv.org/abs/2512.08065.

[25] D. Baxter et al. "Coherent elastic neutrino-nucleus scattering at the European Spallation Source". In: *Journal of High Energy Physics* 2020.2 (Feb. 2020). ISSN: 1029-8479. DOI: 10.1007/jhep02(2020)123. URL: http://dx.doi.org/10.1007/JHEP02(2020)123.

[26] J. D. Walecka. "Semileptonic Weak Interactions in Nuclei". In: *Muon Physics: Weak Interactions*. Ed. by Vernon W. Hughes and C. S. Wu. Section 4. New York: Academic Press, 1975, pp. 113–218. ISBN: 9780123606020.

[27] T.W. Donnelly and J.D. Walecka. "Semi-leptonic weak and electromagnetic interactions with nuclei: isoelastic processes". In: *Nucl. Phys., A* 274.3-4 (Dec. 2024).

[28] Martin Hoferichter, Javier Menéndez, and Achim Schwenk. "Coherent elastic neutrino-nucleus scattering: EFT analysis and nuclear responses". In: *Physical Review D* 102.7 (Oct. 2020). ISSN: 2470-0029. DOI: 10.1103/physrevd.102.074018. URL: http://dx.doi.org/10.1103/PhysRevD.102.074018.

[29] S. Archambault et al. "Dark matter spin-dependent limits for WIMP interactions on ^{19}F by PICASSO". In: *Physics Letters B* 682.2 (Nov. 2009), pp. 185–192. ISSN: 0370-2693. DOI: 10.1016/j.physletb.2009.11.019. URL: http://dx.doi.org/10.1016/j.physletb.2009.11.019.

[30] C. Amole et al. "Dark matter search results from the complete exposure of the PICO-60 bubble chamber". In: *Physical Review D* 100.2 (July 2019). ISSN: 2470-0029. DOI: 10.1103/physrevd.100.022001. URL: http://dx.doi.org/10.1103/PhysRevD.100.022001.

[31] J. D. Walecka. *Theoretical nuclear and subnuclear physics*. Vol. 16. 1995.

[32] S. F. Novaes. *Standard Model: An Introduction*. 2000. arXiv: hep-ph/0001283 [hep-ph]. URL: https://arxiv.org/abs/hep-ph/0001283.

[33] Matthew D. Schwartz. *Quantum Field Theory and the Standard Model*. Cambridge University Press, Mar. 2014. ISBN: 978-1-107-03473-0, 978-1-107-03473-0.

[34] H. Weyl. "Gravitation and electricity". In: *Sitzungsber. Preuss. Akad. Wiss. Berlin (Math. Phys.)* 1918 (1918), p. 465.

[35] C. N. Yang and R. L. Mills. "Conservation of Isotopic Spin and Isotopic Gauge Invariance". In: *Phys. Rev.* 96 (1 Oct. 1954), pp. 191–195. DOI: 10.1103/PhysRev.96.191. URL: https://link.aps.org/doi/10.1103/PhysRev.96.191.

[36] Werner Heisenberg. "Über den Bau der Atomkerne. I". In: *Zeitschrift für Physik* 77 (1932), pp. 1–11. URL: https://api.semanticscholar.org/CorpusID:186218053.

[37] Ryoyu Utiyama. "Invariant Theoretical Interpretation of Interaction". In: *Phys. Rev.* 101 (5 Mar. 1956), pp. 1597–1607. DOI: 10.1103/PhysRev.101.1597. URL: https://link.aps.org/doi/10.1103/PhysRev.101.1597.

[38] Howard Georgi. *Lie algebras in particle physics*. 2nd ed. Vol. 54. Reading, MA: Perseus Books, 1999.

[39] Steven Weinberg. *The Quantum theory of fields. Vol. 1: Foundations*. Cambridge University Press, June 2005. ISBN: 978-0-521-67053-1, 978-0-511-25204-4. DOI: 10.1017/CBO9781139644167.

[40] F. Halzen and Alan D. Martin. *QUARKS AND LEPTONS: AN INTRODUCTORY COURSE IN MODERN PARTICLE PHYSICS*. 1984. ISBN: 978-0-471-88741-6.

[41] Ta-Pei [0000-0002-1137-0969] Cheng and Ling-Fong [0000-0002-8035-3329] Li. *Gauge Theory of Elementary Particle Physics*. Oxford, UK: Oxford University Press, 1984. ISBN: 978-0-19-851961-4, 978-0-19-851961-4.

[42] J. Chadwick. "The intensity distribution in the magnetic spectrum of β particles from radium (B + C)". In: *Verh. Phys. Gesell.* 16 (1914), pp. 383–391.

[43] Charles Drummond Ellis and W. A. Wooster. "The average energy of disintegration of radium E". In: *Proceedings of the Royal Society of London. Series A, Containing Papers of a Mathematical and Physical Character* 117.776 (Dec. 1927), pp. 109–123. ISSN: 0950-1207. DOI: 10.1098/rspa.1927.0168. eprint: https://royalsocietypublishing.org/rspa/article-pdf/117/776/109/25142/rspa.1927.0168.pdf. URL: https://doi.org/10.1098/rspa.1927.0168.

[44] Gerhard Ecker. "James Chadwick: ahead of his time". In: (July 2020). arXiv: 2007.06926 [physics.hist-ph].

[45] E. Fermi. "An attempt of a theory of beta radiation. 1." In: *Z. Phys.* 88 (1934), pp. 161–177. DOI: 10.1007/BF01351864.

[46] S.M. Bilenky. "Neutrino. History of a unique particle". In: *The European Physical Journal H* 38.3 (Dec. 2012), pp. 345–404. ISSN: 2102-6467. DOI: 10.1140/epjh/e2012-20068-9. URL: http://dx.doi.org/10.1140/epjh/e2012-20068-9.

[47] T. D. Lee and Chen-Ning Yang. "Parity Nonconservation and a Two Component Theory of the Neutrino". In: *Phys. Rev.* 105 (1957). Ed. by G. Feinberg, pp. 1671–1675. DOI: 10.1103/PhysRev.105.1671.

[48] T. D. Lee and Chen-Ning Yang. "Question of Parity Conservation in Weak Interactions". In: *Phys. Rev.* 104 (1956), pp. 254–258. DOI: 10.1103/PhysRev.104.254.

[49] C. S. Wu et al. "Experimental Test of Parity Conservation in β Decay". In: *Phys. Rev.* 105 (1957), pp. 1413–1414. DOI: 10.1103/PhysRev.105.1413.

[50] Richard L. Garwin, Leon M. Lederman, and Marcel Weinrich. "Observations of the Failure of Conservation of Parity and Charge Conjugation in Meson Decays: the Magnetic Moment of the Free Muon". In: *Phys. Rev.* 105 (4 Feb. 1957), pp. 1415–1417. DOI: 10.1103/PhysRev.105.1415. URL: https://link.aps.org/doi/10.1103/PhysRev.105.1415.

[51] "92 - ON THE CONSERVATION LAWS FOR WEAK INTERACTIONS". In: *Collected Papers of L.D. Landau*. Ed. by D. TER HAAR. Pergamon, 1965, pp. 742–746. ISBN: 978-0-08-010586-4. DOI: https://doi.org/10.1016/B978-0-08-010586-4.50097-3. URL: https://www.sciencedirect.com/science/article/pii/B9780080105864500973.

[52] Abdus Salam. "On parity conservation and neutrino mass". In: *Il Nuovo Cimento* 5.1 (1957), pp. 299–301. DOI: 10.1007/BF02812841. URL: https://doi.org/10.1007/BF02812841.

[53] M. Goldhaber, L. Grodzins, and A. W. Sunyar. "Helicity of Neutrinos". In: *Phys. Rev.* 109 (3 Feb. 1958), pp. 1015–1017. DOI: 10.1103/PhysRev.109.1015. URL: https://link.aps.org/doi/10.1103/PhysRev.109.1015.

[54] R. P. Feynman and M. Gell-Mann. "Theory of the Fermi Interaction". In: *Phys. Rev.* 109 (1 Jan. 1958), pp. 193–198. DOI: 10.1103/PhysRev.109.193. URL: https://link.aps.org/doi/10.1103/PhysRev.109.193.

[55] E. C. G. Sudarshan and R. E. Marshak. "Chirality Invariance and the Universal Fermi Interaction". In: *Phys. Rev.* 109 (5 Mar. 1958), pp. 1860–1862. DOI: 10.1103/PhysRev.109.1860.2. URL: https://link.aps.org/doi/10.1103/PhysRev.109.1860.2.

[56] Murray Gell-Mann. "The Interpretation of the New Particles as Displaced Charged Multiplets". In: *Il Nuovo Cimento* 4.S2 (1956), pp. 848–866. DOI: 10.1007/BF02748000. URL: https://doi.org/10.1007/BF02748000.

[57] Kazuhiko Nishijima. "Charge Independence Theory of V Particles*". In: *Progress of Theoretical Physics* 13.3 (Mar. 1955), pp. 285–304. ISSN: 0033-068X. DOI: 10.1143/PTP.13.285. eprint: https://academic.oup.com/ptp/article-pdf/13/3/285/5425869/13-3-285.pdf. URL: https://doi.org/10.1143/PTP.13.285.

[58] Carlo Giunti and Chung W. Kim. *Fundamentals of Neutrino Physics and Astrophysics*. Oxford University Press, Mar. 2007. ISBN: 9780198508717. DOI: 10.1093/acprof:oso/9780198508717.001.0001. URL: https://doi.org/10.1093/acprof:oso/9780198508717.001.0001.

[59] G. et al. Arnison. "Experimental observation of isolated large transverse energy electrons with associated missing energy at $\sqrt{(s)}$=540 GeV". In: *Phys. Lett. B* 122 (1983), pp. 103–116.

[60] G. et al. Arnison. "Experimental observation of lepton pairs of invariant mass around 95 GeV/c^2". In: *Phys. Lett. B* 126 (1983), pp. 398–410.

[61] M. Beneke. "Effective field theory - Concepts and applications". English. In: *2009 European School of High-Energy Physics, ESHEP 2009*. 2009 European School of High-Energy Physics, ESHEP 2009. 17th European School of High-Energy Physics, ESHEP 2009 ; Conference date: 14-06-2009 Through 27-06-2009. 2010, pp. 145–195. ISBN: 9789290833536.

[62] John F. Donoghue, Eugene Golowich, and Barry R. Holstein. "Effective field theory for low-energy QCD". In: *Dynamics of the Standard Model*. Cambridge Monographs on Particle Physics, Nuclear Physics and Cosmology. Cambridge University Press, 2023, pp. 200–236.

[63] Alan R Edmonds. "Angular Momentum in Quantum Mechanics". In: 1957. URL: https://api.semanticscholar.org/CorpusID:264715005.

[64] Jouni Suhonen. *From Nucleons to Nucleus: Concepts of Microscopic Nuclear Theory*. Theoretical and Mathematical Physics. Berlin, Germany: Springer, 2007. ISBN: 978-3-540-48861-3, 978-3-540-48859-0. DOI: 10.1007/978-3-540-48861-3.

[65] T. de Forest Jr. and J.D. Walecka. "Electron scattering and nuclear structure". In: *Advances in Physics* 15.57 (1966), pp. 1–109. DOI: 10.1080/00018736600101254. eprint: https://doi.org/10.1080/00018736600101254. URL: https://doi.org/10.1080/00018736600101254.

[66] M.G. Mayer and J.H.D. Jensen. *Elementary Theory of Nuclear Shell Structure*. Structure of matter series. Wiley, 1955. ISBN: 9780598634146. URL: https://books.google.cl/books?id=qLHQAAAAMAAJ.

[67] Chong Qi. *Theoretical Nuclear Physics*. Lecture notes. Apr. 2015. URL: https://www.kth.se/social/files/58d26e56f27654419542e9c8/Lecture2014.pdf.

[68] N. Zettili. *Quantum Mechanics: Concepts and Applications*. Wiley, 2009. ISBN: 9780470746561. URL: https://books.google.cl/books?id=TAjVyzm57YwC.

[69] Ashok Das and Thomas. Ferbel. *Introduction to nuclear and particle physics / A. Das and T. Ferbel.* eng. 2nd ed. River Edge, N.J: World Scientific, 2003. ISBN: 9812387447.

[70] Wick Haxton and Cecilia Lunardini. "SevenOperators, a Mathematica script for harmonic oscillator nuclear matrix elements arising in semileptonic electroweak interactions". In: *Computer Physics Communications* 179.5 (Sept. 2008), pp. 345–358. ISSN: 0010-4655. DOI: 10.1016/j.cpc.2008.02.018. URL: http://dx.doi.org/10.1016/j.cpc.2008.02.018.

[71] T. W. Donnelly and R. D. Peccei. "Neutral Current Effects in Nuclei". In: *Phys. Rept.* 50 (1979), p. 1. DOI: 10.1016/0370-1573(79)90010-3.

[72] T.W. Donnelly and W.C. Haxton. "Multipole operators in semileptonic weak and electromagnetic interactions with nuclei: Harmonic oscillator single-particle matrix elements". In: *Atomic Data and Nuclear Data Tables* 23.2 (1979), pp. 103–176. ISSN: 0092-640X. DOI: https://doi.org/10.1016/0092-640X(79)90003-2. URL: https://www.sciencedirect.com/science/article/pii/0092640X79900032.

[73] V.C. Chasioti and T.S. Kosmas. "A unified formalism for the basic nuclear matrix elements in semi-leptonic processes". In: *Nuclear Physics A* 829.3 (2009), pp. 234–252. ISSN: 0375-9474. DOI: https://doi.org/10.1016/j.nuclphysa.2009.08.009. URL: https://www.sciencedirect.com/science/article/pii/S0375947409005776.

[74] The Editors of Encyclopaedia Britannica. *Spallation.* Encyclopaedia Britannica. July 1998. URL: https://www.britannica.com/science/spallation (visited on 04/04/2026).

[75] Neutron Sciences Directorate, Oak Ridge National Laboratory. *How SNS Works.* https://neutrons.ornl.gov/content/how-sns-works. Recuperado el 19 de febrero de 2026. s.f.

[76] J. Asaadi et al. "Physics Opportunities in the ORNL Spallation Neutron Source Second Target Station Era". In: *Snowmass 2021.* Sept. 2022. arXiv: 2209.02883 [hep-ex].

[77] H. Abele et al. "Particle Physics at the European Spallation Source". In: *Phys. Rept.* 1023 (2023), pp. 1–84. DOI: 10.1016/j.physrep.2023.06.001. arXiv: 2211.10396 [physics.ins-det].

[78] C. L. Cowan et al. "Detection of the Free Neutrino: a Confirmation". In: *Science* 124.3212 (1956), pp. 103–104. DOI: 10.1126/science.124.3212.103. eprint: https://www.science.org/doi/pdf/10.1126/science.124.3212.103. URL: https://www.science.org/doi/abs/10.1126/science.124.3212.103.

[79] John R. Lamarsh and Anthony John Baratta. *Introduction to nuclear engineering John R. Lamarsh, Anthony J. Baratta.* eng. Third edition ; Pearson new international edition. Essex, England: Pearson, 2014. ISBN: 9781292038230.

[80] Alexis Aguilar-Arevalo et al. "Search for light mediators in the low-energy data of the CONNIE reactor neutrino experiment". In: *Journal of High Energy Physics* 2020.4 (Apr. 2020). ISSN: 1029-8479. DOI: 10.1007/jhep04(2020)054. URL: http://dx.doi.org/10.1007/JHEP04(2020)054.

[81] Chao Zhang, Xin Qian, and Muriel Fallot. "Reactor antineutrino flux and anomaly". In: *Progress in Particle and Nuclear Physics* 136 (Mar. 2024), p. 104106. ISSN: 0146-6410. DOI: 10.1016/j.ppnp.2024.104106. URL: http://dx.doi.org/10.1016/j.ppnp.2024.104106.

[82] N. Ackermann et al. "Direct observation of coherent elastic antineutrino–nucleus scattering". In: *Nature* 643.8074 (July 2025), pp. 1229–1233. ISSN: 1476-4687. DOI: 10.1038/s41586-025-09322-2. URL: http://dx.doi.org/10.1038/s41586-025-09322-2.

[83] S. Navas et al. "Review of particle physics". In: *Phys. Rev. D* 110.3 (2024), p. 030001. DOI: 10.1103/PhysRevD.110.030001.

[84] D. K. Papoulias and T. S. Kosmas. "Standard and Nonstandard Neutrino-Nucleus Reactions Cross Sections and Event Rates to Neutrino Detection Experiments". In: *Advances in High Energy Physics* 2015 (2015), pp. 1–17. ISSN: 1687-7365. DOI: 10.1155/2015/763648. URL: http://dx.doi.org/10.1155/2015/763648.

[85] Ayan Chattaraj et al. "Probing conventional and new physics at the ESS with coherent elastic neutrino-nucleus scattering". In: *Journal of High Energy Physics* 2025.5 (May 2025). ISSN: 1029-8479. DOI: 10.1007/jhep05(2025)064. URL: http://dx.doi.org/10.1007/JHEP05(2025)064.

[86] D. Aristizabal Sierra, Jiajun Liao, and D. Marfatia. "Impact of form factor uncertainties on interpretations of coherent elastic neutrino-nucleus scattering data". In: *JHEP* 06 (2019), p. 141. DOI: 10.1007/JHEP06(2019)141. arXiv: 1902.07398 [hep-ph].

[87] Kenneth S Krane. *Introductory nuclear physics*. New York, NY: Wiley, 1988. URL: https://cds.cern.ch/record/359790.

[88] Richard H. Helm. "Inelastic and Elastic Scattering of 187-Mev Electrons from Selected Even-Even Nuclei". In: *Phys. Rev.* 104 (5 Dec. 1956), pp. 1466–1475. DOI: 10.1103/PhysRev.104.1466. URL: https://link.aps.org/doi/10.1103/PhysRev.104.1466.

[89] D. Aristizabal Sierra et al. *Axial-vector neutral-current measurements in coherent elastic neutrino-nucleus scattering experiments*. 2026. arXiv: 2603.05281 [hep-ph]. URL: https://arxiv.org/abs/2603.05281.

[90] J. D. Lewin and P. F. Smith. "Review of mathematics, numerical factors, and corrections for dark matter experiments based on elastic nuclear recoil". In: *Astropart. Phys.* 6 (1996), pp. 87–112. DOI: 10.1016/S0927-6505(96)00047-3.

[91] P. Klos et al. "Large-scale nuclear structure calculations for spin-dependent WIMP scattering with chiral effective field theory currents". In: *Physical Review D* 88.8 (Oct. 2013). ISSN: 1550-2368. DOI: 10.1103/physrevd.88.083516. URL: http://dx.doi.org/10.1103/PhysRevD.88.083516.

[92] Theodore Gray. *The Photographic Periodic Table of the Elements*. https://periodictable.com/index.html. Accessed: 2026-03-17. n.d.

[93] George B Arfken and Hans J Weber. *Mathematical methods for physicists*. San Diego, CA: Academic Press, 1995. URL: https://cds.cern.ch/record/379118.

[94] D. Aristizabal Sierra. *Extraction of neutron density distributions from high-statistics coherent elastic neutrino-nucleus scattering data*. 2023. arXiv: 2301.13249 [hep-ph]. URL: https://arxiv.org/abs/2301.13249.

[95] Kaushik Borah et al. "Parametrization and applications of the low-Q^2 nucleon vector form factors". In: *Physical Review D* 102.7 (Oct. 2020). ISSN: 2470-0029. DOI: 10.1103/physrevd.102.074012. URL: http://dx.doi.org/10.1103/PhysRevD.102.074012.

[96] J. Menéndez, D. Gazit, and A. Schwenk. "Chiral Two-Body Currents in Nuclei: Gamow-Teller Transitions and Neutrinoless Double-Beta Decay". In: *Physical Review Letters* 107.6 (Aug. 2011). ISSN: 1079-7114. DOI: 10.1103/physrevlett.107.062501. URL: http://dx.doi.org/10.1103/PhysRevLett.107.062501.

[97] Noemi Rocco. "Effects of Two-Body Currents on the Nuclear Electroweak Response". Corso di Laurea in Fisica, Anno Accademico 2011–2012. Tesi di Laurea Magistrale. Università degli Studi di Roma "La Sapienza", 2012. URL: https://chimera.roma1.infn.it/OMAR/personal/theses/rocco_ms.pdf.

[98] D. Aristizabal Sierra, N. Mishra, and L. Strigari. *Implications of first neutrino-induced nuclear recoil measurements in direct detection experiments*. 2024. arXiv: 2409.02003 [hep-ph]. URL: https://arxiv.org/abs/2409.02003.

[99] Kate Scholberg. *Observation of Coherent Elastic Neutrino-Nucleus Scattering by COHERENT*. 2018. arXiv: 1801.05546 [hep-ex]. URL: https://arxiv.org/abs/1801.05546.

[100] D. Aristizabal Sierra, Valentina De Romeri, and N. Rojas. "COHERENT analysis of neutrino generalized interactions". In: *Phys. Rev. D* 98 (2018), p. 075018. DOI: 10.1103/PhysRevD.98.075018. arXiv: 1806.07424 [hep-ph].

[101] D. Aristizabal Sierra et al. "Coherent elastic neutrino-nucleus scattering with the directional detector at next generation neutrino facilities". In: *Physical Review D* 104.3 (Aug. 2021). ISSN: 2470-0029. DOI: 10.1103/physrevd.104.033004. URL: http://dx.doi.org/10.1103/PhysRevD.104.033004.

[102] A. S. García-Viltres and E. Vázquez-Jáuregui. "PICO-500: A tonne scale bubble chamber for the search of dark matter". In: *Nuovo Cim. C* 45.1 (2021), p. 7. DOI: 10.1393/ncc/i2022-22007-x.

[103] G. Cowan. *Statistical data analysis*. 1998. ISBN: 978-0-19-850156-5.

[104] A. Airapetian et al. "Precise determination of the spin structure function of the proton, deuteron, and neutron". In: *Physical Review D* 75.1 (Jan. 2007). ISSN: 1550-2368. DOI: 10.1103/physrevd.75.012007. URL: http://dx.doi.org/10.1103/PhysRevD.75.012007.

[105] James D Bjorken and Sidney David Drell. *Relativistic quantum mechanics*. International series in pure and applied physics. New York, NY: McGraw-Hill, 1964. URL: https://cds.cern.ch/record/100769.

[106] Michael E. Peskin and Daniel V. Schroeder. *An Introduction to quantum field theory*. Reading, USA: Addison-Wesley, 1995. ISBN: 978-0-201-50397-5, 978-0-429-50355-9, 978-0-429-49417-8. DOI: 10.1201/9780429503559.